

**MEMS BASED CATHETER FOR ENDOSCOPIC OPTICAL
COHERENCE TOMOGRAPHY**

XU YINGSHUN
(B. Eng, Tianjin University)

A THESIS SUBMITTED
FOR THE DEGREE OF DOCTOR OF PHILOSOPHY
DIVISION OF BIOENGINEERING
NATIONAL UNIVERSITY OF SINGAPORE

2009

To my parents for their love, support and encouragement

ACKNOWLEDGEMENTS

First, I would like to heartfully thank my supervisors, Dr. Chen Nanguang and Dr. Janak Singh, for their erudite knowledge and invaluable suggestions on me through this research project. I also would like to appreciate useful discussions from the collaborators, Prof. Colin J. R. Sheppard from NUS (National University of Singapore), Prof. Malini C. Olivo from NCC (National Cancer Centre) / NUS / SBIC (Singapore Bioimaging Consortium) and Mr. C. S. Premachandran from IME (Institute of Microelectronics, A*STAR).

The work environment provided by the Optical Bioimaging Laboratory at NUS and MMC (Microsystems, Modules and Components) Laboratory and SAM (Sensors & Actuator Microsystems) Programme at IME is quite helpful and makes it an excellent workplace for research and development in high efficiency. I also acknowledge leadership and support for other mentors and colleagues, including Prof. Kwong Dim-Lee, Dr. Feng Hanhua, Dr. Kotlanka Ramakrishna, Chen Wei Sheng Kelvin, Ahmad Khairyanto Bin Ratman and IME staff members for their various guidance and assistance. Finally, the love, support and encouragements from my parents and friends have inspired me continuously to complete this project and march forward in research.

Many thanks to you all,

Xu Yingshun

NUS, Singapore

2009

PUBLICATIONS & PRESENTATIONS

- **Y. Xu**, M. Wang, C. S. Premachandran, K. W. S. Chen, N. Chen and M. Olivo, “Platinum microheater integrated silicon optical bench assembly for endoscopic optical coherence tomography” *Journal of Micromechanics and Microengineering* 20, 015008 (2010).
- **Y. Xu**, J. Singh, T. Selvaratnam and N. Chen, “Two-axis gimbal-less electrothermal micromirror for large angle circumferential scanning” *IEEE Journal of Selected Topics in Quantum Electronics* 15, pp. 1432-1438 (2009).
- C. S. Premachandran, A. Khairyanto, K. W. S. Chen, J. Singh, J. H. S. Teo, **Y. Xu**, N. Chen, C. Sheppard and M. Olivo, “Design, fabrication and assembly of an optical biosensor probe package for OCT (Optical Coherence Tomography) application” *IEEE Transaction on Advanced Packaging* 32, pp. 417-422 (2009).
- Khairyanto, C. S. Premachandran K. W. S. Chen, J. Singh, J. Chandrappan, J. H. Lau and **Y. Xu**, “Optical alignment of dual-axis MEMS based scanning optical probe for optical coherence tomography (OCT) application” *the 10th Electronics Packaging Technology Conference (EPTC'08)*, Singapore, pp. 945-950 (2008).
- **Y. Xu**, J. Singh, C. S. Premachandran, A. Khairyanto, K. W. S. Chen, N. Chen, C. J. R. Sheppard and M. Olivo, “Design and development of a 3D scanning MEMS OCT probe using a novel SiOB package assembly” *Journal of Micromechanics and Microengineering* 18, 125005 (2008).
- M. Olivo, J. Singh, **Y. Xu** and C. S. Premachandran, “MEMS Optical Probe for Cancer Diagnostics Using Optical Coherence Tomography” *A*STAR Scientific Conference & RI Open House*, Singapore (2008).
- **Y. Xu**, J. Singh and N. Chen, “Modeling of two-axis gimbal-less scanning micromirror” *the 22th European Conference on Solid-State Transducers (Eurosensors XXII)*, Dresden, Germany, pp. 56-59 (2008).
- **Y. Xu**, J. Singh, C. S. Premachandran, A. Khairyanto, K. W. S. Chen, N. Chen, C. J. R. Sheppard and M. Olivo, “Two axes MEMS probe for endoscopic optical coherence tomography” *the 6th International Conference on Optics Design and*

Fabrication (ODF'08), Taipei, Taiwan, PS-163 (2008).

- S. Premachandran, A. Khairyanto, K. W. S. Chen, J. Singh, S. X. L. Wang, **Y. Xu**, N. Chen, C. J. R. Sheppard, M. Olivo and J. Lau, “Influence of optical probe packaging on a 3D MEMS scanning micro-mirror for optical coherence tomography (OCT) applications” *the 58th Electric Components and Technology Conference (ECTC'08)*, Lake Buena Vista, USA, pp. 829-833 (2008).
- J. Singh, J. H. S. Teo, **Y. Xu**, C. S. Premachandran, N. Chen, K. Ramakrishna, M. Olivo and C. J. R. Sheppard, “A two axes scanning SOI MEMS micromirror for endoscopic bioimaging” *Journal of Micromechanics and Microengineering* **18**, 025001 (2008).
- J. Singh, **Y. Xu**, C. S. Premachandran, J. H. S. Teo and N. Chen, “Novel 3D micromirror for miniature optical bio-probe SiOB assembly” *the Microfluids, BioMEMS and Medical Microsystems VI, part of the SPIE Photonics West (PW'08)*, San Jose, USA, 688608 (2007).
- **Y. Xu**, J. Singh, J. H. S. Teo, K. Ramakrishna, C. S. Premachandran, K. W. S. Chen, T. K. Chuah, N. Chen, M. Olivo and C. J. R. Sheppard, “MEMS based non-rotatory circumferential scanning optical probe for endoscopic optical coherence tomography” *the Optical Coherence Tomography and Coherence Techniques III, part of the European Conference on Biomedical Optics (ECBO'07)*, Munich, Germany, 662733 (2007).
- **Y. Xu**, J. Singh, C. J. R. Sheppard and N. Chen, “Ultra long high resolution beam by multi-zone rotationally symmetrical complex pupil filter” *Optics Express* **15**, pp. 6405-6413 (2007).
- C. S. Premachandran, K. W. S. Chen, J. Singh, J. H. S. Teo, **Y. Xu**, N. Chen, C. J. R. Sheppard and M. Olivo, “Design, fabrication and assembly of an optical biosensor probe package for OCT (optical coherence tomography) application” *the 57th Electric Components and Technology Conference (ECTC'07)*, Nevada, USA, pp. 1556-1560 (2007).

TABLE OF CONTENTS

| | PAGE |
|--|-----------|
| ACKNOWLEDGEMENTS | I |
| PUBLICATIONS & PRESENTATIONS | II |
| TABLE OF CONTENTS | IV |
| SUMMARY | VIII |
| LIST OF FIGURES | X |
| LIST OF TABLES | XVI |
| LIST OF ABBREVIATIONS | XVII |
| CHAPTER 1 INTRODUCTION | 1 |
| 1.1 INTRODUCTION TO OCT | 1 |
| 1.2 ENDOSCOPIC OCT | 6 |
| 1.3 ORGANIZATION OF THE DISSERTATION | 10 |
| CHAPTER 2 OVERVIEW ON MEMS AND OPTICAL MEMS | 12 |
| 2.1 ACTUATION MECHANISMS OF MEMS SCANNERS | 13 |
| 2.1.1 ELECTROSTATIC SCANNERS | 13 |
| 2.1.2 ELECTROTHERMAL SCANNERS | 15 |
| 2.1.3 MAGNETIC AND ELECTROMAGNETIC SCANNERS | 16 |
| 2.1.4 OTHER ACTUATION METHODS | 17 |

| | |
|--|-----------|
| 2.2 STRUCTURES OF MEMS SCANNERS | 17 |
| CHAPTER 3 MICROMACHINED ELECTROTHERMAL SCANNERS: THEORETICAL STUDY, MATERIAL SELECTION AND MODELING | 18 |
| 3.1 THEORETICAL STUDY AND MATERIAL SELECTION FOR ELECTROTHERMAL ACTUATOR | 18 |
| 3.2 MODELING OF TWO-AXIS GIMBAL-LESS STRUCTURE | 38 |
| CHAPTER 4 MICROMACHINED ELECTROTHERMAL SCANNERS: DESIGNS, FABRICATION PROCESS AND CHARACTERIZATION | 49 |
| 4.1 MICROMACHINED ELECTROTHERMAL SCANNERS DESIGNS | 49 |
| 4.1.1 TWO-AXIS GIMBAL-LESS ELECTROTHERMAL SCANNERS BASED ON CURVED ACTUATORS | 50 |
| 4.1.2 TWO-AXIS GIMBAL-LESS ELECTROTHERMAL SCANNERS BASED ON FOLDED ACTUATORS | 51 |
| 4.2 MICROMACHINED ELECTROTHERMAL SCANNERS FABRICATION PROCESSES | 57 |
| 4.2.1 CMOS-COMPATIBLE PROCESSES | 62 |
| 4.2.2 MEMS PROCESSES | 63 |
| 4.2.3 DEVICE DICING AND RELEASING PROCESSES | 64 |
| 4.2.3.1 MECHANICAL DICING WITHOUT PROTECTIVE COATING | 64 |
| 4.2.3.2 LASER DICING | 65 |

| | |
|---|----|
| 4.2.3.3 MECHANICAL DICING WITH PROTECTIVE COATING | 67 |
| 4.3 MICROMACHINED ELECTROTHERMAL SCANNERS CHARACTERIZATIONS | |
| | 70 |
| 4.3.1 TWO-AXIS GIMBAL-LESS ELECTROTHERMAL SCANNERS BASED ON CURVED ACTUATORS | 71 |
| 4.3.1.1 STEADY STATE PERFORMANCE (DC TRANSFER CHARACTERISTICS) | 71 |
| 4.3.1.2 RADIUS OF CURVATURE | 72 |
| 4.3.1.3 FREQUENCY RESPONSE | 74 |
| 4.3.1.4 REPEATABILITY AND RELIABILITY MEASUREMENTS | 75 |
| 4.3.2 TWO-AXIS GIMBAL-LESS ELECTROTHERMAL SCANNERS BASED ON FOLDED ACTUATORS | 76 |
| 4.3.2.1 STEADY STATE PERFORMANCE (DC TRANSFER CHARACTERISTICS) | 76 |
| 4.3.2.2 RADIUS OF CURVATURE | 78 |
| 4.3.2.3 FREQUENCY RESPONSE | 79 |
| 4.4 SUMMARY OF SCANNERS PERFORMANCE | 81 |
| CHAPTER 5 SiOB ASSEMBLY: DESIGNS, FABRICATION PROCESS, ASSEMBLY AND CHARACTERIZATION | 83 |

| | |
|--|-----|
| 5.1 TRADITIONAL SiOB | 85 |
| 5.1.1 DESIGN | 85 |
| 5.1.2 FABRICATION PROCESS | 87 |
| 5.1.3 ASSEMBLY | 89 |
| 5.1.4 CHARACTERIZATION | 91 |
| 5.1.4.1 RELIABILITY TEST OF MICRO SOLDER BALLS | 91 |
| 5.1.4.2 OPTICAL TEST OF ASSEMBLED SiOB | 93 |
| 5.1.5 DRAWBACKS OF TRADITION SiOB | 97 |
| 5.2 SiOB WITH INTEGRATED PLATINUM MICROHOTPLATES AND COMB INSULATOR | 98 |
| 5.2.1 DESIGN | 98 |
| 5.2.2 FABRICATION PROCESS | 101 |
| 5.2.3 CHARACTERIZATION | 103 |
| 5.3 SUMMARY OF SiOB ASSEMBLY | 106 |
| CHAPTER 6 ENDOSCOPIC OCT DEMONSTRATION | 108 |
| 6.1 EXPERIMENTAL SETUP | 108 |
| 6.2 OCT IMAGES | 110 |
| CHAPTER 7 CONCLUSION AND FUTURE RESEARCH | 114 |
| BIBLIOGRAPHY | 117 |

SUMMARY

The optical coherence tomography (OCT) has grown into a well recognized non-invasive optical imaging modality for imaging biological systems. This technology promises the capability of providing 2D / 3D high resolution *in vivo* and *in situ* images and excellent optical sectioning for imaging multilayer microstructures of internal organs. Recently in order to avoid destructive effects on tissues by using conventional biopsy and reduce sampling errors, the idea of “optical biopsy” by utilizing endoscopic OCT (EOCT) was introduced.

EOCT features its miniaturization of the optical system and scanners in the sample arm of OCT system. Initially most catheters developed for EOCT are based on the assemblies of microprism and single mode fiber (SMF) which are stretched or rotated by external actuation mechanisms. Their scanning speeds are quite limited due to the friction and inertial of devices. The recent rapid growth of microelectromechanical system (MEMS) benefits modern EOCT catheters by offering compact, robust, high speed scanning, light weight micro devices.

This dissertation presents the design, fabrication and characterization of several novel MEMS scanners and corresponding silicon optical bench (SiOB) assemblies for EOCT applications. The theoretical study on performance optimization of electrothermal actuators and modeling of the two-axis gimbal-less structure of MEMS scanners are also discussed in the dissertation. The preliminary OCT imaging results of fully developed EOCT catheter are demonstrated.

The curved actuator based MEMS scanner is based on novel silicon-on-insulator (SOI) process and consists of four bimorph (Al / Si) electrothermal actuators, four flexure

springs and 500 μm diameter high reflective mirror plate. With less than 2 V drive voltage, it provides large deflection angle of up to 17° and -3 dB full range swing bandwidth of 46 Hz. The EOCT catheter integrated with the MEMS scanner has the outer dimension of about 4 mm with transparent, biocompatible polycarbonate housing. The folded bimorph actuator (FBA) based MEMS scanners has an optimized structure for large angle circumferential scanning application.

LIST OF FIGURES

| FIGURES | PAGE |
|--|------|
| 1.1 Schematics diagrams of (a) TDOCT, (b) FDOCT and (c) SSOCT system. | 2 |
| 1.2 Focusing conditions of (a) low NA in OCT and (b) high NA in other optical microscopes. | 3 |
| 1.3 (a) Conventional bench top OCT configuration. (b) Conceptual depiction of miniature OCT optics. | 6 |
| 1.4 (a) Conventional endoscopic OCT catheter by proximal end actuation. (b) MEMS based endoscopic OCT catheter by distal end actuation. | 7 |
| 2.1 Side view of (a) parallel-plate type and (b) vertical comb drive type electrostatic MEMS scanners. | 14 |
| 3.1 Schematic drawing of a bimorph microactuator. | 20 |
| 3.2 Curvatures of different metal-Si combinations with various thickness ratios. | 26 |
| 3.3 Curvatures of different metal- SiO_2 combinations with various thickness ratios. | 27 |
| 3.4 Curvatures of different metal-Ge combinations with various thickness ratios. | 28 |
| 3.5 Curvatures of different metal (including Si)-Ge combinations with various thickness ratios. | 29 |
| 3.6 Thermal response time of different metal-Si combinations with various thickness ratios. | 33 |
| 3.7 Thermal response time of different metal- SiO_2 combinations with various thickness ratios. | 34 |
| 3.8 Thermal response time of different metal-Ge combinations with various thickness ratios. | 35 |
| 3.9 Thermal response time of different metal (including Si)-SU8 combinations with various thickness ratios. | 36 |
| 3.10 Top-view (a) and side-view (b) of the spatial four-spring and plate system. (From figure 2 in [4.28]) | 39 |
| 3.11 Deflection angles versus vertical displacement at free end of (a) spring 1, (b) mirror plate and (c) spring 2. (From figure 3 in [4.28])) | 44 |

| | |
|--|----|
| 3.12 Normalized elastic force versus vertical displacement at free end in examples with the spring free length of (a) 100, (b) 164.5 and (c) 250. (From figure 4 in [4.28])) | 45 |
| 3.13 Lateral shift trajectory of the centroid of the mirror plate. (From figure 5 in [4.28])) | |
| | 46 |
| 4.1 SEM micrographs of (a) 3D micromirror with straight actuators. (b) A close up view of an actuator, a spring and a mirror plate. (Redraw from Figure 1 in [5.1]) | 49 |
| 4.2 Electro-thermally actuated 3D micromirror design: (a) linear actuators and (b) curved actuators. (From Figure 3 in [5.2]) | 50 |
| 4.3 (a) A two-axis gimbal-less micromirror with FBAs. (b) A close up view of the Al wires on the straight microstructure of a FBA. (Figure 4.3 (a) redraw from Figure 1 (c) in [5.3]) | 51 |
| 4.4 Comparison of bimorph bending actuators providing (a). vertical displacement and (b) rotational angle. Solid patterns show a tilting micromirror while hollow patterns show a resting micromirror. (From Figure 2 in [5.3]) | 53 |
| 4.5 Top-view of a 3D model of a two-axis gimbal-less micromirror created by Coventorware. (From Figure 3 in [5.3]) | 55 |
| 4.6 3D displays of simulation results of the two-axis micromirror under multichannel sinusoidal waveforms with different phase changes: (a) 0°; (b) 90°; (c) 180°; (d) 270°. (From Figure 4 in [5.3]) | 55 |
| 4.7 (a) Silicon substrate after implantation steps. (b) Substrate after Al patterning (mask #2) and depositing back side masking layers. (c) PETEOS (5000 Å thick) deposition and patterning (mask#3). (d) Thin Cr–Au (150–500Å) deposition and patterning for reflecting surface. (e) Processed wafer after four probes ECE in aqueous KOH. (f) Silicon cut through oxide hard mask and final release of the structure. (g) Plane view representation of cross-section (b), numbers are the n-layer thicknesses. (From Figure 3 in [5.1]) | 57 |
| 4.8 Silicon etching in an aqueous KOH. (From Figure 8 in [5.2]) | 60 |
| 4.9 SOI thermally actuated micromirror fabrication process flow. (From Figure 9 in [5.2]) | 61 |

| | |
|--|----|
| 4.10 Oxide hard mask, mirror metal and Al heaters. (From Figure 10 in [14]) | 62 |
| 4.11 Missing mirror plate of a released micromirror after mechanical dicing without protective coating. (From Figure 4 in [5.4]) | 64 |
| 4.12 (a) A released micromirror attached on an adhesive tape after laser dicing. (b) The micro plate and (c) pads were contaminated by white debris generated by laser dicing. (d) Rough edge of the micromirror. | 65 |
| 4.13 Damaged micromirror after laser dicing. (From Figure 6 in [5.4]) | 66 |
| 4.14 A diced micromirror protected by photoresist. (From Figure 7 in [5.4]) | 67 |
| 4.15 Optical images of the released micromirror devices: (a) mirror with a linear actuator, (b) mirror with a curved actuator, (c) mirror view from top, (d) light transmission from back. (Redraw from Figure 11 in [5.2]) | 68 |
| 4.16 SEM micrographs of the realized compact size large tilt angle micromirrors: (a) 400 μm mirror with linear actuators, (b) 500 μm mirror with curvilinear actuators and springs. (Redraw from Figure 12 in [5.2]) | 69 |
| 4.17 Experiment setup for micromirror characterization. | 70 |
| 4.18 Test results of micromirror chips fabricated using 1.5 μm SOI substrates. | 71 |
| 4.19 Frequency response of the micromirror with a unipolar 1.2 V peak-to-peak sinusoidal signal for full range swing. (From Figure 4 in [5.5]) | 74 |
| 4.20 (a)–(b) Lissajous patterns scanned by the micromirror. (From Figure 5 in [5.5]) | 75 |
| 4.21 Measured voltage-current relationship of actuators. (From Figure 6 in [5.3]) | 76 |
| 4.22 Measured voltage-mechanical deflection relationship of the two-axis micromirror. (From Figure 7 in [5.3]) | 76 |
| 4.23 3D display of the surface profile of the two-axis micromirror. (From Figure 8 in [5.3]) | 78 |

| | |
|--|----|
| 4.24 (a) Schematic diagram of the micromirror driver circuit for multichannel arbitrary waveform generation; (b) details in single channel. (From Figure 9 in [5.3]) | 79 |
| 4.25 (a) Frequency response of the two-axis micromirror under four channels sine wave drive signals for full range swing; (b) measured and simulated angular fluctuation of mechanical deflection of the micromirror to all direction. (From Figure 10 in [5.3]) | 80 |
| 5.1 An early stage prototype of SiOB. | 84 |
| 5.2 (a) Assembled traditional SiOB with flexure PCB interface. (b) Packaged traditional SiOB assembly ready for OCT imaging test. (Redraw from Figure 16 in [5.15] and Figure 10 in [5.16], respectively) | 85 |
| 5.3 Fabrication process: (a) silicon oxide and silicon nitride deposition for the hard mask; (b) KOH wet etching for the trench; (c) chromium/gold deposition, photoresist electroplating on the slope and chromium/gold wet etching for electrical wires. (d) Side view of traditional SiOB assembly. (Redraw from Figure 6 in [5.14]) | 87 |
| 5.4 (a) Micromirror attached by micro solder balls. (b) Assembly of the micromirror to the lower substrate of the SiOB by two steps micro soldering technology. (b) Interconnection between the micromirror and the chromium/gold electrical wires on the slope of the trench. (Note: different dummy micromirrors were used for assembly testing, so (a) and (b) show different micromirrors used.) (Redraw from Figure 8, 12 and 13 in [5.15]) | 89 |
| 5.5 (a) Placement of the micromirror onto the lower substrate with the micro solder balls. (b) Placement of the GRIN lens assembly onto the upper substrate. (c) Placement of the upper substrate onto the lower substrate. (d) Full assembly and plastic packaging of the MEMS based endoscopic OCT catheter. (Redraw from Figure 1, 7, 8 and 9 in [5.16]) | 90 |
| 5.6 (a) Interconnection between a pad and a micro solder ball. (b) Broken pad after shear test. (Redraw from Figure 10 and 11 in [5.15]) | 91 |

| | |
|--|-----|
| 5.7 (a) Close up view of an assembled SiOB. (b) Experimental setup for optical characterization. (Redraw from Figure 6 (b) and (c) in [5.17]) | 93 |
| 5.8 (a) Optical simulation of the catheter with GRIN lens and micromirror. (b) Effect of the micromirror's curvature on the coupling efficiency. (c) Effect of the micromirror's curvature on the working distance. (d) Effect of tilting of the micromirror during assembly. (Redraw from Figure 4, 5, 6 and 7 in [16]) | 94 |
| 5.9 Optical image of the Platinum microheater on the lower silicon substrate. | 98 |
| 5.10 Fabrication process: (a) silicon oxide and silicon nitride deposition for stress balancing; (b) Titanium / Platinum lift-off for the microhotplates, silicon oxide deposition for electrical isolation, chromium/gold deposition for electrical wires; (c) DRIE for the trench. (d) Side view of new SiOB assembly. | 101 |
| 5.11 Optical images of the SiOB assembly at (a) the distal end, (b) the proximal end and (c) overview with a ruler. | 103 |
| 5.12 (red) step response of the Platinum microheater; (black) Corresponding current change. | 104 |
| 5.13 Optical microscopic images of a Platinum microheater after heating up to failure. | 104 |
| 5.14 (a)-(b): SEM micrographs of a comb isolator and five micro solder balls inside; (c) Cross-sectional SEM micrograph of the connection between the plastic core micro solder ball and pads on the micromirror and the lower silicon substrate. | 106 |
| 6.1 (a) The customized swept source OCT system as the experimental setup for optical probe testing. (b) Photo of the probe holder and multi-axis sample platform for testing. | 108 |
| 6.2 Schematic diagram of the swept source OCT system integrated with the two-axis MEMS scanning probe. | 109 |

6.3 (A, B) OCT cross sectional images obtained by the MEMS scanning probe; (C) the reference image obtained by Thorlabs OCM1300SS commercial system. (From Figure 3 in [6.1])

110

6.4 (A) *En face* image obtained by a wide field optical microscope. (B) OCT *en face* image. (C) 3D reconstruction of a stack of 2D cross-sectional OCT images for. (D) Orthogonal slices of OCT images of an IR viewing card acquired using the SiOB MEMS OCT probe. (Redraw from Fig. 9 in [5.5])

111

LIST OF TABLES

| TABLES | PAGE |
|---|------|
| 3.1 Nomenclature | 19 |
| 3.2 Physical properties of materials commonly used in microfabrication | 24 |
| 3.3 Summary of numerical analyses on deflection of two-layer composite beams under 50K thermal loads (Substrate thickness is fixed at 2 μm) | 30 |
| 3.4 Summary of numerical analyses on thermal response time of two-layer composite beams with optimized thickness ratio for largest deflection. (Substrate thickness is fixed at 2 μm) | 37 |
| 3.5 Geometric and mechanical parameters of the model (From table 1 in [3.28]) | 41 |
| 3.6 Comparison of examples with different spring free length (From table 2 in [3.29]) | 47 |
| 5.1 Shear test results (Redraw from Table. 2 in [5.15]) | 92 |
| 5.2 Parameters of both new and previous SiOB designs as well as different micromirrors used | 100 |

LIST OF ABBREVIATIONS

| | |
|--------|--|
| CMOS | Complementary Metal-Oxide Semiconductor |
| DDS | Digital Direct Synthesizer |
| DOF | Degree OF Freedom |
| DRIE | Deep Reactive-Ion Etching |
| DMD | Digital Mirror Device |
| DWDM | Dense Wavelength-Division-Multiplexed |
| ECE | ElectroChemical Etch-stop |
| EOCT | Endoscopic Optical Coherence Tomography |
| EWOD | ElectroWetting on Dielectric |
| FBA | Folded Bimorph Actuator |
| FDML | Fourier Domain Mode Lock |
| FDOCT | Fourier Domain Optical Coherence Tomography |
| FEA | Finite Element Analysis |
| GI | GastroIntestinal |
| GRIN | Gradient Refractive INdex |
| IFA | Integrated Force Array |
| KOH | Potassium hydroxide |
| LPCVD | Low Pressure Chemical Vapor Deposition |
| MEMS | MicroElectroMechanical Systems |
| NA | Numerical Aperture |
| OCT | Optical Coherence Tomography |
| OXC | Optical Cross Connect |
| PCB | Printed Circuit Board |
| PECVD | Plasma-Enhanced Chemical Vapor Deposition |
| PETEOS | Plasma Enhanced TetraEthylOrthoSilicate |
| SCS | Single Crystalline Silicon |
| SDOCT | Spectral Domain Optical Coherence Tomography |
| SEM | Scanning Electron Microscope |
| SLM | Single Light Modulator |

| | |
|-------|---|
| SiOB | Silicon Optical Bench |
| SMF | Single Model Fiber |
| SNR | Signal-to-Noise Ratio |
| SOI | Silicon-On-Insulator |
| SSOCT | Swept Source Optical Coherence Tomography |
| TDOCT | Time Domain Optical Coherence Tomography |
| TTL | Transistor-to-Transistor Logic |
| UBM | Under Bump Metallization |
| WD | Working Distance |

CHAPTER 1

INTRODUCTION

1.1 INTRODUCTION TO OCT

Over past decades, OCT has evolved from an emerging optical imaging method into a mature clinical imaging modality due to its excellent advantages over conventional optical imaging methods, such as wide field and confocal microscopy. OCT promises excellent optical sectioning capability in μm and offers high penetration depth in highly scattering sample of up to 3 mm. Due to its high sensitivity, OCT has found its place as a widely accepted imaging technique, especially in ophthalmology and other biomedical applications.

The basic setup of an OCT system consists of a low coherence light source as well as a Michelson interferometer. Near infrared light generated from the low coherence light source is split by two equal or unequal parts by the Michelson interferometer which is usually implemented by a 2 X 2 fiber coupler or a beam splitter in a free space configuration and coupled into two arms, reference arm and sample arm. Backscattered light collected from the tissue sample meets the light reflected from a fixed or scanning mirror in the reference arm and generates interference fringes which include depth-resolved information of the tissue sample. Subsequently, the interference fringes are detected by a photodetector in order to convert optical signals into photocurrent for following electronic signal processing.

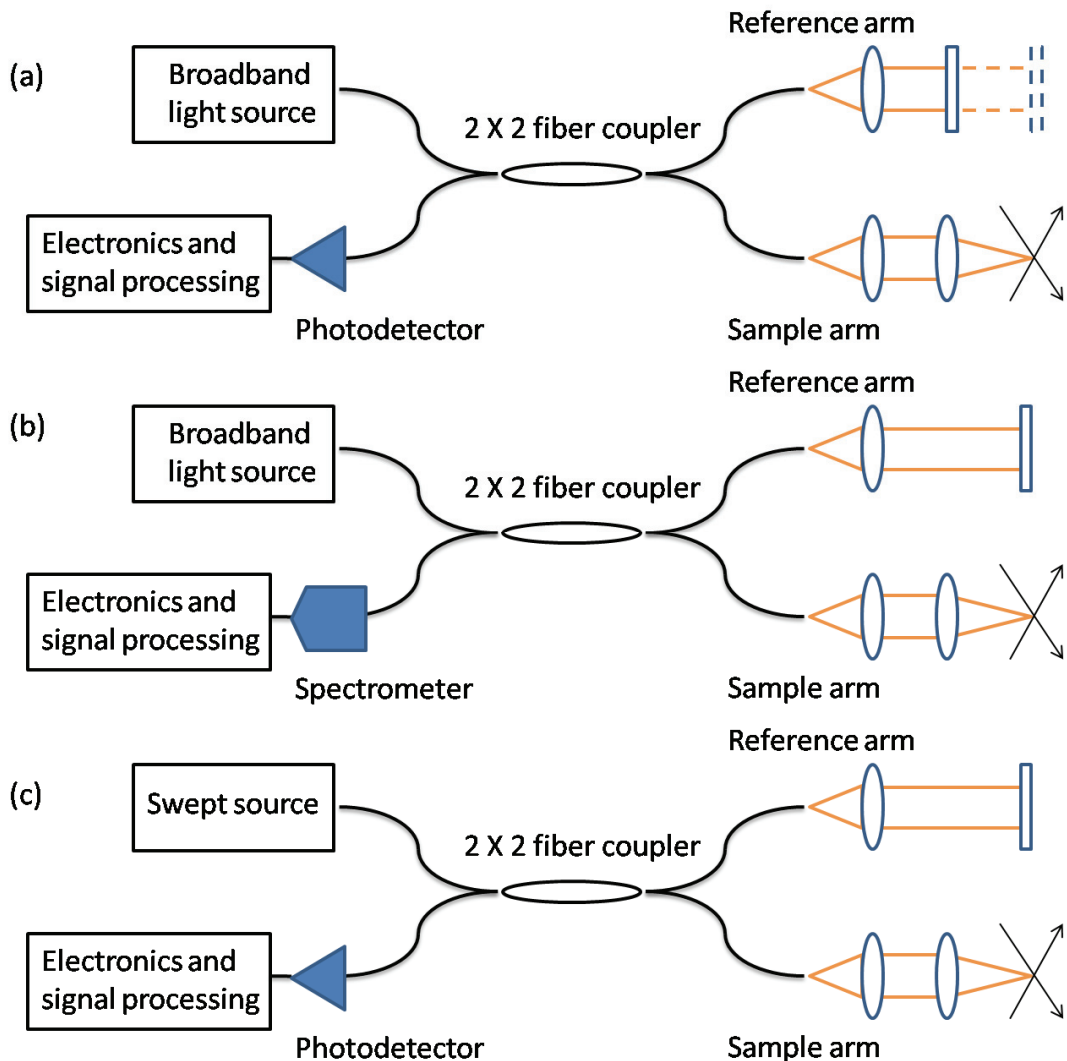


Figure 1.1 Schematics diagrams of (a) TDOCT, (b) FDOCT and (c) SSOCT system.

There are several kinds of OCT which have been developed. At the beginning, in a TDOCT system [1], a scanning optical delay line is incorporated into the reference arm and scans over a certain distance equal to the imaging depth into the sample, as shown in Fig. 1.1 (a). A depth-resolved profile of the sample which is called A-line can be obtained by translating a high reflective mirror in the reference arm at a uniform speed and

filtering the interference fringes signal acquired at the Doppler shifting frequency induced by the scanning mirror in the reference arm. A-lines reflect the refractive index differences in the sample in one dimension and a two dimensional cross-sectional image consists of hundreds to thousands of A-lines. One of the main differences between OCT and other kinds of optical microscopy lies in that its axial resolution only depends on the central wave length λ and bandwidth of the broadband light source $\Delta\lambda$ and is independent of the focusing condition of the objective lens. The axial resolution dz which equals to the coherence length of the laser source l_c is given as [2] in Eq. 1.1:

$$dz = l_c = \ln(2) \frac{2\lambda^2}{\pi\Delta\lambda} \quad (1.1)$$

And its transverse resolution dx can be expressed as in Eq. 1.2:

$$dx = \sqrt{\frac{2b\lambda}{\pi}} \quad (1.2)$$

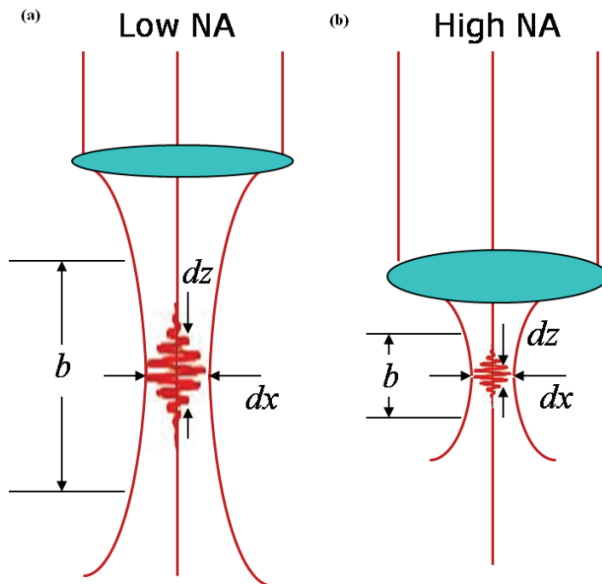


Figure 1.2 Focusing conditions of (a) low NA in OCT and (b) high NA in other optical microscopes.

By using superluminescent diodes, a typical TDOCT system offers 10 to 15 μm axial resolution. The use of ultra broadband light sources can offer even higher axial resolution. A Kerr-lens mode-locked Ti: Al_2O_3 oscillator was demonstrated as a high-power source for high-resolution optical coherence tomographic imaging and yielded *in situ* images of biological tissues with 3.7 μm resolution and 93-dB dynamic range [3] and later a modified system with double-chirped mirrors that emits sub-two-cycle pulses with bandwidths of up to 350 nm, centered at 800 nm achieved axial resolutions of $\sim 1 \mu\text{m}$ with a 110 dB dynamic range in biological tissue [4]. Subsequently, ultra broadband light sources for ultra high resolution OCT were implemented by using photonic crystal fibers for super continuum generation. 2 μm axial resolution with 370 nm bandwidth at a 1.3 μm center wavelength [5], $\sim 0.5 \mu\text{m}$ axial resolution with 400 nm bandwidth at a 725 nm center wavelength [6] and 1.3 μm axial resolution with 600 nm bandwidth at a 1.3 μm center wavelength [7] in biological samples have been reported by using the super continuum generation ultra broadband light source based OCT system. TDOCT systems have employed a variable group delay reference arm to coherently gate backscattered light from various depths in a sample. This approach is hampered by the relatively complicated optical and mechanical designs needed to scan ~ 10 ps delays at kilohertz rates in order to achieve real-time imaging.

An alternate approach to coherence gating without employing a scanning delay line involves acquiring the spectral information of the interferometric signal generated by mixing sample light with reference light at a fixed group delay. Two distinct methods have been developed that employ this spectral domain approach. The first, FDOCT [8-10] uses a broadband light source and achieves spectral discrimination with a dispersive

spectrometer in the detector arm. The second method, SSOCT [11-13], time-encodes wave number by rapidly tuning a narrowband source through a broad optical bandwidth.

The SNR expression of a TDOCT system and a SSOCT system can be expressed as:

$$SNR_{TDOCT} = \frac{\rho R_s S_{TDOCT}}{2eB_{TDOCT}}, \quad (1.3) [2]$$

$$SNR_{SSOCT} = \frac{\rho R_s S_{SSOCT}}{4eB_{SSOCT}} \approx M \frac{\rho R_s S_{TDOCT}}{4eB_{SSOCT}}, \quad (1.4) [14]$$

where ρ is the detector sensitivity, R_s is the sample arm reflectivity, S_{TDOCT} and S_{SSOCT} are the summations of the source spectral density in TDOCT and SSOCT system, respectively, B_{TDOCT} and B_{SSOCT} are the bandwidths of the source in TDOCT and SSOCT system, respectively and $B_{TDOCT} = B_{SSOCT}$. A comparison of Eq. 1.3 and 1.4 indicates that for a rectangular spectral source, a SSOCT system is intrinsically more sensitive than a TDOCT system by a factor of $\frac{1}{2}M$. For a Gaussian source, the SNR advantage of SSOCT over TDOCT is expected to be $\frac{1}{4}M$. Similar conclusion has also been arrived in [15, 16]. This illustrates that for a given source power, sample reflectivity, and A-scan rate, a spectrometer based SSOCT system with $N=2048$ pixels can, in principle, possess a ~ 20 to 30 dB sensitivity advantage over its counterpart TDOCT system. So SSOCT offers a similar sensitivity advantage over the conventional TDOCT. A typical SSOCT system can achieve a SNR of about 120 dB. This improved sensitivity can be traded off in favor of shortened signal acquisition time. Recently, ultrahigh-speed wavelength-swept sources based on FDML method that enable the data acquisition rate of SSOCT of 290 KHz [17], 370 KHz [18, 19] and 236 KHz [20] A-line rates have been successfully developed. This illustrates the potential of SSOCT-based systems to provide real-time imaging of tissue structures [21].

1.2 ENDOSCOPIC OCT

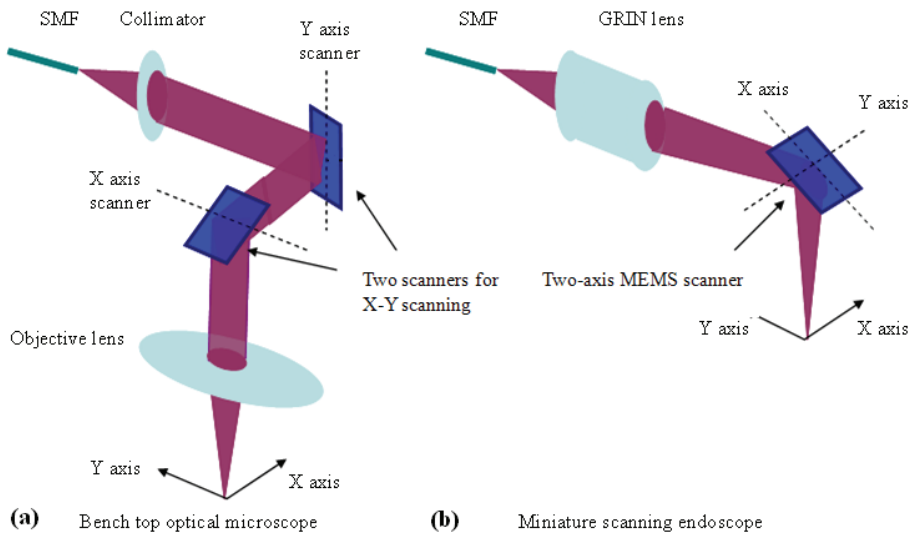
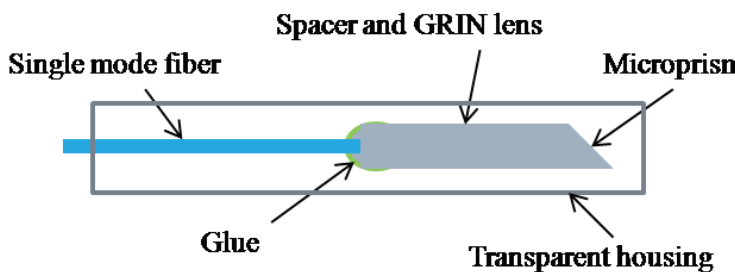


Figure 1.3 (a) Conventional bench top OCT configuration. (b) Conceptual depiction of miniature OCT optics.

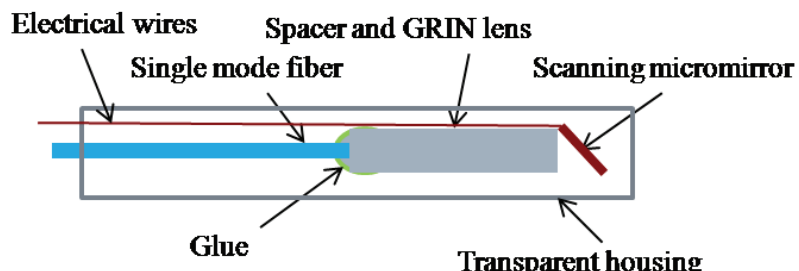
OCT can generate high resolution, cross-sectional images of biological tissues *in situ* and in real time and function as a type of optical biopsy to enable imaging of tissue microstructure with the resolution approaching that of standard excision biopsy, without the need of excising the tissue specimen. One promising application of optical biopsy using OCT is the endoscopic imaging of the GI tract. In contrast to conventional endoscopy, which can only visualize the surface alterations, OCT can detect changes in tissue morphology beneath the tissue surface.

Miniaturization of the optics and scanners in the sample arm of the OCT system is a challenge for endoscopic applications as there is a trade-off between the size of the probe and the quality of the OCT images. Fig. 1.3 illustrates the differences between the conventional bench top OCT optics and the miniature probe OCT optics. The bench top optical microscope configuration utilizes two galvo mirrors for the *x* and *y*-axis scanning

(Fig. 1.3 (a)). As there is no limitation of space, the quality of the image can be improved by having larger scanning mirrors and larger diameter high intensity light beams. In the case of miniature optics (Fig. 1.3 (b)), the diameter of the probe restricts the overall dimensions of the micromirror / microprism and hence in a way constrains the overall efficiency of managing the light beam incident on the sample and scattered light from the sample.



(a) Proximal actuation



(b) Distal actuation

Figure 1.4 (a) Conventional endoscopic OCT catheter by proximal end actuation.
(b) MEMS based endoscopic OCT catheter by distal end actuation.

Therefore, endoscopic imaging with high resolution OCT could potentially improve the detection, visualization, and diagnosis of gastrointestinal diseases. Endoscopic application of OCT and the idea of “optical biopsy” were firstly introduced nearly ten

year ago [22, 23] and the most important task for scientists and engineers to implement OCT-based endoscopes is how to miniaturize OCT probes and steer the near infrared light beam for delivering, focusing, scanning and collecting reflected signals from tissue sample in high efficiency. Furthermore, the optical probe must be flexible and have a small diameter to enable its entry into internal channels. Historically, early stage endeavors on miniature OCT probe implementations were mainly focusing on developments of manipulating single mode fibers for scanning usage. Single mode fibers for near infrared light transmission used in OCT systems is ideally suitable for this kind of purpose. To achieve side-view scanning, the general design of such a kind of probe consists of a mirror or a micro prism mounted at the distal end of single mode fiber to deflect the focused beam from the optical fiber tip out of a window on the side of the probe. External rotational mechanism, such as a motor, for circumferential scanning [24, 25] or a linear translation stage for transverse scanning [26] were connected to drive the single mode fiber but scanning speed was limited to a few Hz.

Recently, many MEMS scanners based on various actuating mechanisms, such as electrothermal [27-30], electrostatic [31-34] and magnetic [35] actuation, were developed for distal end scanning probes of EOCT application. The first implementations of MEMS based EOCT catheters utilized a single-axis electrothermal MEMS scanner [27] and an electrostatic MEMS scanner [31] to perform 2D front-view scanning for bladder cancer detection. The CMOS MEMS process based single-axis electrothermal MEMS scanner involved was capable of steering an optical beam in +/- 15° as well as about 15 mA current consumption correspond to 33 V drive voltage. With 165 Hz resonant frequency, the MEMS scanner provided 2D cross sectional images covering the images range of 2.9

mm by 2.8 mm [27] and even larger, 4.2 mm by 2.8 mm [29]. Their imaging frame rates were about 5 frames/second. Besides, IFA based electrostatic MEMS scanner was also incorporated in EOCT imaging [31]. These devices were 1 or 3 mm wide and 1 cm long. They could produce strains of as much as 20 % and forces up to 13 dyne with applied voltages of +/- 65 V as well as the power consumption less than only 2 mW. The imaging rate was about 4-6 Hz.

However, these single-axis MEMS scanner based EOCT catheter designs have only shown basic functions for 2D imaging with a comparable frame rate to the conventional single mode fiber based EOCT catheters but these catheters were not able to perform 3D imaging without any axial or lateral movements of the endoscope itself. Such 3D scanning MEMS based EOCT catheters [32-35] were then developed in order to provide 3D images as a standard visualization for optical biopsy. These 3D catheters had the capability of 3D imaging as well as high speed real time 2D scanning up to tens Hz. The increased imaging rate effectively avoided motion artifacts caused by human physiological motions and matched the requirements of the real time imaging with the help of evolved FDOCT / SSOCT systems with higher A-line acquisition rates. Most of 3D scanning MEMS based EOCT catheters used two-axis MEMS scanners based on different actuation mechanisms, such as vertical comb drive electrostatic actuation [32], angular comb drive electrostatic actuation [33], electrothermal actuation [34] and magnetic actuation [35]. The two-axis MEMS scanner was integrated at the distal end of the catheter by 45° to the optical axis. Due to its general optical deflection of around +/- 20° on both axes, 3D images of 1 mm by 1 mm by 1.4 mm [32] / 1.8 mm by 1 mm by 1.3 mm [33] / 0.55 mm by 0.55 mm by 1 mm [34, 35] were acquired with up to about 1/30

Hz imaging rate. The low imaging rate is mainly attributed to the A-line acquisition rate limitation of current FDOCT / SDOCT systems. Recently the development of FDML laser source based OCT significantly increased the imaging rate by about 20 times and enabled real time 3D imaging.

1.3 ORGANIZATION OF THE DISSERTATION

The study is divided into two phases. The first phase of this study is related to the design, fabrication and characterization of novel two-axis MEMS scanners. The second phase is to develop corresponding SiOB assemblies for these MEMS scanners and micro optical components for EOCT catheter integration. Chapter 2 provides the overview of MEMS and optical MEMS, especially focusing on actuation mechanisms and various structures of MEMS scanners. Chapter 3 gives theoretical study of multilayer composite beam which is used to optimize the design of bimorph actuators and helpful in material selection as well as a quantitative modeling of two-axis gimbal-less structure, which is the key technology in the MEMS scanner development. In chapter 4, details of the design strategies, fabrication process and characterization of MEMS scanners are provided. Two MEMS scanner designs are investigated. Curved actuator based MEMS scanner is actually an improvement of our earlier successful MEMS scanner [36] which was developed for optical switch applications and FBA based MEMS scanner is an attempt to offer large angular deflection for circumferential scanning application. Chapter 5 describes two SiOB designs, the traditional one and the new one integrated with Pt microhotplates and comb-insulator. The traditional SiOB has been successfully utilized to assemble MEMS scanner, GRIN lens and SMF together and inserted into a transparent

housing in order to build an endoscopic OCT catheter. Preliminary OCT imaging test results are demonstrated in chapter 6. The final chapter concludes the work in the dissertation and proposes possible work in the future.

CHAPTER 2

OVERVIEW ON MEMS AND OPTICAL MEMS

MEMS is defined as the integration of mechanical elements including sensors and actuators and electronics, maybe as well as optical components, in very small scale. Their size normally ranges from the sub micrometer or sub micron level to the millimeter level. MEMS extend the fabrication techniques developed for the integrated circuit industry to add mechanical elements such as beams, gears, diaphragms, and springs to devices. Movable mechanical elements integrated are the indispensable and critical parts of MEMS devices. Most MEMS devices are based on silicon microfabrication techniques [37].

In 1993, optical MEMS as the powerful combination of MEMS and micro-optics has been introduced. The original optical MEMS applications reported were laser scanners and dynamic micromirrors for adaptive optics applications. However, at that time, and possibly a decade before, in the early 1980s, micromirror devices were already under development at TI where they eventually became the foundation of DMD. During the 1990s, the first commercial realization of the DMD became feasible. The trend for optical MEMS during the next decade will be in revolutionizing photonics systems with breakthroughs in telecommunication, micro display and consumer electronics fields. These requirements are only achievable by optical MEMS, the combination of two micro technologies of MEMS and micro-optics. Optical MEMS applications also include sensors, projection and mobile systems and devices.

Whether including movable mechanical elements or not becomes a criterion on distinguishing MEMS devices from other micromachined devices, such as solid state devices [38], active and passive Si photonic circuits [39] and even microfluidic devices [40] which become a hot topic recently. Therefore actuation mechanisms referring to how electrical drive signal generated by external source is transferred into the mechanical deformation or motion of mechanical elements in the MEMS device are challenging research topics in this study and will be reviewed in the following section. In addition, the performance of MEMS devices also highly depend on their well designed structures. So a brief overview on structures of MEMS scanners will also be given in order to provide sufficient back ground information on my study.

2.1 ACTUATION MECHANISMS OF MEMS SCANNERS

The ability to steer or direct light is a key requirement for MEMS scanners and a variety of actuation mechanisms have been applied on this explosive growing area.

2.1.1 ELECTROSTATIC SCANNERS

Most electrostatic micromirrors are based on torsional rotation. Usually there are two groups of electrodes: fixed and movable electrodes. Voltage applied between the fixed and movable electrodes generates electrostatic forces which drive the mirror rotate on the torsion axis until the restoring torque and the electrostatic torque are equal. The electrostatic forces mainly depend on the overlapping area between the fixed and movable electrodes as well as the applied voltage. As the currently dominating actuation mechanism for MEMS scanner, electrostatic actuation can be classified into two groups: parallel plate (Fig. 2.1 (a)) and vertical comb drive (Fig. 2.1(b)).

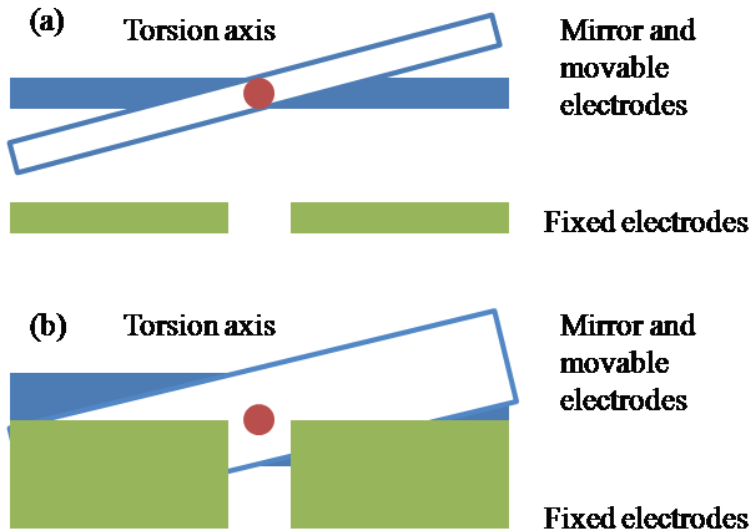


Figure 2.1 Side view of (a) parallel-plate type and (b) vertical comb drive electrostatic MEMS scanners.

In the parallel-type MEMS scanners, the gap between the fixed and movable electrodes is a function of the rotation angle. The initial gap spacing should be large enough to accommodate the scan angle, but small enough for reasonable actuation voltage. So it is a tradeoff in the MEMS scanner design. Parallel-type MEMS scanners can be implemented by surface and bulk micromachining technology but assembly is required to elevate the mirror above the substrate and make a precision alignment on both fixed and movable electrodes. As an example, a polysilicon parallel-type scanner [41] with 400 μm X 400 μm mirror has a static optical scan range of 28° and a drive voltage of 70 V. Its resonant frequency was at 1.5 kHz. Two-axis scanning was achieved by electrostatic force between the mirror and the quadrant electrodes on the substrate. In telecommunication applications, DWDM requires large port count OXC which is the idea application area for two-axis parallel-type electrostatic scanners. Square mirror arrays with up to 256

MEMS scanners have been demonstrated with a surface micromachined process for OXC applications [42-44].

The electrostatic vertical comb drive works more efficient than the parallel-type one. The comb drive consists of a large number of interdigitated electrodes with quite small gap of several micrometers. In the comb drive, the gap is constant and the area of the electrode overlap is a function of the rotation angle. Since the equivalent area of overlapping electrodes of comb drive is far larger than that of the parallel-type, required drive voltage is obviously decreased. Decoupling of the mirror and actuator removes the restriction on the maximum deflection (scan angle) imposed by geometry of the parallel plate. In addition, the pull-in associated with the parallel plate can be avoided in the vertical comb drive. The first MEMS electrostatic comb drives [45] were lateral comb drives formed in polysilicon. For lateral combdrives, the moving comb travels in-plane relative to the fixed comb, parallel to the substrate. Lateral comb drives have been used for scanning micromirrors [46], but vertical comb drives are much more prevalent. In the vertical comb drive, moving comb motion is out of the fixed comb plane and perpendicular to the substrate. The first vertical comb drive [47, 48] was introduced. AVC, as a improved type of vertical comb drive, were implemented by a variety of methods and the device's performances were demonstrated as 3.2° (mechanical range) at 108 V for a scanner with a resonant frequency of 1.4 kHz [49] and 50.9° optical scan range at the resonant frequency of 4.13 kHz at 30 Vdc plus 14 Vpp [50].

2.1.2 Electrothermal scanners

The most widely used electrothermal actuation on MEMS scanners is based so called bimetallic effect. Two or more layers of materials with different properties, such as

Young's modulus, CTE, thermal conductivity and so on, are combined together and bend under certain temperature changes due to the mismatch of CTE. The study on bimetallic electrothermal actuation based MEMS scanners focuses on how to achieve large deflection angle [28] or vertical displacement [51] depending on their specific applications so that new material combination and novel structure for bimorph actuators are highly desired. More detailed discussion on electrothermal actuated MEMS scanners is given as following chapters. Apart from bimorph actuator, thermoelastic driven monomorph actuators based MEMS scanner [52] also demonstrated excellent performance in resonant mode. A SCS micromirror with 1 mm diameter that achieves a scanning deflection angle of $\pm 8.5^\circ$ at 9.5 kHz, which is driven by a 1.5 Volt source.

2.1.3 MAGNETIC AND ELECTROMAGNETIC SCANNERS

Magnetic actuation was firstly introduced to MEMS scanners by bulk micromachining [53] and by surface micromachining [54]. The overall size of the MEMS scanners must be large enough, usually up to several mm, to accommodate external magnets since the magnetic forces scales with the volume of external magnets (permanent or micro coils). Both types of mirrors were approximately 4 mm x 4 mm and achieved deflection angles of greater than 60° with response times ~ 30 msec. The current art of state electromagnetic scanners [55] can provide 3.5 mm x 3.5 mm mirror plate and 5.7 mm x 5.7 mm outer frame with measured resonant frequencies of 380 Hz and 150 Hz, respectively. Reported maximum scan angles (total optical scan range) were 5.44° at 30 mA in resonance for the inner axis and 51.34° at 130 mA in resonance for the outer axis.

2.1.4 OTHER ACTUATION METHODS

Besides electrostatic, electrothermal, magnetic and electromagnetic actuation mentioned above, various alternative actuation methods have been applied on MEMS scanner development, such as piezoelectric [56, 57], pneumatic / thermopneumatic [58, 59] and EWOD [60] actuation. But so far they still suffer from several intrinsic disadvantages, such as fabrication complexity, switching speed, stability and robustness, which make them not practical.

2.2 STRUCTURES OF MEMS SCANNERS

Another critical consideration on MEMS scanner design is the structure of the device, which is dependent on specific applications. Based on the number of rotation axis of the MEMS scanners, currently popular structures can be classified as: single-axis and two-axis. Single-axis design features its simple structure but limit its scanning capability into one dimension. Therefore it has been widely used into optical switch application where only two status: on and off are required. Two-axis design has become the most popular structure since it is easy to realize two dimensional scanning and even tip-tilt-piston full functional motion. My study focused on the development of two-axis electrothermal MEMS scanners. The differences between two-axis gimbal and gimbal-less design are given in chapter 3.

CHAPTER 3

MICROMACHINED ELECTROTHERMAL SCANNERS: THEORETICAL STUDY, MATERIAL SELECTION AND MODELING

As the first section of the chapter introducing my study on surface and bulk micromachined electrothermal scanners, it is focusing on the theoretical study on behaviors of multilayer composite beams under certain thermal loads, material selection for electrothermal actuators as well as quantitative modeling of two-axis gimbal-less structure on which our MEMS scanners are mainly based.

3.1 THEORETICAL STUDY AND MATERIAL SELECTION FOR ELECTROTHERMAL ACTUATOR

Usually a typical electrothermal actuator consists of two layers with different mechanical properties, such as CTE, thermal conductivity, Young's modulus as well as density of materials. The first theoretical formula for evaluation of stresses, arising in two-layer composite, was suggested by G. G. Stoney [61] in 1909 and is widely utilized from the stress calculation based on the measured curvature on the substrate. Later, in 1925 Timoshenko [62] examined the mechanical behavior of bimetal thermostat based on an elementary beam theory. A schematic drawing of the cantilever-type microactuator is shown in Fig. 3.1. The lengths of the two layers combined in the sandwich structure are assumed to be equal. All other dimensions and physical values may be different and are indicated by the indexes 1 and 2, respectively.

Table 3.1 Nomenclature

| | |
|----------------|--|
| $1/\rho$ | Curvature of the biomaterial structure |
| m | Thickness ratio of the biomaterial structure |
| n | Young's modulus ratio of the biomaterial structure |
| h | Total thickness of the biomaterial structure |
| $\Delta\alpha$ | Difference of coefficient of thermal extension (CTE) of two materials |
| ΔT | Isothermal temperature change throughout the biomaterial structure |
| t_i | Thickness of i_{th} layer |
| w_i | Width of i_{th} layer |
| α_i | Coefficient of thermal expansion (CTE) of i_{th} layer |
| E_i | Young's (elastic) modulus of i_{th} layer |
| d_i | Density of i_{th} layer |
| C_i | Heat capacity of i_{th} layer |
| λ_i | Thermal conductivity of i_{th} layer |
| I_i | Moment of inertia of i_{th} layer |
| δ_i | The distance between the centroid of i_{th} layer and N_{th} layer |
| ϵ_i | Strains of i_{th} layer |
| τ | Thermal response time of the biomaterial structure |
| l | Length of the biomaterial structure |

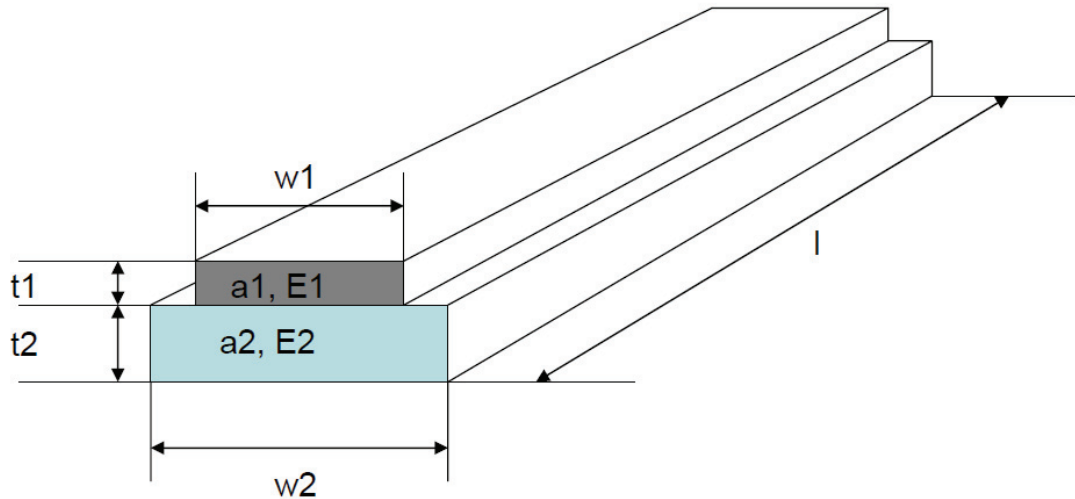


Figure 3.1 Schematic drawing of a bimorph microactuator.

The original Timoshenko's formula is given as:

$$\frac{1}{\rho} = \frac{6\Delta\alpha\Delta T(1+m)^2}{h\left(3(1+m)^2+(1+mn)\left(m^2+\frac{1}{mn}\right)\right)} \quad (3.1)$$

The concept of the continuous displacements between interfaces in the Timoshenko's theory has been a basic hypothesis for numerous other theories. E. Suhir [63, 64] developed an analytical approach based on Timoshenko's formula to predict the shearing (peeling) stresses at the interface of two different materials. It is the first model to calculate the interfacial peeling stress of a thermostat structure. L. B. Freud et al [65] extended Stoney's formula for configurations with thin substrates or large deformations, which break two main assumptions of Stoney's formula: (1). the film's thickness is much less than the substrate's thickness and both the film and substrate thickness are small compared to lateral dimensions; (2). the strains and deformations are intestinally small. Both Stoney and Timoshenko's formulae have long been one of the most important tools for understanding the deformations and thermomechanical stresses for single-layered

structures like deposited metal thin film on substrates. Nowadays a few extensions of Stoney's formula for multilayer applications are not only useful but also necessary [66-72] and their specific applications on optical thin film coating [73, 74] and thin solder layer for multilayer electronic assembly [75] have been investigated.

It should be noted that Stoney's formulae actually is a good approximation of Timoshenko's theory in the case of a thin film deposited on a relative thick substrate and the thickness ratio of two layers should be less than 0.1. In most microelectronic fabrications, in comparison with the thickness of normal silicon substrates of more than 700 μm , the thickness of deposited thin film materials ranging from several nm to a few μm is so thin that it meets the assumptions of modified Stoney's equation. By measuring the curvature or the warpage of silicon substrates, stresses caused by thin films deposited can be easily estimated. However, in MEMS applications, the thickness ratio of two materials may not be limited within 0.1 so modifications on Timoshenko's formula for multilayer applications are highly required as a more general case. It makes no assumptions regarding the thickness of the layers and produces a linear set of equations that admit a solution which can be expressed in a closed form [76].

Governing equations:

$$\text{Force equilibrium} \quad \sum_{i=1}^N P_i = 0 \quad (3.2)$$

$$\text{Moment equilibrium} \quad \sum_{i=1}^N M_i - \sum_{i=1}^{N-1} P_i \delta_i = 0 \quad (3.3)$$

Noting that $M_i = E_i I_i / \rho$, above equation can be rewritten as

$$\frac{1}{\rho} \sum_{i=1}^N E_i I_i - \sum_{i=1}^N P_i \delta_i = 0 \quad (3.4)$$

Compatibility of strain at layers' interfaces, for $i=1, 2, \dots, N-1$ one must have

$$(\epsilon_{thermal} + \epsilon_{axial} + \epsilon_{bending})_i = (\epsilon_{thermal} + \epsilon_{axial} + \epsilon_{bending})_{i+1} \quad (3.5)$$

$$\alpha_i T + \frac{P_i}{A_i E_i} + \frac{h_i}{2\rho} = \alpha_{i+1} T + \frac{P_{i+1}}{A_{i+1} E_{i+1}} - \frac{h_{i+1}}{2\rho} \quad (3.6)$$

Finally, these equations can be reduced by a linear system of $L=N+1$ equations that can be solved to determine P_1, P_2, \dots, P_N and $1/\rho$. Cases with $N=2, 3, 4$ layers assemblies are discussed as follows:

$N=2$: equivalent to Timoshenko's formula (3.1)

$$\begin{bmatrix} \frac{1}{E_1 h_1} & -\frac{1}{E_2 h_2} & \frac{h_1+h_2}{2} \\ 1 & 1 & 0 \\ \frac{h_1+h_2}{2} & 0 & -\sum_{i=1}^2 E_i I_i \end{bmatrix} \cdot \begin{bmatrix} P_1 \\ P_2 \\ \frac{1}{\rho} \end{bmatrix} = \begin{bmatrix} (\alpha_2 - \alpha_1) \Delta T \\ 0 \\ 0 \end{bmatrix} \quad (3.7)$$

$N=3$: appeared in [3.15]

$$\begin{bmatrix} \frac{1}{E_1 h_1} & -\frac{1}{E_2 h_2} & 0 & \frac{h_1+h_2}{2} \\ 0 & \frac{1}{E_2 h_2} & -\frac{1}{E_3 h_3} & \frac{h_2+h_3}{2} \\ 1 & \frac{1}{E_3 h_3} & 1 & 0 \\ \frac{h_1}{2} + h_2 + \frac{h_3}{2} & \frac{h_2+h_3}{2} & 0 & -\sum_{i=1}^3 E_i I_i \end{bmatrix} \cdot \begin{bmatrix} P_1 \\ P_2 \\ P_3 \\ \frac{1}{\rho} \end{bmatrix} = \begin{bmatrix} (\alpha_2 - \alpha_1) \Delta T \\ (\alpha_3 - \alpha_2) \Delta T \\ 0 \\ 0 \end{bmatrix} \quad (3.8)$$

$N=4$: following A. O. Cifuentes' scheme, $N=4$ layer should have $L=5$ matrix in the following form and be similar to the equations shown above.

$$\begin{bmatrix} \frac{1}{E_1 h_1} & -\frac{1}{E_2 h_2} & 0 & 0 & \frac{h_1+h_2}{2} \\ 0 & \frac{1}{E_2 h_2} & -\frac{1}{E_3 h_3} & 0 & \frac{h_2+h_3}{2} \\ 0 & 0 & \frac{1}{E_3 h_3} & -\frac{1}{E_4 h_4} & \frac{h_3+h_4}{2} \\ 1 & 1 & 1 & 1 & 0 \\ \frac{h_1}{2} + h_2 + h_3 + \frac{h_4}{2} & \frac{h_2}{2} + h_3 + \frac{h_4}{2} & \frac{h_3+h_4}{2} & 0 & -\sum_{i=1}^4 E_i I_i \end{bmatrix} \cdot \begin{bmatrix} P_1 \\ P_2 \\ P_3 \\ P_4 \\ \frac{1}{\rho} \end{bmatrix} = \begin{bmatrix} (\alpha_2 - \alpha_1) \Delta T \\ (\alpha_3 - \alpha_2) \Delta T \\ (\alpha_4 - \alpha_3) \Delta T \\ 0 \\ 0 \end{bmatrix}$$

(3.9)

Physical properties of some commonly used materials in microfabrication are listed in Table. 3.2. In Table 3.2 all kinds of materials is divided into three groups: semiconductor substrate including Si, SiO_2 and Ge, metal thin film and polymer including SU8 which is widely used in microfluidic and bioMEMS applications.

Table 3.2 Physical properties of materials commonly used in microfabrication

| Material | Density ($g.cm^{-3}$) | Young's modulus (GPa) | CTE ($\mu m.m^{-1}.K^{-1}$) | Heat Capacity ($J.mol^{-1}.K^{-1}$) | Thermal Conductivity ($W.m^{-1}.K^{-1}$) |
|----------|----------------------------|---------------------------------|----------------------------------|--|--|
| Si | 2.329 | 165 | 2.49 | 0.71 | 1.49 |
| SiO_2 | 2.2 | 75 | 0.4 | 1 | 1.4 |
| Ge | 5.323 | 102 | 5.75 | 0.32 | 0.6 |
| Al | 2.7 | 68 | 24 | 0.902 | 2.37 |
| Au | 19.3 | 77 | 14.4 | 0.129 | 3.18 |
| Cr | 7.19 | 279 | 4.9 | 0.45 | 0.939 |
| Ti | 4.506 | 110 | 9 | 0.52 | 0.219 |
| Cu | 8.96 | 110 | 16.4 | 0.385 | 4.01 |
| Pt | 21.45 | 168 | 8.8 | 0.13 | 0.716 |
| SU8 | 1.2 | 4 | 60 | 1.6748 | 0.2 |

Eq. 3.7-3.9 has been used to optimize the thickness ratio of multilayer composite beam in order to find the largest mechanical deflection. Similar works on how to select appropriate materials and optimize the performance of electrothermal actuators [77, 78]

have been reported. However only two-layer composite beam was considered, which still has limitation to accurately predict the performance of actual multilayer composite beam even in most actual multilayer case may be approximated by a simplified two-layer alternative. Therefore in my study Eq. 3.8 and 3.9 has been used to directly calculate the performance of multilayer composite beam with better accuracy. The performance considered here mainly focuses on the mechanical deflection of the electrothermal actuator as well as its thermal response time. Material combinations that can perform a large angle or vertical displacement at their tips, when actuated under certain thermal loads conditions are suitable candidates for applications such as MEMS scanners. The primary objective of the study is to identify candidate materials in the preliminary phase of electrothermal actuator design. In addition, passive heat dissipation, heat transfer at the microscale and estimation of maximum permissible heating temperature are not discussed in this study. Deformation of all materials involved in this study is considered as pure elastic deformation not plastic or elastoplastic deformation. These factors clearly require consideration in the detailed design of an electrothermal actuator. Examples of numerical analysis based on Eq. 3.7-3.9 have been conducted and given as follows. The temperature change is arbitrarily selected as 50K.

Study 1: metal thin films on Si substrate. The thickness of Si substrate is fixed at 2 μm and thickness variations of metal thin films have been used in the calculation.

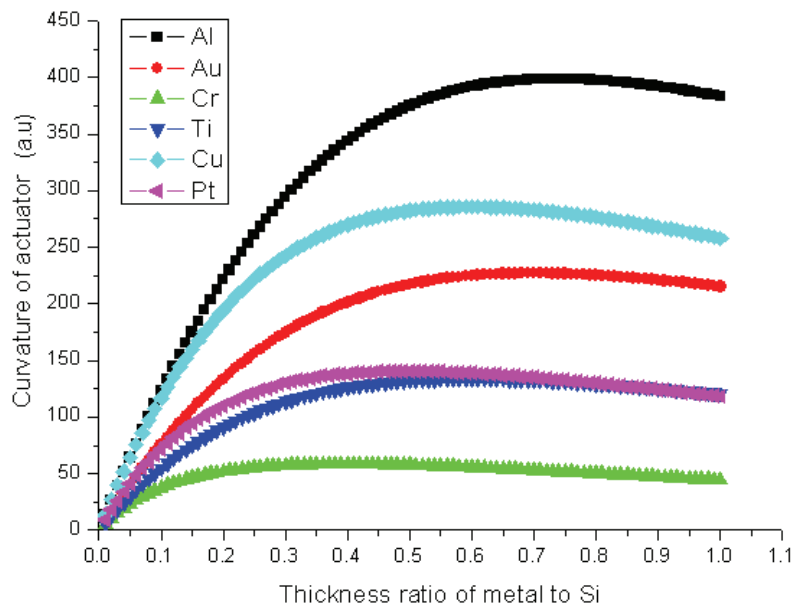


Figure 3.2 Curvatures of different metal-Si combinations with various thickness ratios.

Study 2: metal thin films on SiO_2 substrate. The thickness of SiO_2 substrate is also fixed at 2 μm and thickness variations of metal thin films have been used in the calculation.

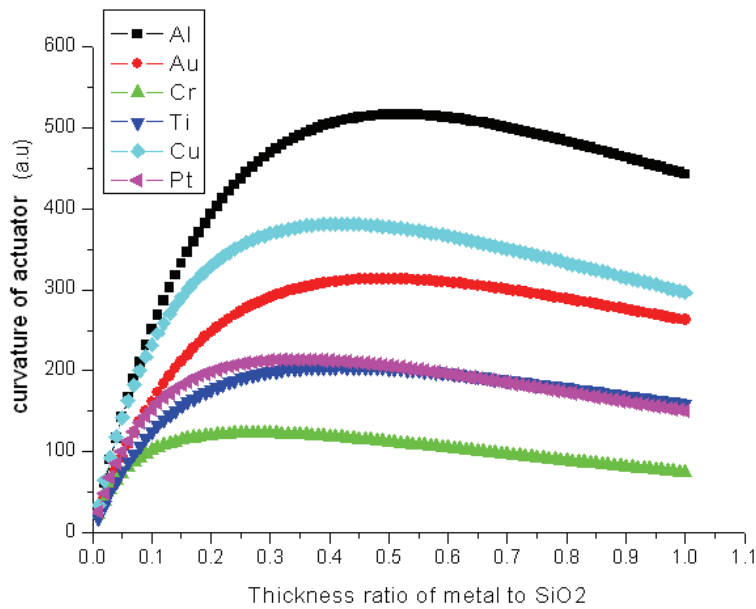


Figure 3.3 Curvatures of different metal- SiO_2 combinations with various thickness ratios.

Study 3: metal thin films on Ge substrate. The thickness of Ge substrate is also fixed at 2 μm and thickness variations of metal thin films have been used in the calculation. Since Ge wafers limited by its 6 inches size cannot be processed in IME's cleanroom, this study exhibits only as a reference.

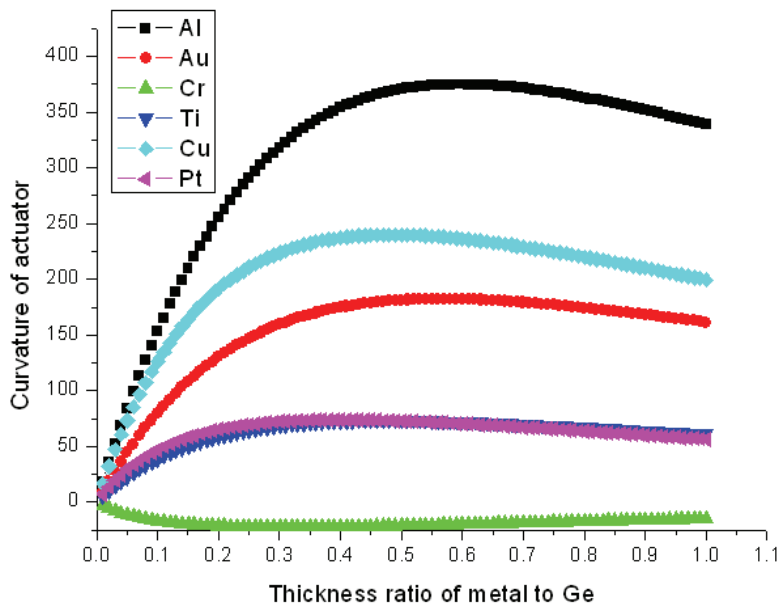


Figure 3.4 Curvatures of different metal-Ge combinations with various thickness ratios.

Study 4: metal thin films on SU8 substrate. The thickness of SU8 substrate is fixed at 2 μm and thickness variations of metal thin films have been used in the calculation. SU8 is a widely used epoxy based negative photoresist and can be spun over a thickness ranging from a few μm to several mm. In addition, SU8-Si combination is also included in this study since this combination shows the significant improvement on the deflection capability over conventional Al / Si combination.

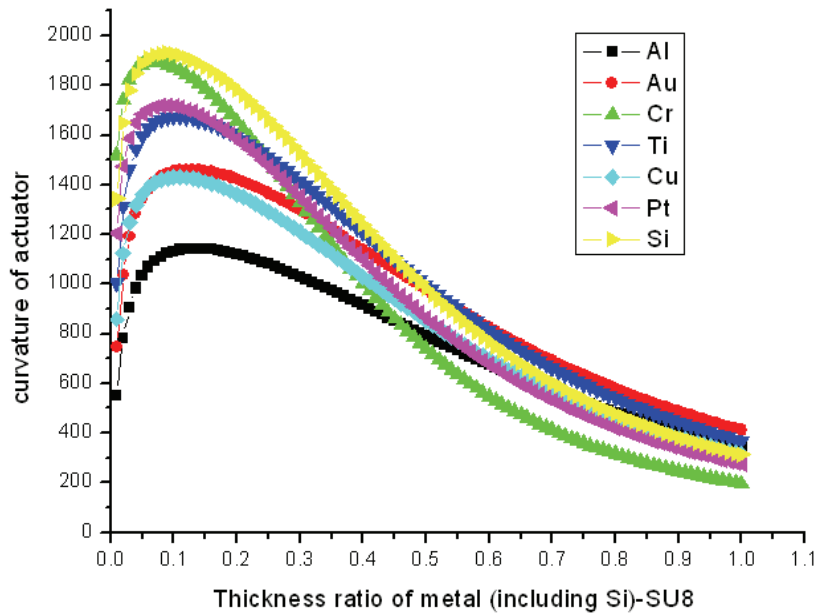


Figure 3.5 Curvatures of different metal (including Si)-Ge combinations with various thickness ratios.

Table 3.3 shows a comparison of a few commonly used metal thin films that exhibit significant mechanical deflection on four kinds of substrates (*Si*, SiO_2 , Ge and SU8). As expected, metals on SiO_2 deliver a large deflection since SiO_2 has very small CTE as well as moderate Young's modulus which is comparable to the metal thin films deposited on it. Moreover, metals/Si on SU8 show a impressive performance of mechanical deflection due to the significant high CTE and low Young's modulus of SU8.

Table 3.3 Summary of numerical analyses on deflection of two-layer composite beams under 50K thermal loads (Substrate thickness is fixed at 2 μm)

| Substrates Thin films | Silicon | | SiO_2 | | Ge | | SU8 | |
|--------------------------|--------------------------|---------------|--------------------------|---------------|--------------------------|---------------|--------------------------|----------------|
| | Opti. thick. ratio | Curv. | Opti. thick. ratio | Curv. | Opti. thick. ratio | Curv. | Opti. thick. ratio | Curv. |
| Al | 0.74 | 398.8 3093 | 0.52 | 516.2 1482 | 0.6 | 374.871 62 | 0.13 | 1143.2 452 |
| Au | 0.7 | 226.9 624 | 0.49 | 313.3 976 | 0.57 | 182.151 76 | 0.13 | 1461.2 3655 |
| Cr | 0.4 | 58.66 661 | 0.27 | 123.0 2396 | 0.32 | -22.2569 | 0.07 | 1894.3 6823 |
| Ti | 0.6 | 133.7 2133 | 0.42 | 204.9 5751 | 0.48 | 73.2287 8 | 0.11 | 1673.0 1044 |
| Cu | 0.6 | 285.7 2407 | 0.42 | 381.3 1629 | 0.48 | 239.965 07 | 0.11 | 1430.2 599 |
| Pt | 0.5 | 140.6 8689 | 0.35 | 214.0 7425 | 0.4 | 73.9328 3 | 0.09 | 1719.7 9098 |
| Si | | | | | | | 0.09 | 1930.0 5135 |

From Eq. 3.1, it is obvious that the deflection of the biomaterial structure depends on the material selected (qualified by E, n and Δa), the thickness ratio m, given temperature

change ΔT and total thickness h . Since E , n and a are natural properties of materials, the main task to obtain the maximum deflection becomes how to find the optimized thickness ratio m . A normalized curvature θ is derived from Eq. 3.1 and listed as follows:

$$\theta = \frac{\frac{1}{\rho}t_2}{6\Delta T} = \frac{\frac{1}{\rho}t_2}{6\Delta T} = \frac{\Delta\alpha(1+m)^2}{3(1+m)^2 + (1+mn)\left(m^2 + \frac{1}{mn}\right)} \quad (3.10)$$

To maximize the normalized curvature for given materials, the derivative of θ should be equations to zero. The derivative of θ is found to be:

$$\theta' = \frac{2(1+m)}{3(1+m)^2 + (1+mn)\left(m^2 + \frac{1}{mn}\right)} - \frac{(1+m)^2\left(6+6m+n\left(m^2 + \frac{1}{mn}\right) + (1+mn)\left(2m - \frac{1}{m^2n}\right)\right)}{\left(3(1+m)^2 + (1+mn)\left(m^2 + \frac{1}{mn}\right)\right)^2} = 0 \quad (3.11)$$

Only one positive root among 6 roots of is found by solving Eq. (3.11),

$$m_{opt} = \frac{1}{\sqrt{n}} \quad (3.12) [87]$$

By substituting Eq. 3.11 into Eq. 3.10, the maximum normalized curvature θ_{opt} is found as,

$$\theta_{opt} = \frac{\Delta\alpha}{4} \quad (3.13) [87]$$

From Eq. 3.13, it is clear that the maximum normalized curvature for a thermally actuated bimaterial is dependent only on the difference in thermal expansion coefficients, of the two materials. Moreover, the optimized thickness ratio does depend on the modulus ratio.

Apart from thermomechanical stresses and mechanical deflections, thermal response time is another critical considerations for some specific applications of multilayer composite beam, such as micromechanical calorimeters [78-80], uncooled focal plane array (FPA) for IR imaging [81-83] and electrothermal actuators [84-86]. Actually sensitivity is also very important for sensing applications of multilayer composite beams,

in my study of electrothermal actuation it is exclusive. The thermal response time of a two-layer sensor under a constant temperature along its length was expressed as:

$$\tau = \frac{l^2 dc}{\lambda} \quad (3.14)$$

in [78] and a more specific expression was given in [79] as:

$$\tau = l^2 \frac{d_1 C_1 t_1 + d_2 C_2 t_2}{\lambda_1 t_1 + \lambda_2 t_2} \quad (3.15)$$

This equation is not valid when there is a temperature variation on the sensor leading to a smaller time constant. Because thermal energy is already stored in the sensor. Therefore the Eq. 3.10 can be modified as:

$$\tau = \frac{l^2}{2} \frac{d_1 C_1 t_1 + d_2 C_2 t_2}{\lambda_1 t_1 + \lambda_2 t_2} \quad (3.16) \text{ when the sensor is heated only at its end and}$$

$$\tau = \frac{l^2}{3} \frac{d_1 C_1 t_1 + d_2 C_2 t_2}{\lambda_1 t_1 + \lambda_2 t_2} \quad (3.17) \text{ when the sensor is heated along its entire length.}$$

A similar analysis has been conducted to identify appropriate material combinations for fast switching applications and estimate the thermal response time of selected material combinations by mainly using Eq. 3.15.

Study 5: metal thin films on Si substrate. The thickness of Si substrate is fixed at 2 μm and thickness variations of metal thin films have been used in the calculation.

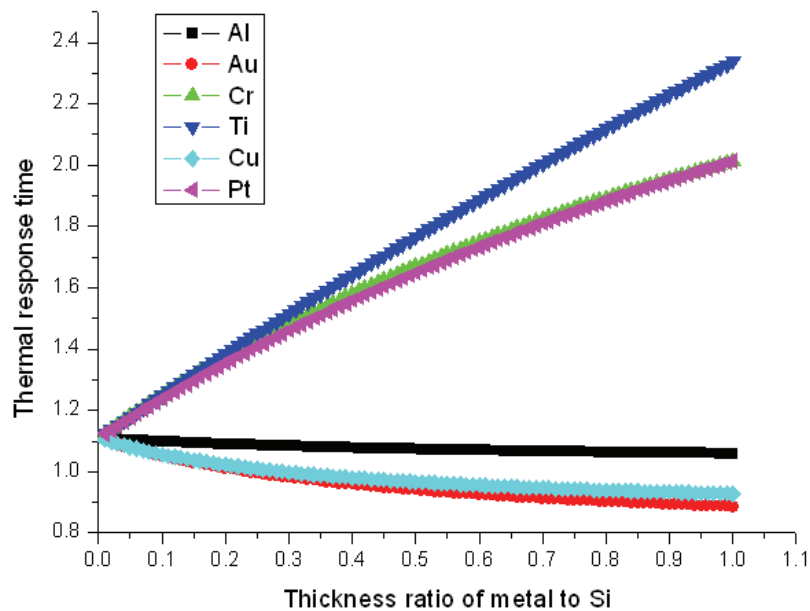


Figure 3.6 Thermal response time of different metal-Si combinations with various thickness ratios.

Study 6: metal thin films on SiO_2 substrate. The thickness of SiO_2 substrate is fixed at 2 μm and thickness variations of metal thin films have been used in the calculation.

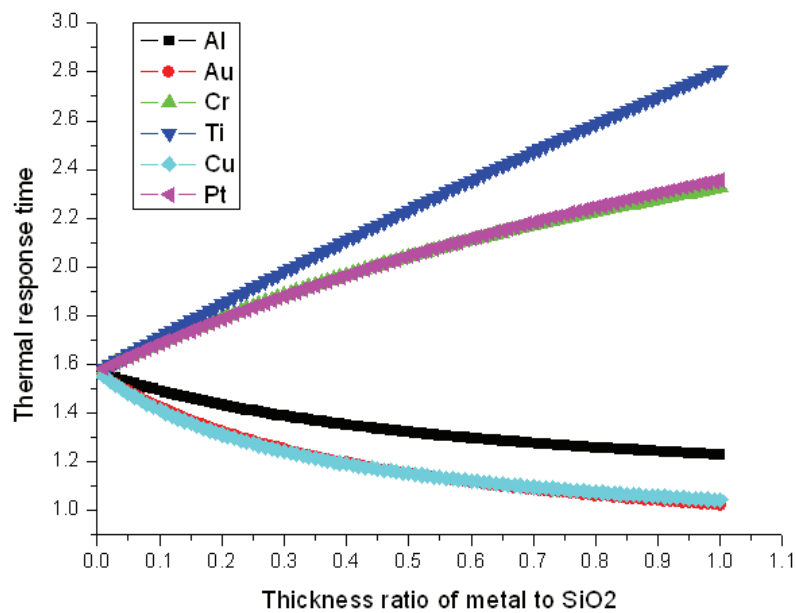


Figure 3.7 Thermal response time of different metal- *SiO₂* combinations with various thickness ratios.

Study 7: metal thin films on Ge substrate. The thickness of Ge substrate is fixed at 2 μm and thickness variations of metal thin films have been used in the calculation.

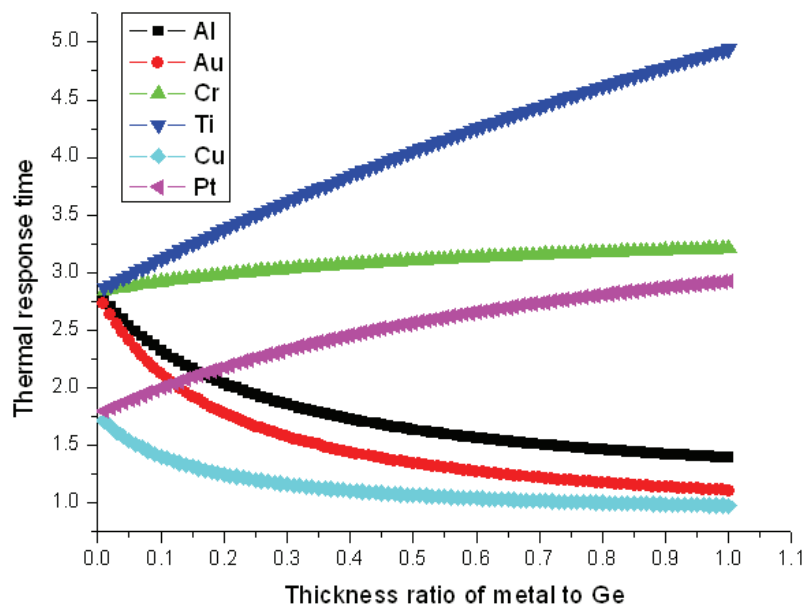


Figure 3.8 Thermal response time of different metal-Ge combinations with various thickness ratios.

Study 8: metal thin films on SU8 substrate. The thickness of SU8 substrate is fixed at 2 μm and thickness variations of metal thin films have been used in the calculation.

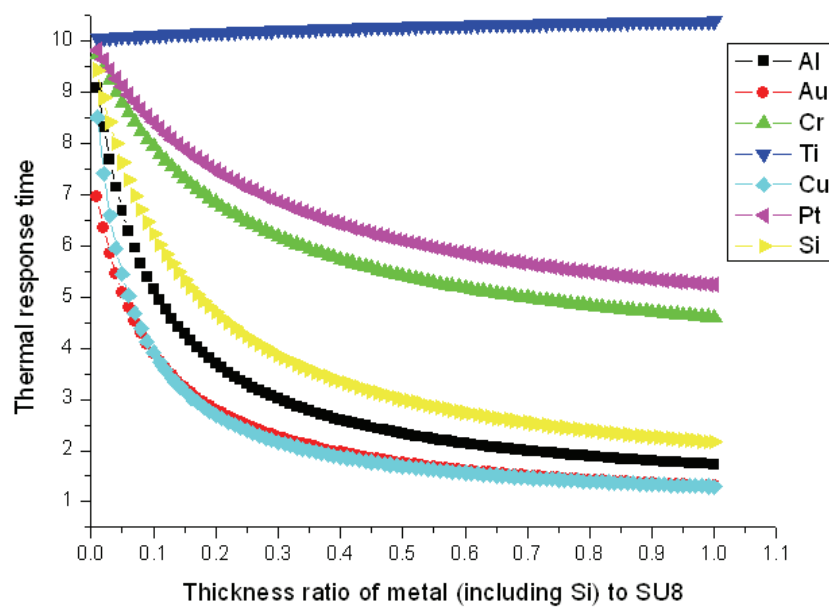


Figure 3.9 Thermal response time of different metal (including Si)-SU8 combinations with various thickness ratios.

Table 3.4 Summary of numerical analyses on thermal response time of two-layer composite beams with optimized thickness ratio for largest deflection. (Substrate thickness is fixed at 2 μm)

| Substrates Thin films | Silicon | | SiO_2 | | Ge | | SU8 | |
|--------------------------|--------------------------|--------------|--------------------------|--------------|--------------------------|---------------|--------------------------|--------------|
| | Opti. thick. ratio | Res. time | Opti. thick. ratio | Res. time | Opti. thick. ratio | Res. time | Opti. thick. ratio | Res. time |
| Al | 0.74 35 | 1.065 35 | 0.52 82 | 1.316 82 | 0.6 82 | 1.56508 82 | 0.13 5 | 4.5785 5 |
| Au | 0.7 99 | 0.913 99 | 0.49 09 | 1.156 09 | 0.57 09 | 1.29424 09 | 0.13 3 | 3.4651 3 |
| Cr | 0.4 08 | 1.580 08 | 0.27 8 | 1.858 8 | 0.32 8 | 3.0414 8 | 0.07 8 | 8.4154 8 |
| Ti | 0.6 93 | 1.886 93 | 0.42 15 | 2.134 15 | 0.48 15 | 4.01075 15 | 0.11 72 | 10.118 72 |
| Cu | 0.6 69 | 0.955 69 | 0.42 07 | 1.183 07 | 0.48 07 | 1.07698 07 | 0.11 4 | 3.7267 4 |
| Pt | 0.5 26 | 1.649 26 | 0.35 13 | 1.924 13 | 0.4 13 | 2.45799 13 | 0.09 9 | 8.5491 9 |
| Si | | | | | | | 0.09 9 | 6.4608 9 |

3.2 MODELING OF TWO-AXIS GIMBAL-LESS STRUCTURE

Two-axis micromirror is a key technology to enable tip and tilt, i.e., two DOF actuation. The commonly used method to implement two-axis rotation is by employing gimbaled structures. A gimbaled structure consists of two independent rotation axes, one inner fast axis and another outer slow axis. The main advantage of a gimbaled structure lies in that the rotations of the two axes of gimbaled structures are physically decoupled. However, eliminating crosstalk between drive signals and mechanical coupling may require complex fabrication process. Non uniformity in scanning frequencies can also render it useless for many applications, especially in high speed scanning applications. Moreover, the gimbaled structures occupy large areas and sacrifice the fill factor of the micromirrors.

In gimbal-less structures, all actuators normally have uniform characteristics and are relatively easier to fabricate. Simple fabrication processes have been applied to implement two-axis scanning micromirrors utilizing electrostatic comb drive, electrothermal and electrostatic parallel plate actuators. This study relates to a two-axis gimbal-less electrothermal scanning micromirror developed for 3D free space optical switching. This micromirror consists of four Aluminum (Al)-Silicon (Si) bimorph actuators, four planar springs and a mirror plate coated with a high reflective gold thin film. The motions of two axes of gimbal-less structure are not physically decoupled as is the case for gimbaled structures. Hence the mechanical deflection of the mirror plate depends on all the actuators and their mechanical characteristics, deformation of one actuator results in deformation of other actuators and tilt of the mirror plate. In this study the behavior of a two-axis gimbal-less scanning micromirror has been modeled as a

spatial four-spring and plate system. Numerical simulation has been carried out. The study shows that model is very useful in optimizing design parameters and in predicting micromirror performance.

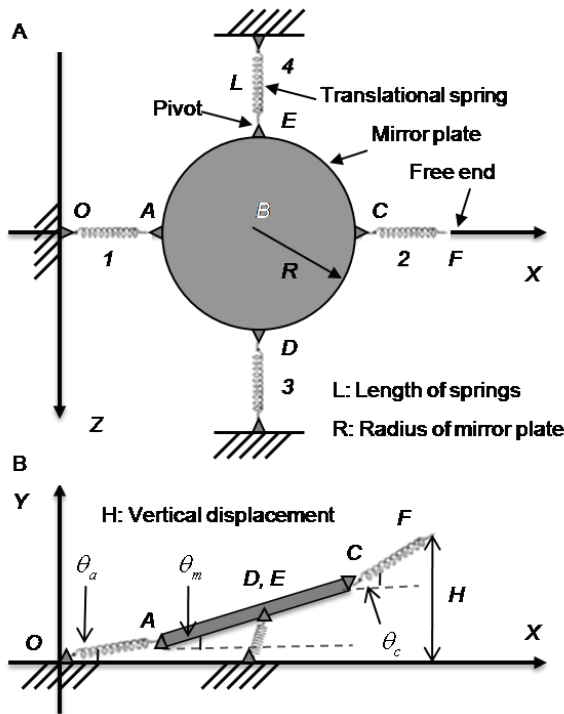


Figure 3.10 Top-view (a) and side-view (b) of the spatial four-spring and plate system. (From figure 2 in [88]).

As aforementioned, the modeling strategy employed in this paper is to simplify the actual two-axis micromirror design as a spatial four-spring and plate system (Fig. 3.10). Each of the all four springs has one end attached to four fixed pivots placed on the circular mirror plate. In the model, three springs have the other end attached to fixed pivots while the one spring has a free end. These springs are assumed to behave linearly elastically and have the same properties, i.e., linear spring characteristics with the same free length and the

same spring elasticity constant. A vertical displacement applied at the free end of the spring is used to simulate the vertical displacement at the tip of an Al-Si bimorph actuator and determines the equilibrium position(s) of the system and the forces acting in the coupling elements. Similar compliant mechanical structures are widely used as mounting or support structures as well as parallel mechanisms or robot manipulators. The geometric and mechanical parameters used in the model are listed in Table 3.5.

Table 3.5 Geometric and mechanical parameters of the model (From table 1 in [88])

| Parameters | Symbols |
|------------------------------|-------------------------|
| Geometric | |
| Vertical displacement at F | H |
| Radius of mirror | R |
| Free length of springs | L |
| Lengths of extended springs | L with subscript |
| Angles of springs and mirror | θ with subscript |
| Coordinates of points | x, y with subscript |
| Mechanical | |
| Elastic forces of springs | F with subscript |
| Moments on mirror | M with subscript |

In this study, we provide a drive signal to an actuator for single axis rotation rather than differentially drive opposite two actuators. This kind of non-differential drive scheme is expected to provide a simpler way to tilt the mirror plate. So in our study we pay more

attention on the investigation of how such a non-differential drive scheme affect two-axis gimbal-less structures.

First of all, geometric constraints of each spring projected on the X and Y axes provide the following scalar equations:

$$\text{For spring 1: } x_a^2 + y_a^2 = L_1^2 \quad (3.18)$$

$$\text{For spring 2: } (2 * L + 2 * R - x_a)^2 + (H - y_c)^2 = L_2^2 \quad (3.19)$$

where,

$$x_c = x_a + 2 * R * \cos\theta_m \quad (3.20)$$

$$y_c = y_a + 2 * R * \sin\theta_m \quad (3.21)$$

For spring 3 and 4:

$$(x_d - L - R)^2 + y_d^2 + L^2 = L_3^2 \quad (3.22)$$

where,

$$x_d = x_a + R * \cos\theta_m \quad (3.23)$$

$$y_d = y_a + R * \sin\theta_m \quad (3.24)$$

Secondly, the equilibrium of the forces and moments on the mirror plate in X and Y axes yields:

Force Equilibrium:

$$\text{In x axis, } F_{2x} = F_{1x} + F_{3x} + F_{4x} \quad (3.25)$$

$$\text{In y axis, } F_{2y} = F_{1y} + F_{3y} + F_{4y} \quad (3.26)$$

After expansion and substitute Eq. 3.20, 3.21, 3.23 and 3.24 into Eq. 3.25 and 3.26, we get following equations:

$$(L_2 - L) \frac{2*L+2*R-x_a-2*R*cos\theta_m}{L_2} = (L_1 - L) \frac{x_a}{L_1} + 2 * (L_3 - L) \frac{x_a+R*cos\theta_m-L-R}{L_3} \quad (3.27)$$

$$(L_2 - L) \frac{H-y_a-2*R*sin\theta_m}{L_2} = (L_1 - L) \frac{y_a}{L_1} + (L_3 - L) \frac{y_a+R*sin\theta_m}{L_3} \quad (3.28)$$

Moment Equilibrium:

$$\sum M = 0 \quad (3.29)$$

and after expansion and variables substitution,

$$(L_1 - L) \sin \left(\theta_m - \arctan \left(\frac{y_a}{x_a} \right) \right) = (L_2 - L) \sin \left(\arctan \left(\frac{H-y_a-2*R*sin\theta_m}{2*L+2*R-x_a-2*R*cos\theta_m} \right) - \theta_m \right) \quad (3.30)$$

Finally we have a group of ten nonlinear equations composed of Eq. 3.18-3.24, Eq. 3.27, Eq. 3.28 and 3.30 based on geometric constraints, force equilibrium and moment equilibrium, respectively. In these equations, there are ten unknown parameters which describe the positions and tilting angles of all four springs and the mirror plate. For the system shown in Fig. 3.10, the spring free lengths L and the radius of the mirror plate R as well a given load H as are known a priori.

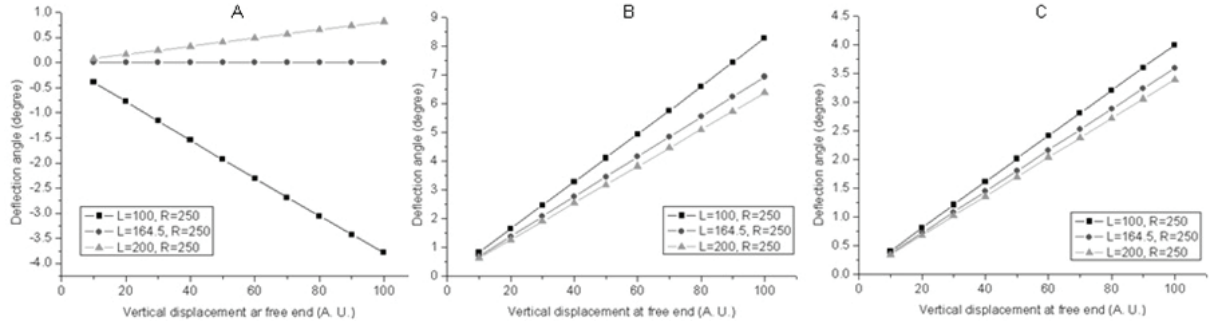


Figure 3.11 Deflection angles versus vertical displacement at free end of (a) spring 1, (b) mirror plate and (c) spring 2 (From figure 3 in [88])).

The radius of mirror plate R was assigned as 250 which is the same as the actual size of the mirror plate and the spring free lengths L were arbitrarily assigned as 100, 164.5 and 250 as a variation of three examples for study. In order to simulate the vertical motion of an excited actuator, a parameter H ranging from 10 to 100 was used as the input of the model.

Fig. 3.11 illustrates the resultant deflection angles of spring 1, mirror plate and spring 2 as responses to the vertical displacement applied on the free end of spring 2. In Fig. 3.11 (a) the example with the spring free length of 100 has a negative deflection angle showing the point A moved downwards. However, the example with the spring free length of 164.5 has nearly zero displacement in Y axis while the other example with the spring free length of 200 performed a positive deflection angle. It is well known, micromirrors with high fill factor are highly desired in some applications, such as SLM and endoscopic imaging. The example with shorter spring free length can save more space and has a larger fill factor. However, for a design with too short spring free length,

before the mirror plate sufficiently elevated, it has a large rotational angle which may lead to light blocked by surrounding wafer. Fig. 3.11 shows the deflection angles of all examples with different spring free lengths are quite linear with the vertical displacement at the free end of spring 2.

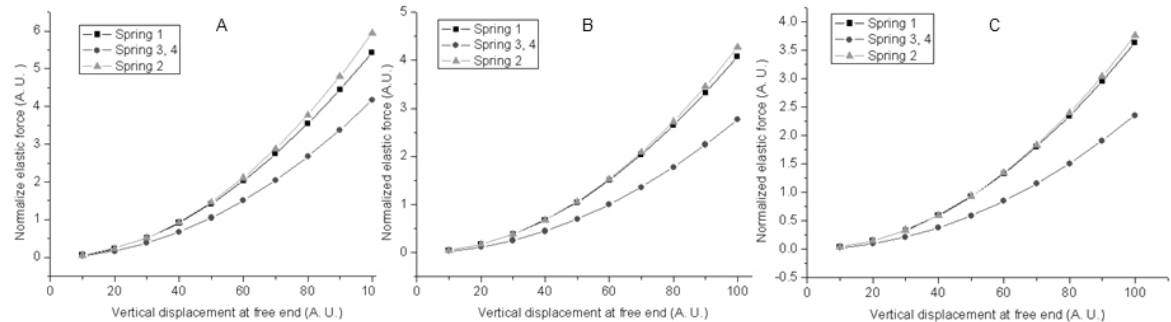


Figure 3.12 Normalized elastic force versus vertical displacement at free end in examples with the spring free length of (a) 100, (b) 164.5 and (c) 250 (From figure 4 in [88])).

Simulated elastic forces generated by the extension of the springs have been shown in Fig. 3.12. Since in our model the elastic constant of springs has been eliminated during the equation derivation, the relative extensions of the springs have been used to express the elastic forces. Fig. 3.12 shows that in all examples the force in spring 1 is always larger than those in other three springs. In the two lateral springs, spring 3 and 4, due to the orthogonal position to the X-Y plane, there is far smaller force in comparison with other two springs, spring 1 and 2, locating in the X-Y plane. As the free length of springs increases, the force difference between spring 1 and 2 decreases gradually.

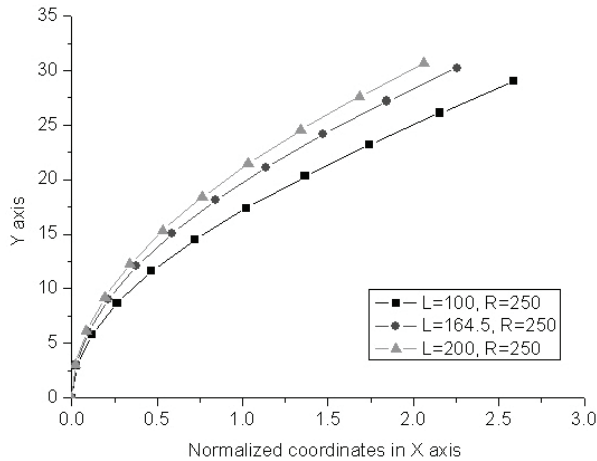


Figure 3.13 Lateral shift trajectory of the centroid of the mirror plate (From figure 5 in [88])).

Lateral shift of the mirror plate may lead to degradation of optical transmission quality, therefore, in the design of optical MEMS scanners lateral shift should be paid more attention and be suppressed as much possible as one can. Fig. 3.13 shows evaluation of the lateral shift in the two-axis gimbal-less structures with the non-differential drive scheme. From Fig. 3.13 we can find that the example with longer spring free length has less lateral shift but more vertical elevation in comparison with those with shorter spring free length under the same H. It can be observed that after an initial nonlinear region the lateral shift trajectories of the centroid of the mirror plate become quite linear. The example with longer spring free length has a steeper slope of the linear trajectory region in comparison to those with shorter spring free lengths. The lateral shift of the mirror plate is less than 1% of the overall dimension of the mirror plate, hence its effect can be assumed negligible.

Table 3.6 Comparison of examples with different spring free length (From table 2 in [88])

| Examples | Fill factor | Angle | Force | Lateral shift |
|--------------|-------------|-------|-------|---------------|
| Long spring | Low | Low | Low | Low |
| Short spring | High | High | High | High |

As a conclusion, according to the simulation results shown above, the comparison of examples with different spring free length has been listed in Table. 3.6.

The main limitation of our model is in neglecting the stiffness and torsion properties of all springs, especially of the two lateral springs, spring 3 and 4, which mainly behave as two torsional bars during the rotation of the mirror plate, however, still the model is reasonably accurate and useful. The presented model describes the motion of two-axis gimbal-less structures utilizing geometric and mechanical analysis. In order to make it more generalized, the properties of real actuators have been simplified into a simple parameter H. Actually the displacement at the tip of the spring may be nearly vertical in small angular deflection, or even quite nonlinear. So the model will need fine tuning for a more accurate theoretical behavior.

A quantitative model was developed for the study of a two-axis gimbal-less scanning micromirror. Two-axis gimbal-less micromirror was modeled as a spatial four-spring and

plate system and the results show that its response is quite linear. The related mechanics has been also investigated.

CHAPTER 4

MICROMACHINED ELECTROTHERMAL SCANNERS: DESIGNS, FABRICATION PROCESS AND CHARACTERIZATION

4.1 MICROMACHINED ELECTROTHERMAL SCANNERS DESIGNS

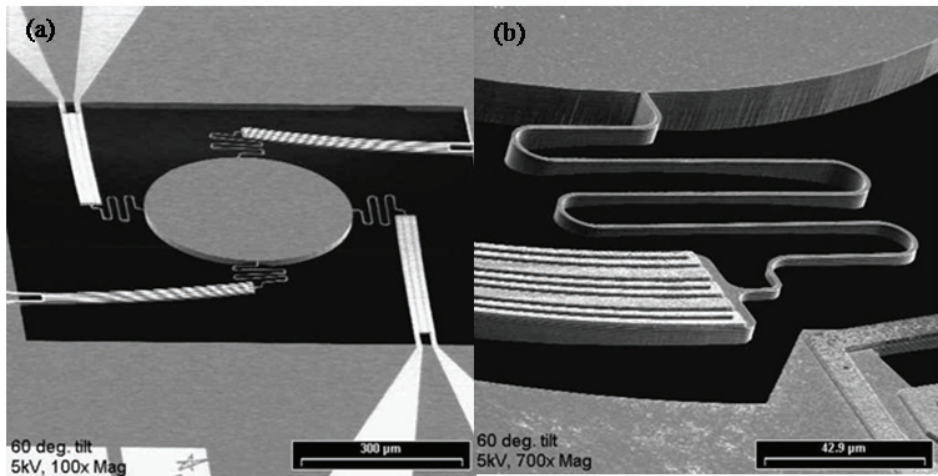


Figure 4.1 SEM micrographs of (a) 3D micromirror with straight actuators and (b) A close up view of an actuator, a spring and a mirror plate. (Redraw from Fig. 1 in [30]).

Our study on 3D micromirror for optical communication network switching applications was published earlier in 2005 [30]. The specifications of the device included deflections up to 10° out of the plane in 3D space, switching speed of 10 ms, the radius of curvature of 30 cm, and reliability testing up to 100 million switching cycles. In the following sections of this chapter, Designs, fabrication process and characterization of novel micromachined electrothermal scanners will be reported.

4.1.1 TWO-AXIS GIMBAL-LESS ELECTROTHERMAL SCANNERS BASED ON CURVED ACTUATORS

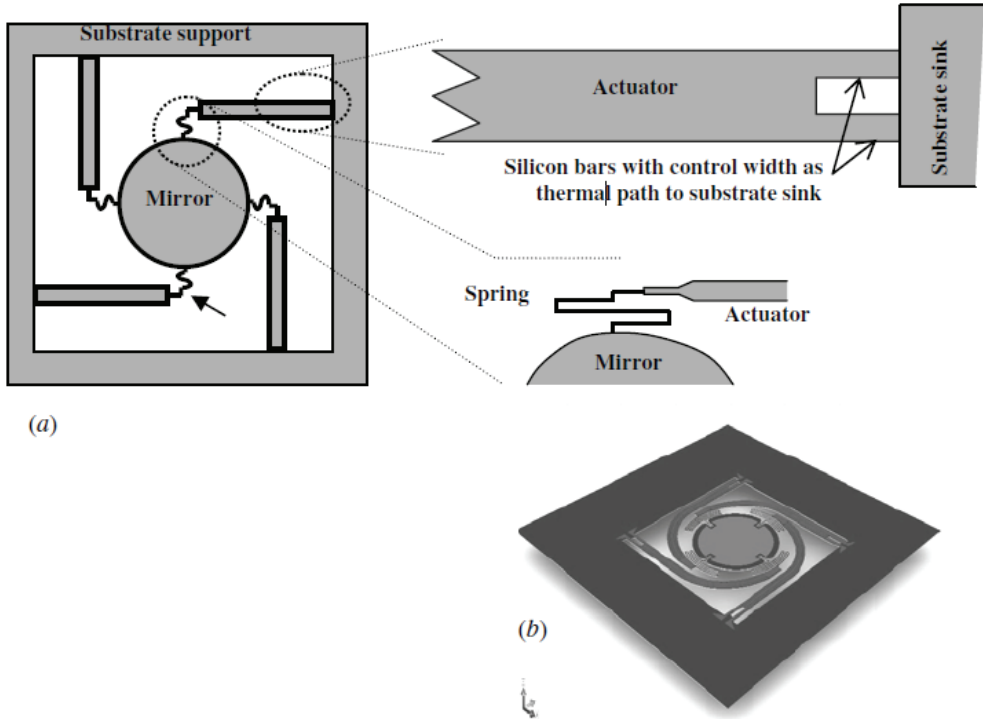


Figure 4.2 Electro-thermally actuated 3D micromirror design: (a) linear actuators and (b) curved actuators. (From Figure 3 in [89]).

The basic design of the micromirror is shown in Fig. 4.2. The thermal actuators are formed of a $2\text{ }\mu\text{m}$ thick silicon cantilever as the base and a $1\text{ }\mu\text{m}$ thick Al heater patterned on it. The resistance of the heater is designed to be at $100\text{ }\Omega$. The Al heater also functions as bimorph material for thermal actuation. On heating, Al expands more than silicon and the composite beam bends downward. Selective bending of the four actuators is managed by electronic control to obtain the desired switching orientation of the mirror. The straight line scanning, which is needed for an optical coherence tomography image, can also be achieved using the same procedure. The developed test chip had micromirrors with a reflecting plate of $4\text{ }\mu\text{m}$ thickness and 200 to $500\text{ }\mu\text{m}$ diameter; actuators of 1.5 to

2.5 μm thickness, 250 to 800 μm length and 26 to 40 μm width, and springs of the same thickness as actuators, 300 to 500 μm in length, and 2 μm width. The test chip also included curved beam composite thermal actuators and curved flexure serpentine springs, which were designed with the same shape (curvature) as the outer diameter of the micromirror plate. These modifications in comparison to the previous development [30] made the design compact with significantly reduced dead space, which allowed 1 mm \times 1 mm chip size micromirror devices with a 400 μm diameter micromirror plate. A micromirror design with curved actuators and springs is shown in Fig. 4.2 (b).

4.1.2 TWO-AXIS GIMBAL-LESS ELECTROTHERMAL SCANNERS BASED ON FOLDED ACTUATORS

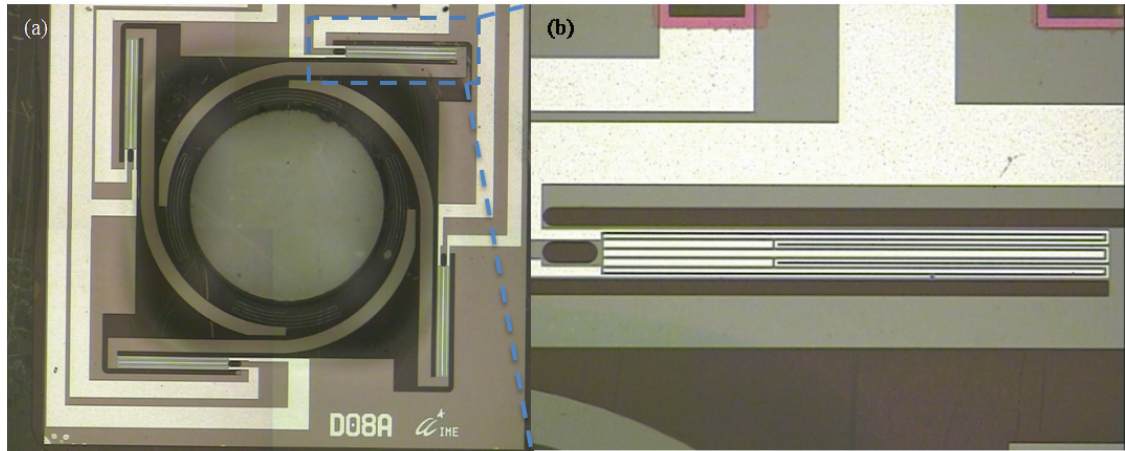


Figure 4.3 (a) A two-axis gimbal-less micromirror with FBAs. (b) A close up view of the Al wires on the straight microstructure of a FBA. (Figure 4.3 (a) redraw from Figure 1 (c) in [90]).

In order to improve the mechanical deflection performance, electrothermal bimorph actuators have continuously evolved from straight actuators [30] to curved actuators [90]. The evolution brings us a significant improvement on the mechanical deflection of the

mirror plate up to 70 %. It should be attributed to the 80 % increase in the length of the actuators of curved actuators. In all of these designs, the mechanical deflection of the mirror plate depends on the diameter of the mirror plate as well as the vertical displacement on the tip of the bending actuator. The mechanical deformation of the bending actuator is mainly dependent on the length of the actuator. Given the same mirror plate size and applied driving voltage, the dominating factor on the mechanical deflection of the mirror plate is the length of the actuator. A longer actuator obviously provides larger mechanical deflection. However, as a matter of fact, the increased length of a longer actuator requires more space in the chip and undoubtedly sacrifices the fill factor of the micromirror. Moreover, since the thermal response time of the actuator is proportional to the square of the actuator length [88], the switch rate of longer actuators significantly decreases. Another drawback of these designs is that with the same actuator but different mirror plate sizes, a micromirror with a small mirror plate always has better performance in mechanical deflection than others with large mirror plates.

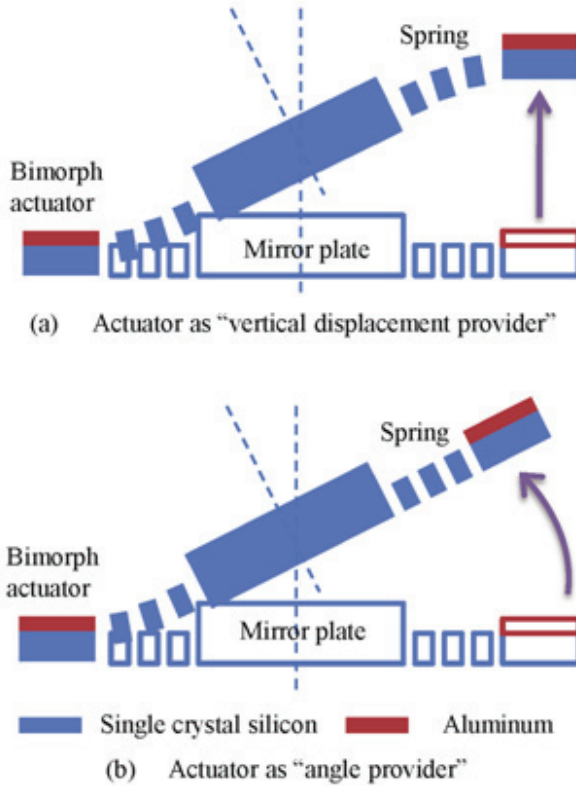


Figure 4.4 Comparison of bimorph bending actuators providing (a). vertical displacement and (b) rotational angle. Solid patterns show a tilting micromirror while hollow patterns show a resting micromirror. (From Figure 2 in [90]).

Therefore we develop a new actuator design which is called FBA, as shown in Fig. 4.3. The design of the FBA can be regarded as a combination of the straight actuator and the curved actuator aforementioned. The FBA consists of a straight bimorph microstructure with an Al electrical circuit on the frontside and SCS as the backbone and a folded curved beam connecting to the mirror plate through a flexural spring. If the FBA is heated, due to the mismatch of CTE between Al ($23.1 \mu\text{m}\cdot\text{m}^{-1}\cdot\text{K}^{-1}$, 25°C) and Si ($2.6 \mu\text{m}\cdot\text{m}^{-1}\cdot\text{K}^{-1}$, 25°C), the straight bimorph microstructure of the FBA bends down while the mirror plate is tilted up by the folded curved beam of the FBA. In addition, the role played by the

FBA is no longer a “vertical displacement provider” as in our previous designs but an “angle provider”. In the new scheme, the angle of mechanical deflection of the mirror plate is only dependent on the length of the actuator and the applied driving voltage but has nothing related with the mirror size. The comparison on the “vertical displacement provider” and the “angle provider” is shown in Fig. 4.4. In Fig. 4.4 (a), a conceptual cross sectional schematic illustrates a mirror plate tilted by a conventional bimorph actuator as a “vertical displacement provider”. Springs are laterally stretched due to the increased distance between the excited actuator and the tilted mirror plate. Moreover, since the bimorph actuator elevates vertically or nearly vertically while the mirror plate is rotated into a certain angle, springs also suffers from the torsion stress due to the angle mismatch between the mirror plate and actuators. The tensile and torsion stresses limit the motion range of the actuator and further the rotational angle of the mirror plate. In the case of a large angle tilting, the issue gets worse. As a solution, in Fig. 4.4 (b), the folded curved beam (not shown in the Fig. 4.4 (b)) works together with the straight bimorph microstructure of the FBA. The distance between the tip of the excited FBA and the mirror plate nearly remains the same so that the stress generated in springs can be reduced. Hence, the FBA, as an “angle provider”, has the same deflection angle as that of the mirror plate.

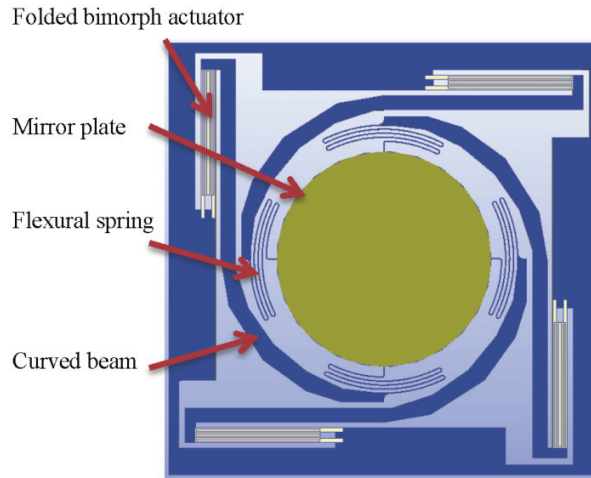


Figure 4.5 Top-view of a 3D model of a two-axis gimbal-less micromirror created by Coventorware. (From Figure 3 in [90]).

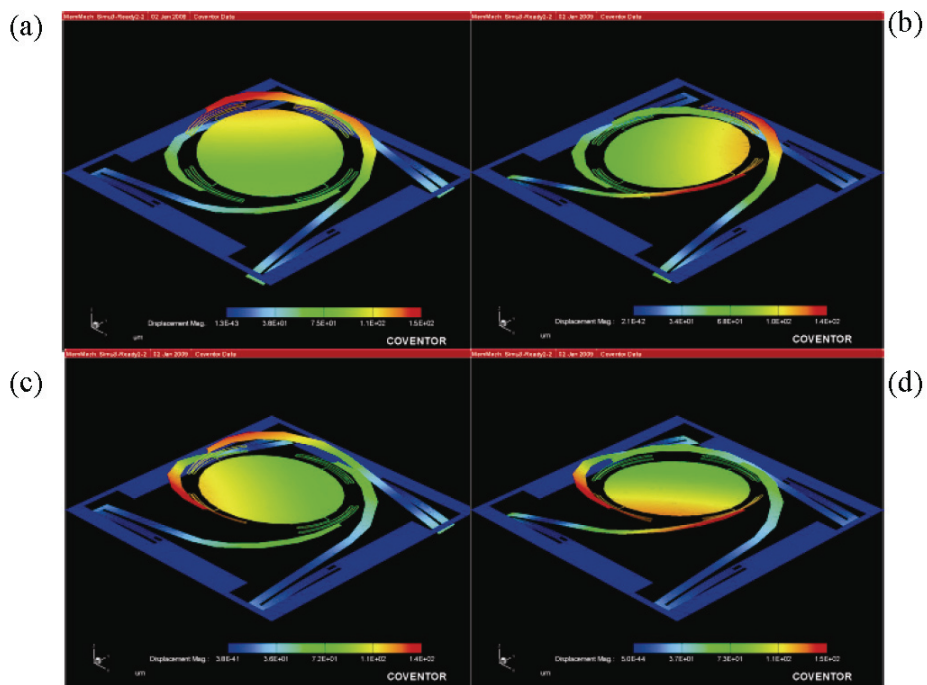


Figure 4.6 3D displays of simulation results of the two-axis micromirror under multichannel sinusoidal waveforms with different phase changes: (a) 0° ; (b) 90° ; (c) 180° ; (d) 270° (From Figure 4 in [90]).

The FEA simulation was conducted by using Coventorware to predict the performance and understand the behavior of the two-axis gimbal-less micromirror under certain temperature loads. Layout files were imported into Coventorware in order to create 3D models of micromirrors, as shown in Fig. 4.5. Variations of geometrical and temperature load parameters were used to understand the effect of different layouts with a variation of springs and actuators. A series of 3D displays of Coventorware simulation results of the two-axis micromirror under multichannel sinusoidal waveforms with different phase changes are shown Fig. 4.6.

4.2 MICROMACHINED ELECTROTHERMAL SCANNERS FABRICATION PROCESSES

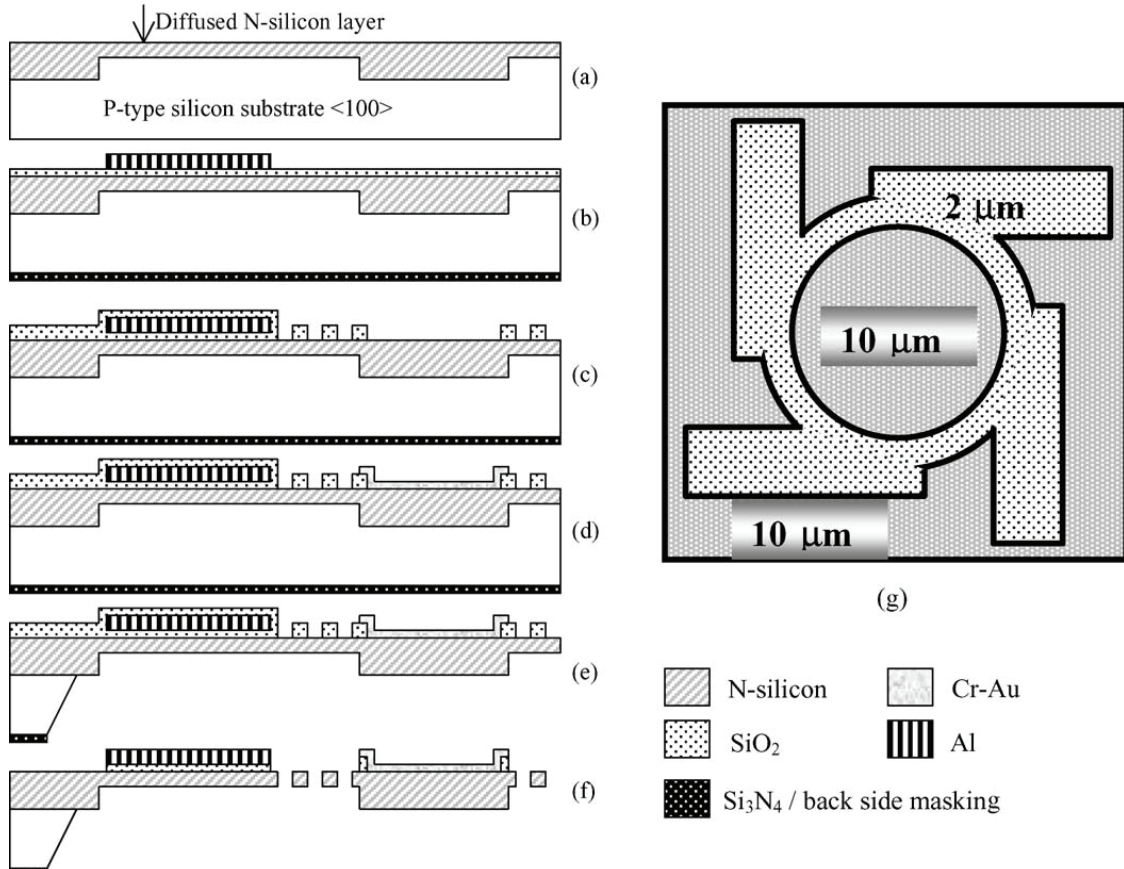


Figure 4.7 (a) Silicon substrate after implantation steps. (b) Substrate after Al patterning (mask #2) and depositing back side masking layers. (c) PETEOS (5000 Å thick) deposition and patterning (mask#3). (d) Thin Cr–Au (150–500Å) deposition and patterning for reflecting surface. (e) Processed wafer after four probes ECE in aqueous KOH. (f) Silicon cut through oxide hard mask and final release of the structure. (g) Plane view representation of cross-section (b), numbers are the n-layer thicknesses. (From Figure 3 in [30]).

Before we proceed to the new SOI fabrication process developed for current MEMS scanners, an overview on previous silicon fabrication process of 3D micromirror for

optical communication network switching applications [30] is given here as a background introduction and comparison. CMOS 6 inches silicon wafer fabrication facility was used for the development. Fabrication process started with prime <1 0 0> p-type 6 inches silicon wafers. Phosphorus implantation and annealing drive-in steps were carried out to form two-step p–n junctions. First phosphorus (n-type of impurity) implantation (for n-silicon layer) was carried out through a masking step (mask #1) for deeper junction and impurity was diffused by high temperature annealing to a depth of 8 μm . Second phosphorus implantation was carried out globally using open frame photoresist masking and impurity was diffused by high temperature annealing to a simulated shallow depth of 2 μm . In the third implantation step, phosphorus was selectively implanted and annealed to prepare n+ silicon ohmic contact in the n-region. In the fourth implantation step, boron was selectively implanted and annealed to prepare p+ silicon contact in the p-region of the substrate. Fig. 4.7 (a) shows the cross-section view of the two-step p–n junction substrate. Thin films, thermal silicon dioxide–LPCVD silicon nitride–PETEOS silicon dioxide–PECVD silicon nitride, which were used as the hard mask during silicon etching in aqueous solution of KOH, were deposited on the back side of the processed silicon substrate. In the following steps, silicon nitride and native oxide layers on the front side of wafer were stripped off before depositing a fresh layer of PETEOS silicon dioxide of 2000 Å thickness to work as electrical isolation layer. Aluminum thin film of 1 μm thickness was deposited on PETEOS oxide layer and etched using second mask (mask #2) lithography. Processed substrate at this stage is shown in Fig. 4.7 (b). Aluminum was used as bimorph material and resistive heater in the actuator, and to form metal electrical current lines and pads. Another PETEOS silicon dioxide of 5000 Å was deposited on the

aluminum, patterned (using mask #3), and etched, shown in Fig. 4.7 (c). This silicon dioxide layer covers and passivates previously patterned aluminum from ambient and was also used as the hard mask in the last step during DRIE for silicon cut to realize the microstructure. In the following deposition and lithographic (mask #4) steps, Cr and Au of 150 and 500 Å thicknesses respectively were deposited and patterned for mirror reflecting surface and for bonding pads as well, shown in Fig. 4.7 (d). Next, an aluminum thin film was deposited for silicon ECE electrical contacts and patterned using open frame lithography to separate n-silicon and p-silicon areas for probing independently. Last lithographic step (mask #5) was carried out on the backside to pattern hard mask layers, thermal silicon dioxide–LPCVD silicon nitride–PETEOS silicon dioxide–PECVD silicon nitride. Now the processed wafer was ready for backside four probes ECE of silicon in aqueous solution of KOH. The etching in KOH was carried out at 75 °C and it took about 15 hours to etch through the wafer and stop at n-silicon layer. During ECE, electrical potential was applied as such that p-silicon was etched, while etching stopped on the n-silicon at the junction. The processed silicon substrate at this stage is shown in Fig. 4.7 (e). Before moving to next steps for releasing devices, processed wafer was diced into small mirror array chips. After dicing, ECE metal was stripped off from the front side, which opened the silicon dioxide hard mask. In the final step, silicon was cut through the silicon dioxide hard mask, which realized the mirror array devices. Cross-section view of the released structure is shown in Fig. 4.7 (f). In the design/process, n-silicon used in the actuator and the springs was 2 μm thick; the edges of thick mirror plate were also kept 2 μm thick for achieving simultaneous release of the structure. This mechanism was proved to be very useful and a high yield of about 80 % could be reached.

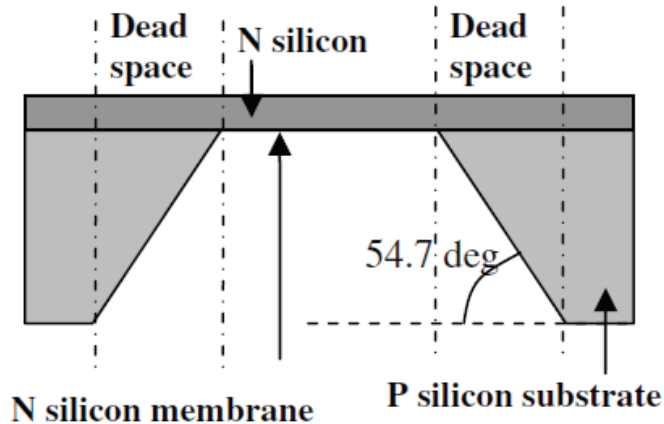


Figure 4.8 Silicon etching in an aqueous KOH. (From Figure 8 in [89]).

As a conclusion, the fabrication process mentioned above was based on a two depths (steps) p–n junction silicon membrane and backside silicon substrate etching in an aqueous solution of KOH. In this fabrication, the potential-dependent electrochemical etch stop on the diffused n-layer from the backside was the most critical process module. A two thicknesses n-silicon layer membrane was realized, which was subsequently selectively etched to form the micromirror components. The chip size was $2.5 \text{ mm} \times 2.5 \text{ mm}$ for a mirror plate size of $400 \mu\text{m}$, and it had a lot of dead space because of anisotropic silicon etching in the aqueous solution of KOH, which was crystallographic orientation dependent. In a $<100>$ oriented silicon substrate etching window opens at 54.7° from the surface.

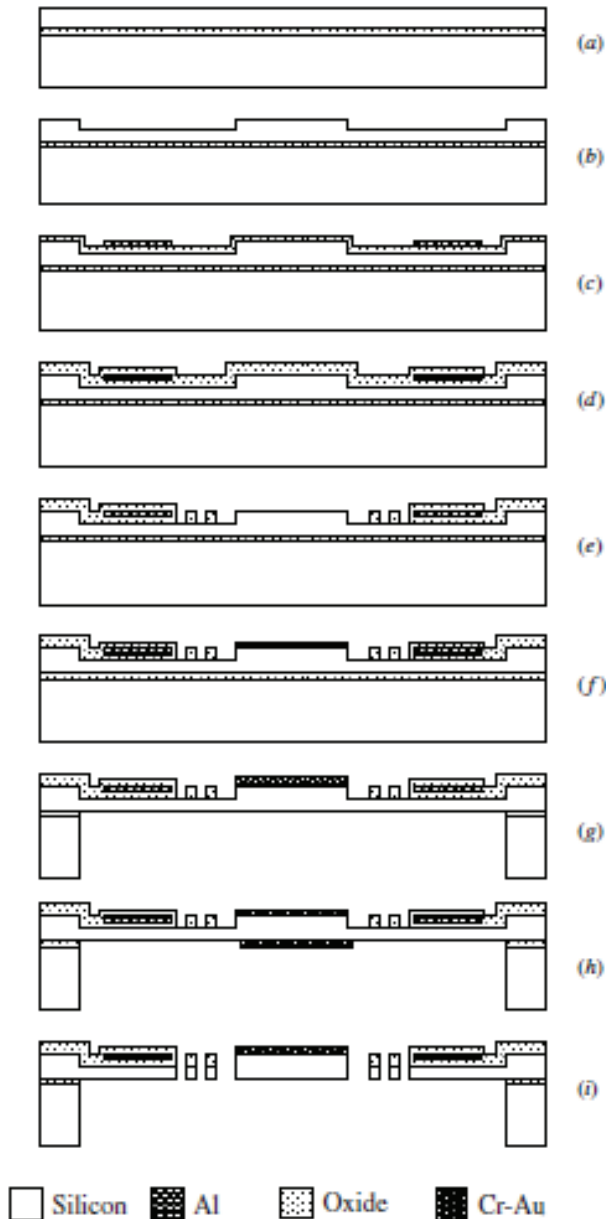


Figure 4.9 SOI thermally actuated micromirror fabrication process flow. (From Figure 9 in [89]).

The new SOI MEMS process, shown in Fig. 4.9, was designed to eliminate the dead space and to reduce the overall size of the micromirror chip. The proposed process is based on the high aspect ratio DRIE process. Most of the steps in the new process are

based on dry etching chemistries, which is good for achieving a higher yield compared to a process with wet process steps.

4.2.1 CMOS-COMPATIBLE PROCESSES

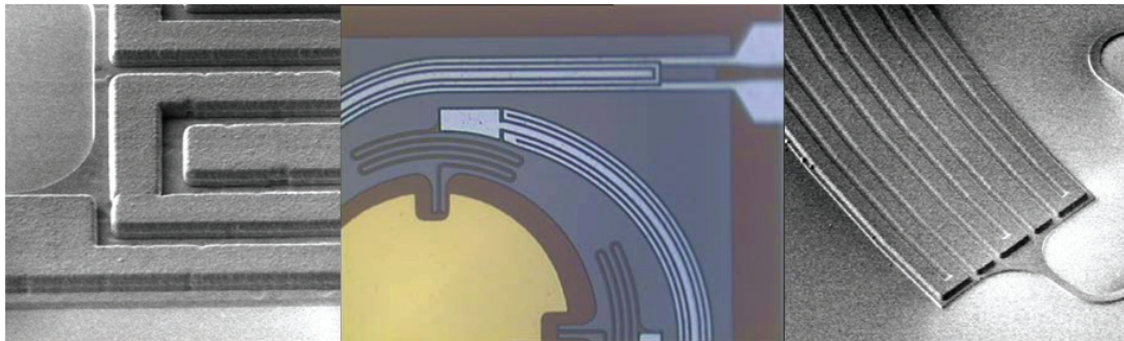


Figure 4.10 Oxide hard mask, mirror metal and Al heaters. (From Figure 10 in [89]).

The process starts with an 8 inch, 4 μm thick device layer and 750 μm thick silicon on an insulator (SOI) p-type substrate as shown in Fig. 4.9 (a). Selective partial etching of the SOI silicon device layer is carried out using the DRIE process to form a two thickness membrane layer as shown in Fig. 4.9 (b). Actuators and flexural springs are then defined in a thinner membrane area, and a mirror is formed in a thicker central area; the process sequence is shown in Fig. 4.9 (c)–(f); these steps are similar to the earlier article [30]. Silicon dioxide is used as the electrical isolation material, Al is used for the heater and bimetal (Fig. 4.10), and silicon is used as the microstructure backbone. All the steps described above are carried out in a CMOS compatible state of the art 8 inch silicon process line clean room.

4.2.2 MEMS PROCESSES

The processed wafers are now transferred for MEMS-specific steps to the MEMS clean room. Cr (50 nm)–Au (100 nm) is then deposited and patterned (shown in Fig. 4.9 (f)) for mirror reflecting surface metal and also for protecting Al pads. Cr–Au is directly deposited on to the silicon mirror plate. Grinding and polishing steps follow next to reduce the substrate thickness to 500 μm ; this is done to reduce the backside DRIE process time. A thin Al metal sacrificial layer is then deposited on the front side to provide a good thermal and electrical contact during the backside DRIE process of silicon. This is important because the charging phenomenon can cause wafer to stick on the chuck, which would break the wafer and also good heat transfer is essential to keep the wafer cool during etching for good results. The backside DRIE process stops on the buried oxide layer, which is later etched by reactive ion etching to realize the silicon membrane of two thicknesses. The structural components were already defined in an oxide hard mask on the front side of the membrane from the earlier CMOS process compatible clean room (Fig. 4.9 (g)). In the next step, Cr–Au (same thickness as the front side) is deposited by evaporation and patterned on the backside of the mirror plate (Fig. 4.9 (h)). The Cr–Au thin films on the backside of the mirror plate are of the same thickness as on the front side; this forms a symmetrical sandwich composite structure for a flatter micromirror. We had proposed this scheme in our earlier article [5.1] and now it is implemented. Patterning is performed using a negative photoresist, which can be electroplated on an Au seed layer. Next, a thin oxide layer of 100 nm is deposited on the backside of the membrane to provide the etch stop surface when the SOI membrane is

etched on the front side to realize microstructure components; this avoids etching attack on the backside of the silicon microstructures.

4.2.3 DEVICE DICING AND RELEASING PROCESSES

At this step we have a processed substrate with SOI device layer silicon membrane windows (Fig. 4.9 (h)). The silicon membrane has thermal actuators and a mirror defined with PECVD oxide and a Cr–Au mirror as hard masks on the front side. On the backside of the membrane there is a thin film of Cr–Au on the mirror plate and a global thin PECVD oxide layer of 100 nm.

4.2.3.1 MECHANICAL DICING WITHOUT PROTECTIVE COATING

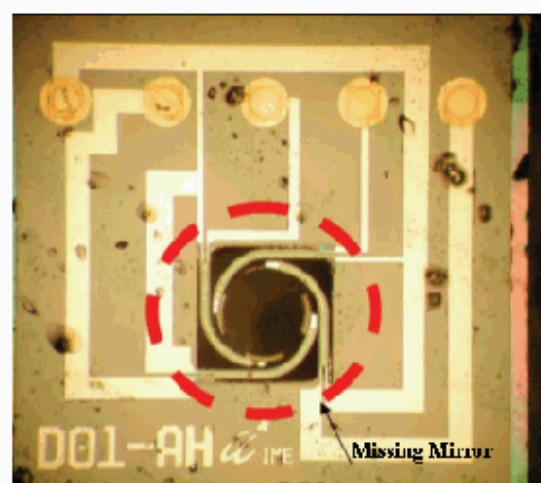


Figure 4.11 Missing mirror plate of a released micromirror after mechanical dicing without protective coating. (From Figure 4 in [91]).

One of the issues is the singulating of the individual mirror devices from a wafer level. As the mirror is highly vulnerable to shock and mechanical pressure, it cannot be diced in its current form using traditional mechanical dicing. Mechanical dicing involves pressure

fluid flow. High-pressure fluid (water) flow that is used as coolant cause the actuator and the silicon spring to break, resulting in dropping of mirrors from the wafer (Fig. 4.11).

4.2.3.2 LASER DICING

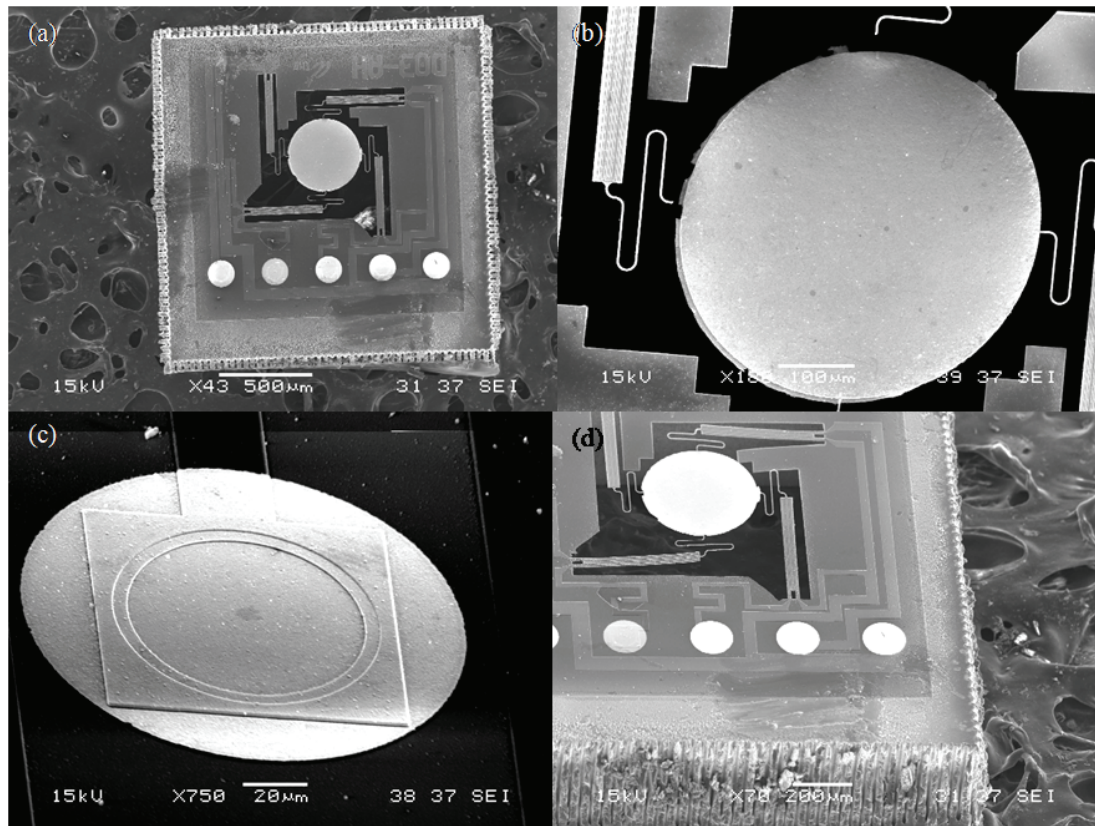


Figure 4.12 (a) A released micromirror attached on an adhesive tape after laser dicing. (b) The micro plate and (c) pads were contaminated by white debris generated by laser dicing. (d) Rough edge of the micromirror.

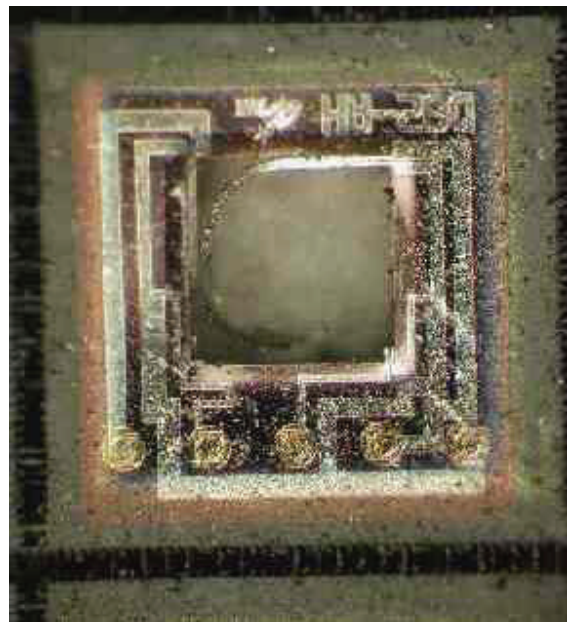


Figure 4.13 Damaged micromirror after laser dicing. (From Figure 6 in [91]).

Laser dicing was explored later but found not to be feasible, due to high heat generated by laser cutting the silicon, debris were produced and the powerful pulsing laser caused burns marks. Along with high vacuum, this resulted in damage. (Fig. 4.12 and 4.13)

4.2.3.3 MECHANICAL DICING WITH PROTECTIVE COATING

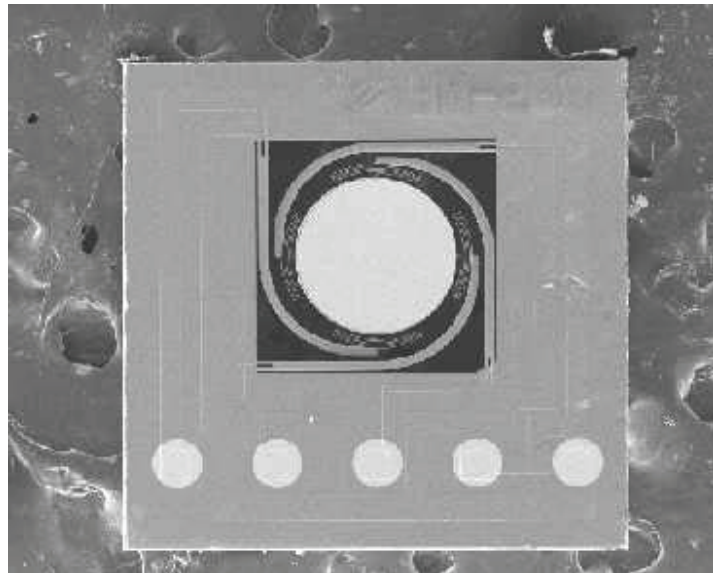


Figure 4.14 A diced micromirror protected by photoresist. (From Figure 7 in [91]).

The mirror device is very fragile when released and any impact either in a wet process or due to handling can break the structure at the springs. Therefore, dicing with the required size such as single mirror chips or multiple mirror arrays were essential before the mirror is freed using the DRIE process of silicon. An OCT optical probe is our target application in this development, where one scanning mirror is used per probe; thus, we diced the processed substrate into single mirror chips of $1.5\text{ mm} \times 1.5\text{ mm}$ sizes. A polymer (SU8 or negative tone photosensitive polymer JSR 151N) coating of about $50\text{ }\mu\text{m}$ thickness was used to protect the thin membrane during dicing. In the absence of a protection layer, all the membranes would be punctured through by a sharp water jet, which is part of the dicing system, to clean the silicon debris generated during dicing. After dicing, mirror chips were peeled off the adhesive tape and passed through polymer stripper wet

chemistry steps. In the case of SU8, we used a SU8 developer, IPA and acetone to clean the chips while JSR 151N had its own stripper solution. No appreciable damage was observed in the polymer removal process. It was noted that a free flow of chips in the wet solutions was more amenable to flow impact, as they could easily turn and twist to soften the force effect and avoid breakage. Now the chips were ready for microstructure release.

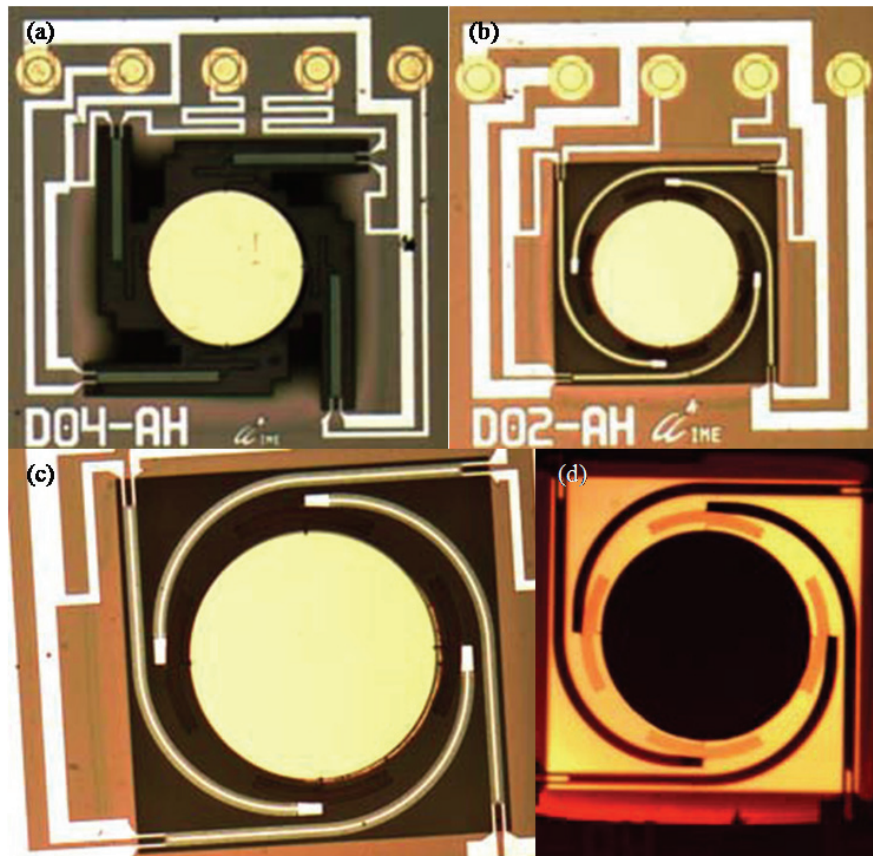


Figure 4.15 Optical images of the released micromirror devices: (a) mirror with a linear actuator, (b) mirror with a curved actuator, (c) mirror view from top, (d) light transmission from back. (Redraw from Figure 11 in [89]).

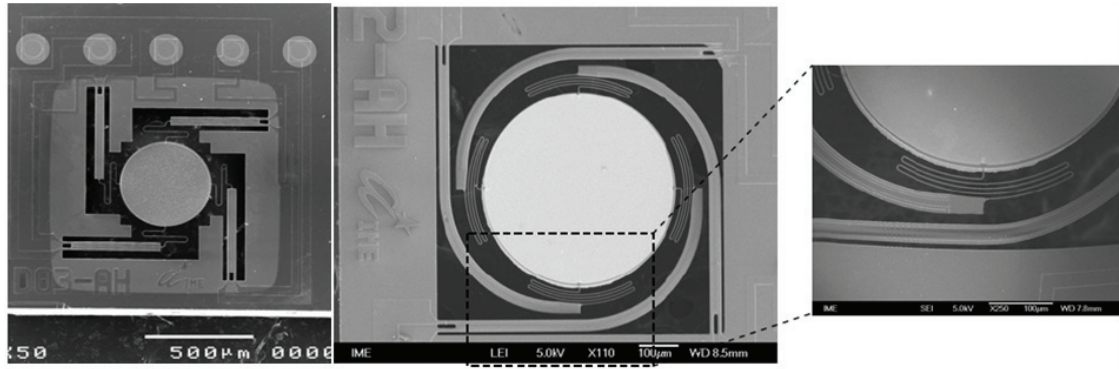


Figure 4.16 SEM micrographs of the realized compact size large tilt angle micromirrors: (a) 400 μm mirror with linear actuators, (b) 500 μm mirror with curvilinear actuators and springs. (Redraw from Figure 12 in [89]).

The mirror chips were placed on to the support wafer and immobilized using adhesive tape, which was compatible with silicon DRIE, oxide layer etching and O_2 plasma clean processes. O_2 plasma clean and 30 s oxide layer etch processes were performed sequentially before the silicon DRIE process was carried out. It took about 1 min to etch through a 2 μm thick silicon membrane to stop at a 100 nm oxide layer. The mirror plate, actuators, and springs could easily be observed through the thin oxide layer membrane. Now in the last step, the mirror chips were flipped over and the thin oxide membrane was etched off using the dry oxide etch process to finally realize the micromirror devices. The realized mirror chips are shown in optical images given in Fig. 5.15 and SEM images given in Fig. 4.16.

4.3 MICROMACHINED ELECTROTHERMAL SCANNERS CHARACTERIZATIONS

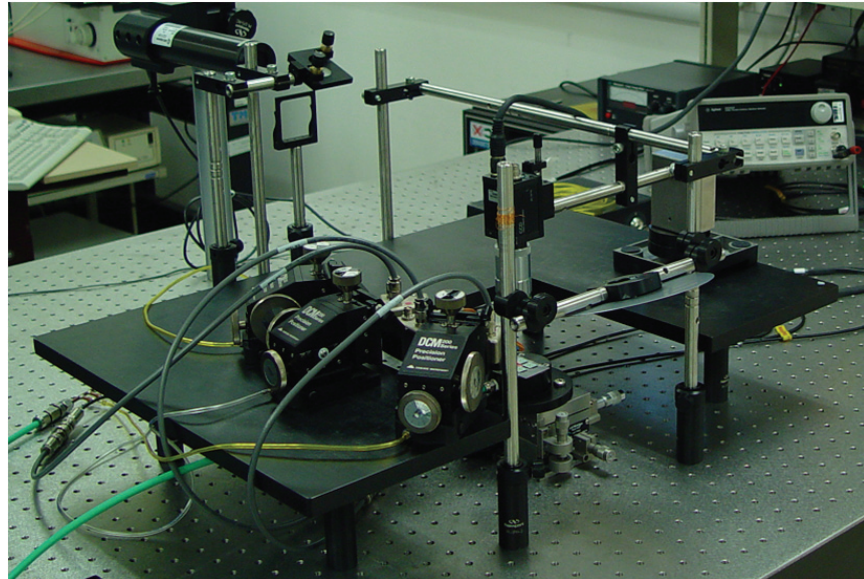


Figure 4.17 Experiment setup for micromirror characterization.

After design and fabrication, a variety of characterizations was important for us to fully understand the behavior and performance of fabricated MEMS scanners. Both steady state and frequency domain testing were conducted by using the experimental setup (Fig. 4.17) consisting of a U shape platform, several micromanipulators equipped with probes for electrical drive signal delivery and pickup, a CCD camera with a high NA objective lens connected to a monitor and a collimated He-Ne laser source and various optical components for laser light projection as well as a vacuum pump (not shown in Fig. 4.17) for micromanipulators fixation.

This section mainly describes detailed characterization information of two kinds of developed electrothermal MEMS scanners, including steady state and frequency informations.

4.3.1 TWO-AXIS GIMBAL-LESS ELECTROTHERMAL SCANNERS BASED ON CURVED ACTUATORS

4.3.1.1 STEADY STATE PERFORMANCE (DC TRANSFER CHARACTERISTICS)

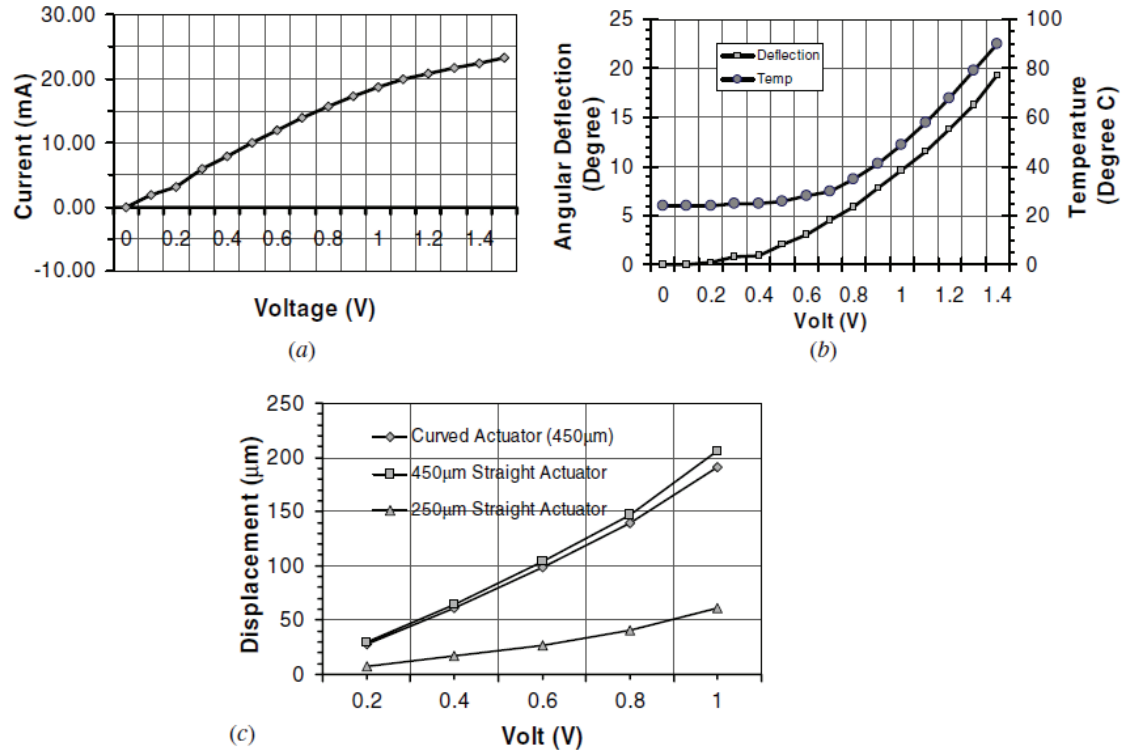


Figure 4.18 Test results of micromirror chips fabricated using $1.5\ \mu\text{m}$ SOI substrates.

A novel SOI integration process for 3D scanning micromirror devices was successfully developed as demonstrated. A test chip approach was used where structural dimensions were varied for the optimization purpose. SOI substrates of silicon device layer thicknesses $1.5\ \mu\text{m}$, $4\ \mu\text{m}$ and $10\ \mu\text{m}$ were used. The micromirror devices were realized and tested out of $1.5\ \mu\text{m}$ and $4\ \mu\text{m}$ substrates as a $10\ \mu\text{m}$ SOI substrate could not be processed due to litho complexities. In the case of $1.5\ \mu\text{m}$ substrates, mirror, actuators and springs, all had $1.5\ \mu\text{m}$ thickness whereas in the case of $4\ \mu\text{m}$ substrates a two

thickness membrane approach was used to have actuators and springs of about 2 μm thickness and mirror plate of 4 μm thickness.

A maximum angular tilt of 17° was achieved with a 1.5 μm thick SOI device layer; the results given in Fig. 5.18 represent this set of devices. As can be seen in Fig. 4.18 (a), the applied voltage was very low, less than 2 V, and the thermal power was always less than 50 mW. Experimental results for angular deflection as a function of voltage and temperature are shown in Fig. 4.18 (b). These results were verified with a theoretical model and were found to have a close match. In Fig. 4.18 (c), the displacement (bending) is plotted against the applied voltage for three different actuator types. The length of the actuator has a significant impact on the total bending; however, curved and linear actuators of the same lengths provide almost the same displacement (bending) irrespective of their shape. This outcome was important to design curved actuators and save the space on the micromirror chip. As can be observed from the testing results (Fig. 4.18(a) and (b)) at 1.6 V, a current of 23 mA was flowing through the actuator, which loaded the actuator with 90 °C temperature and provided a tilt angle of close to 17°. The maximum power at this data point is 36.8 mW. The mirror orientation (displacement) is the direct measurement, which is then used to calculate the angular deflection or tilt angle. The maximum angular tilt obtained from the mirror designs with the same structural geometry as an original 2.5 mm × 2.5 mm chip was 11°, matching our previous results [89].

4.3.1.2 RADIUS OF CURVATURE

The flatness of the micromirror plate is another critical parameter for OCT imaging, as it affects the depth of focus. Initially, with 1.5 μm SOI substrates, a radius of curvature of

about 5 mm was obtained. This low radius of curvature was due to a thin oxide layer in between the Cr–Au and the silicon mirror plate. Cr was also a stress contributing thin film. In the modified process with a 4 μm device layer SOI substrate, Cr–Au was directly deposited on the silicon mirror plate, which was 4 μm thick versus 1.5 μm of the previous case. Another modification was Cr–Au deposition on both sides to balance the residual stress due to metals. These modifications significantly improved the radius of curvature to close to 50 mm, which was good enough for OCT imaging; however, it was still quite low indicating that sandwich composite stress balancing did not work completely and would need further research.

The experimental studies were planned and carried out to understand the curvature phenomena in our mirror plate structure. In the two studies, where a sample had Cr–Au only on the front side and another sample had Cr–Au on the both sides, no appreciable difference in the curvature of the mirror plate was observed. In the next experiment, Au was etched off on the first sample and still the curvature was almost the same. Subsequently, when Cr was also etched off on this sample, the radius of curvature dramatically increased from a few tens of mm to more than 5 m. With this study, we concluded that Cr on the front side of the mirror plate was contributing to most of the curvature of the mirror plate. Cr–Au on the front side was sputter deposited while Cr–Au on the backside was evaporation deposited and as a result stress was not balanced. Sputtered deposited Cr on the front side was identified as the thin film, which was responsible for most of the curvature of the mirror plate. In future work, our aim will be to sputter deposit Cr on the backside of the mirror plate and improve the curvature further.

4.3.1.3 FREQUENCY RESPONSE AND 2D SCANNING PATTERNS

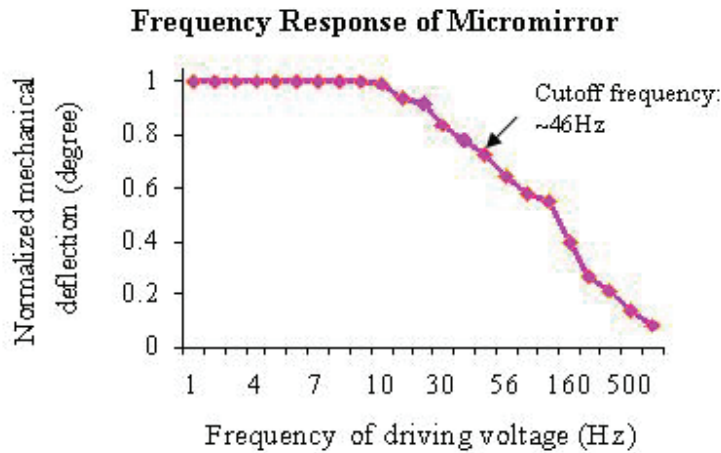


Figure 4.19 Frequency response of the micromirror with a unipolar 1.2 V peak-to-peak sinusoidal signal for full range swing. (From Figure 4 in [34]).

In order to measure the frequency response, a unipolar 1.2 V peak-to-peak sinusoidal signal was applied to one bimorph actuator of the micromirror. The -3dB cut-off frequency was obtained to be 46 Hz as the voltage frequency was increased from 1 to 500 Hz (Fig. 4.18). The corresponding thermal response time was 7.6 ms. This operation frequency is well above the required frequency of about 20 Hz for our optical probe.

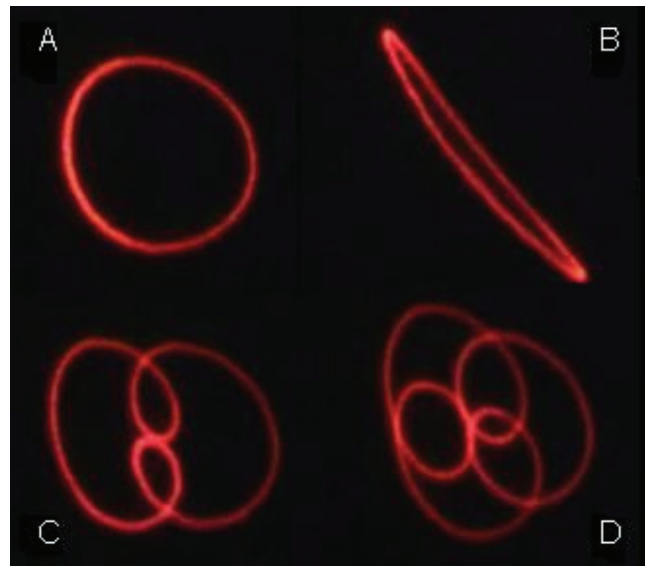


Figure 4.20 (A)–(D) Lissajous patterns scanned by the micromirror. (From Figure 5 in [34]).

Laser patterns shown in Fig. 4.19 were obtained by switching two adjacent thermal actuators in one quarter of the operable space. A Labview program was used to write loop structure patterns using an applied voltage as x – y points in a 2D space. The repetition rate for the loops was 10 Hz.

4.3.1.4 REPEATABILITY AND RELIABILITY MEASUREMENTS

The scan repeatability of the micromirror devices was studied and reported earlier [30]. A high tilt angle, manageable curvature, and demonstrated scan repeatability had qualified the developed 3D thermally actuated single crystal silicon micromirror for use in a miniature silicon optical bench (SiOB) optical probe for OCT bioimaging applications.

4.3.2 TWO-AXIS GIMBAL-LESS ELECTROTHERMAL SCANNERS BASED ON FOLDED ACTUATORS

4.3.2.1 STEADY STATE PERFORMANCE (DC TRANSFER CHARACTERISTICS)

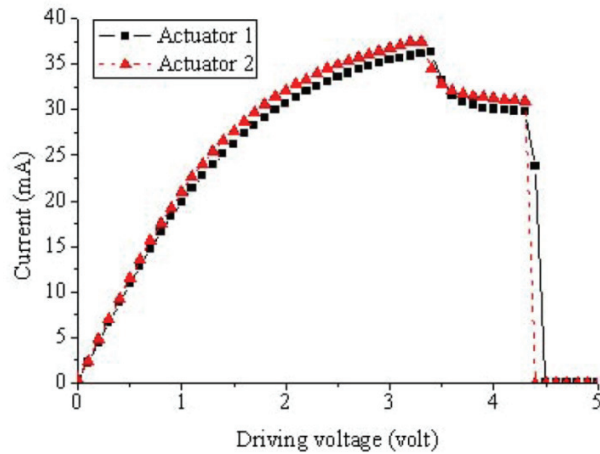


Figure 4.21 Measured voltage-current relationship of actuators. (From Figure 6 in [90]).

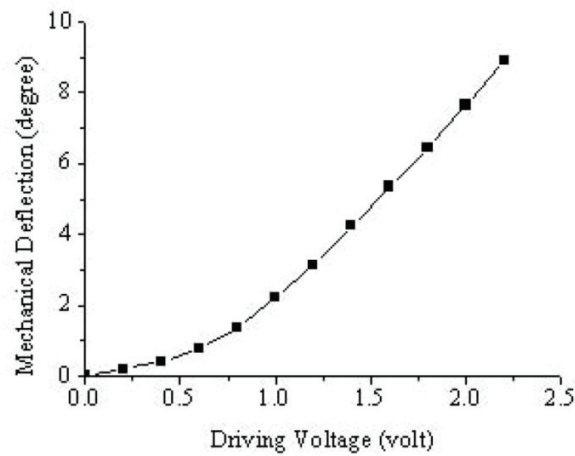


Figure 4.22 Measured voltage-mechanical deflection relationship of the two-axis micromirror. (From Figure 7 in [90]).

Characterization of the two-axis micromirror, such as voltage-current relationship of an actuator, the voltage-mechanical deflection relationship and the curvature of the mirror plate, was carried out. A precision semiconductor parameter analyzer (4156C, Agilent Technologies, USA) was used to measure voltage-current relationship of the actuator. The result is shown in Fig. 4.21. Here we conducted a destructive measure that the analyzer delivered a driving voltage to the target actuator of a released micromirror device as high as possible to find out the electrical tolerance of the Al electrical circuit on the actuator. In Fig. 4.22, the actuator has shown the capability of sustaining slightly more than 3 V driving voltage. After the driving voltage reached the peak value around 3.2 V, the current suddenly decreased at first and then gradually decreased to a constant value about 30 mA. When the driving voltage was more than the other critical value, usually about 4.3 V, the current slightly increased and shortly fell down to zero that indicates the failure of the actuator under testing. If the applied driving voltage did not exceed the second critical value as mentioned above, there was no failure of the actuator observed and such a test was repeatable. But usually applying driving voltage between the two critical values definitely caused the plastic deformation of the actuator rather than elastic deformation as expected. In this case, the failure of the actuator was not a pure mechanical failure but a mechanical induced electrical failure. The phenomenon could be attributed to development of microcracks in the 1 μm Al electrical circuit during the mechanical deformation of the actuator. When the development of large number of microcracks was beyond a threshold, the current intensity in the connecting part of the Al electrical circuit exceeded the maximum sustainable current of Al so that Al electrical

circuit was broken down. In Fig. 4.22 a maximum measured mechanical deflection of $\sim 9^\circ$ was obtained at an operation voltage of ~ 2.2 V.

4.3.2.2 RADIUS OF CURVATURE

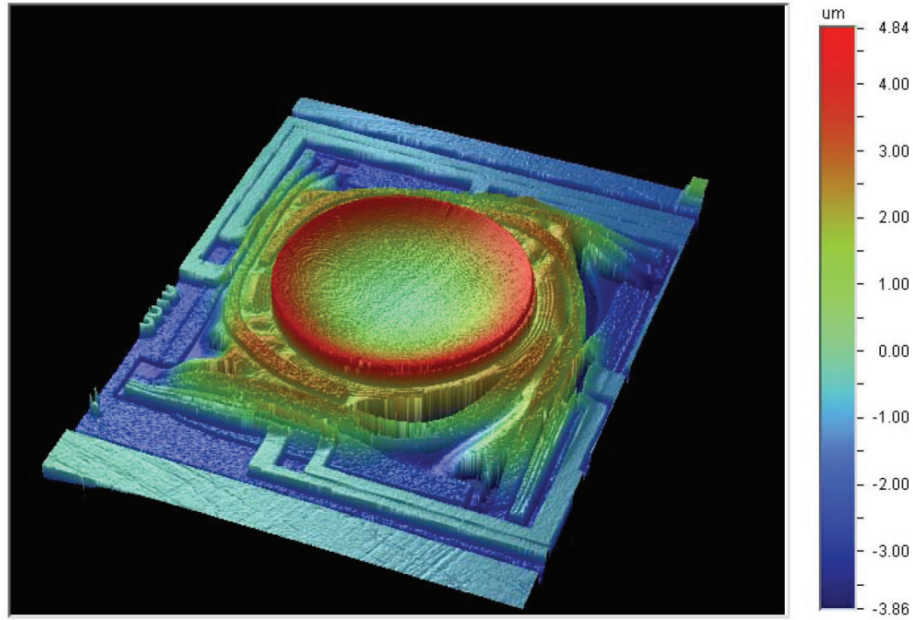


Figure 4.23 3D display of the surface profile of the two-axis micromirror. (From Figure 8 in [90]).

The radius of curvature of the mirror plate was measured to be ~ 45 mm. An optical surface profiler (Wyko DMEMS NT 3300, Veeco Instruments Inc., USA) was used for this test and the 3D result is shown in Fig. 4.23. With thinner Cr / Au layers, the surface flatness of the current micromirror is almost as good as the ~ 50 mm radius of curvature of double sides coated micromirrors which obviously did not reach the goal of the stress balancing. However, the radius of curvature is still quite low and further research for smaller mirror curvature would be required.

4.3.2.3 FREQUENCY RESPONSE

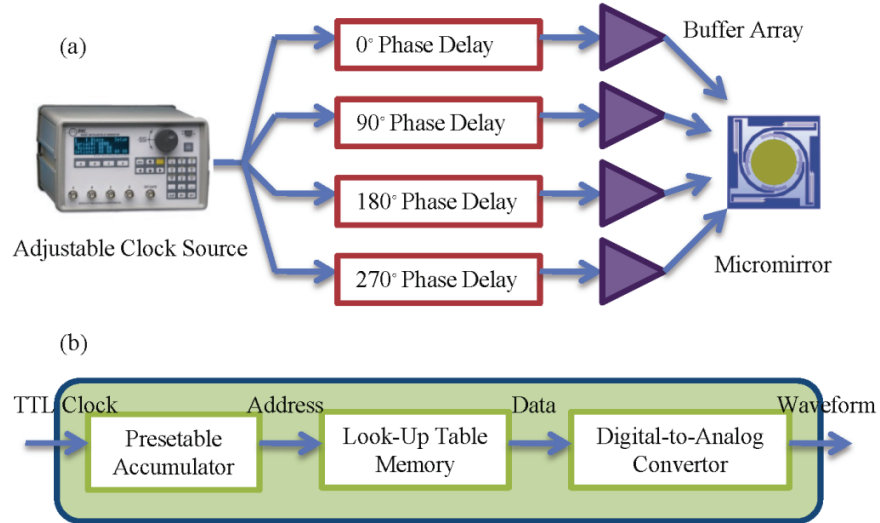


Figure 4.24 (a) Schematic diagram of the micromirror driver circuit for multichannel arbitrary waveform generation; (b) details in single channel. (From Figure 9 in [90]).

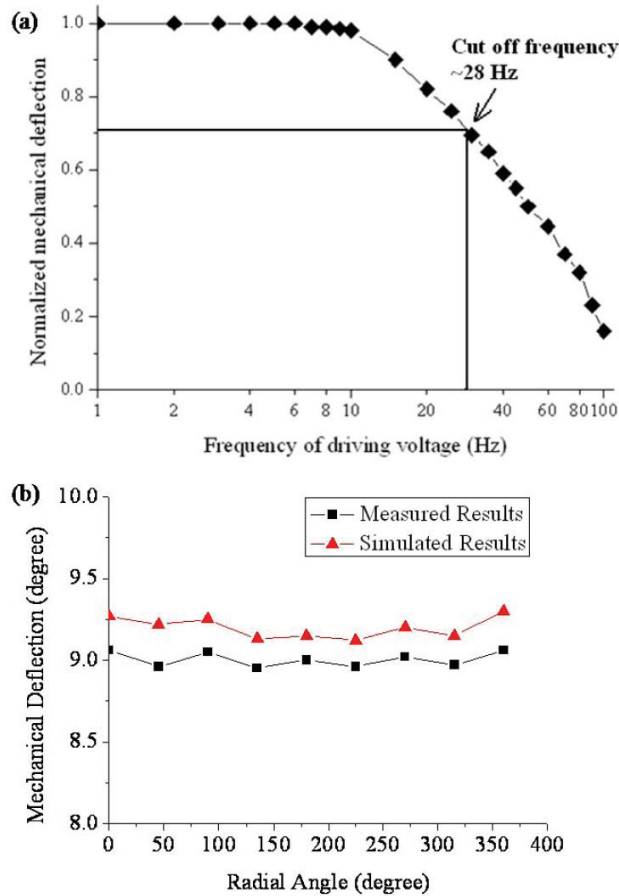


Figure 4.25 (a) Frequency response of the two-axis micromirror under four channels sine wave drive signals for full range swing; (b) measured and simulated angular fluctuation of mechanical deflection of the micromirror to all direction. (From Figure 10 in [90]).

Circumferential beam steering which is the main application of the two-axis micromirror requires multichannel unipolar sinusoidal waveforms with 90° phase difference between each channel to be delivered to four actuators of the micromirror simultaneously. A DDS based micromirror drive circuit utilizing digital phase shifting method was developed to generate multichannel sinusoidal waveforms with certain phase difference. The

schematics of the experimental system and implementation details in single signal generation channel of the driver circuit are shown in Fig. 4.24 (a) and (b), respectively. The frequency of sinusoidal waves generated by all four channels was determined by the frequency of TTL clock from the adjustable clock source. A current buffer array was used to provide sufficient current to the micromirror. The frequency response measurement of the two-axis micromirror was achieved by operating the micromirror by sweeping the frequency of the drive signals from 1 Hz to 100 Hz. The mechanical deflection of the micromirror was measured as a function of the frequency of the drive signals. At the same time the signal amplitude was kept as a constant value. The measurement result was shown in Fig. 4.25 (a), which indicates that the measured -3 dB cut off frequency of the micromirror is about 28 Hz. The corresponding thermal response time was about 12.5 ms. Fig. 4.25 (b) shows the measured and simulated angular fluctuation of mechanical deflection of the micromirror. It proved that the micromirror can provide a uniform mechanical deflection up to $\sim 9^\circ$ with multichannel drive voltages of less than 2.3 V to any angle in full 360° circumference.

4.4 SUMMARY OF SCANNERS PERFORMANCE

A micromachined electrothermal scanner for integrating in a miniature optical probe for OCT bioimaging applications such as optical biopsy for tissue structural analysis has been developed. Theoretical, Coventorware FEA solid model simulations and design were carried out to optimize device parameters. The curved beam actuators and flexural springs were designed and developed to eliminate dead space on the chip; the curved shape increased the length of the actuators while reducing the overall chip size. A novel single SOI wafer process was designed and developed utilizing a high aspect ratio silicon

DRIE process, which was essential to reduce the dead space on the chip. Tilt angle and curvature characterization were performed to establish the suitability of the device for miniature probe integration. Theoretically predicted results match quite closely with the measured results. The measured curvature was about 50 mm, which was acceptable to our current application. The device has advanced to integrate with a silicon optical bench miniature probe.

The first prototype of two-axis gimbal-less micromirror integrated with novel folded bimorph electrothermal actuators optimized for large-angle circumferential scanning applications has been demonstrated. The micromirrors were fabricated by the modified SOI MEMS process. FBAs not only provide large uniform mechanical deflection angle up to 9° in all directions but also help maintain the high fill factor and small outline of the micromirror. FEA simulations and characterizations on devices are performed. The micromirror has advanced to such a level that it can be further improved for larger angular deflection and smaller mirror plate curvature, which makes it more suitable for endoscopic OCT imaging.

CHAPTER 5

SiOB ASSEMBLY: DESIGN, FABRICATION PROCESS, ASSEMBLY AND CHARACTERIZATION

SiOB technology has become a critical solution for aligning micro optical components on silicon substrates in high precision. It has been widely used in a variety of applications in micro optics packaging, such as optical transmitters [92] / receivers [93] / transceivers [94], filters [95, 96], switches [97], attenuators [98] and splitters [99], even more complex micro optical systems, such as micromachined tunable lasers [100, 101], Mach-Zehnder interferometers [102] , Fourier transform spectrometers [103] as well as miniaturized catheters for EOCT imaging [104, 105]. The main technical challenge to realize miniaturized MEMS based EOCT catheters lies in the high precision assembly of a MEMS scanner and micro optics components as well as the delivery of external electrical drive signals to the MEMS scanner. In this study two kinds of SiOB assembly were developed sequentially. The design, fabrication process, assembly and characterization of both two designs are shown in the following sections.

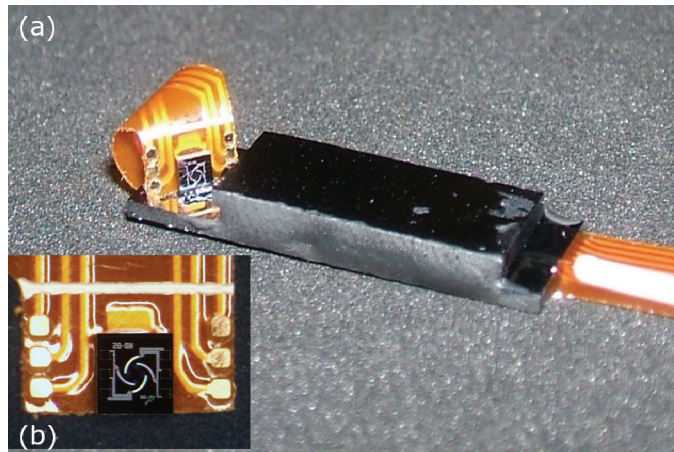


Figure 5.1 An early stage prototype of SiOB.

Fig. 5.1 shows an early stage prototype of SiOB prior to the two SiOB designs described as follows. The six pads aligned on two sides of the MEMS scanner integrated, which is differently from the current MEMS scanner design. The MEMS scanner was first glued on a flexure PCB and tiny gold wires were bonded between the pads on the MEMS scanner and other pads on the flexure PCB. Then the whole assembly was fixed on the lower substrate and the electrical connection to the external drive source was created by the Flexure PCB. However, it was found that it is impossible for this design to meet the requirement for EOCT application due to its large outer dimension both in SiOB and in flexure PCB. Therefore future improvements were made and two new SiOB designs have been developed sequentially in order to solve technical challenges: small dimension, electrical connection and optical alignment.

5.1 TRADITIONAL SiOB

5.1.1 DESIGN

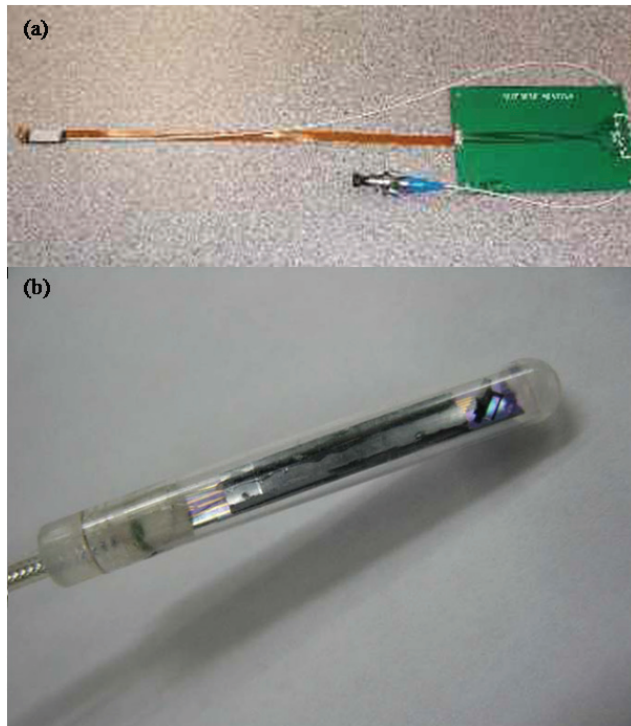


Figure 5.2 (a) Assembled traditional SiOB with flexure PCB interface. (b) Packaged traditional SiOB assembly ready for OCT imaging test. (Redraw from Figure 16 in [91] and Figure 10 in [106], respectively).

The traditional SiOB design [34, 104] was developed for a low cost assembly and packaging solution for the MEMS based EOCT catheter and consisted of two silicon substrates vertically stacked for different purposes. A trench was opened by KOH anisotropic wet etching on the top surface of the lower silicon substrate for embrace a two-axis gimbal-less electrothermal micromirror. The trench was rotated by 45° to the optical axis, e.g. the axis of the SiOB. Five Cr/Au metal lines were deposited on the low

substrate to create electrical contact between the micromirror and the external drive circuit with assistance of micro soldering technology [91]. The function of the other silicon substrate, the upper substrate, is to elevate a customized GRIN lens assembled with a SMF and a glass spacer to the appropriate situation so that the optical axis of the GRIN lens assembly can be precisely aligned with the center of the mirror plate of the micromirror. Therefore the thickness of the upper silicon substrate as well as the depth of the slot opened on the upper silicon substrate for the GRIN lens assembly and the depth of the trench on the lower silicon substrate for the micromirror have been carefully considered.

5.1.2 FABRICATION PROCESS

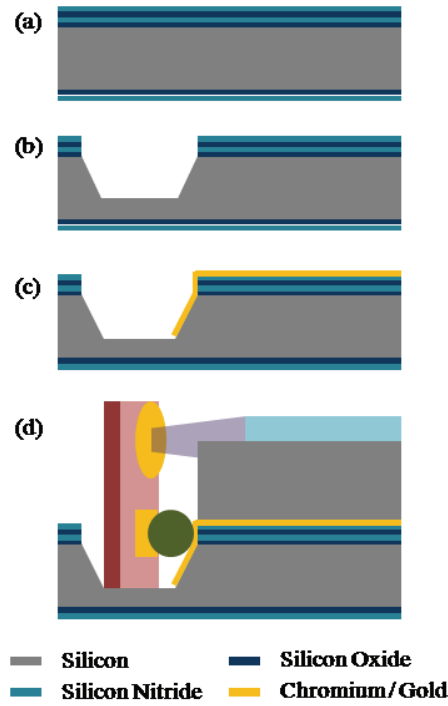


Figure 5.3 Fabrication process: (a) silicon oxide and silicon nitride deposition for the hard mask; (b) KOH wet etching for the trench; (c) chromium/gold deposition, photoresist electroplating on the slope and chromium/gold wet etching for electrical wires. (d) Side view of traditional SiOB assembly. (Redraw from Figure 6 in [104]).

The fabrication process of the lower substrates of the SiOB is shown step by step in Fig. 5.3 (a)-(c). The fabrication was started with an 8 inches silicon wafer. First of all, 300 Å thermal silicon oxide, as well as 1500 Å LPCVD silicon nitride, was grown by SEMCO furnace on the both sides of the wafer. Sequentially, 2000 Å PECVD silicon oxide and 2000 Å silicon nitride were also deposited on the both sides of the wafer by Novellus

PECVD and AMAT, respectively. As is known to all, silicon oxide layer was used to buffer the stress between the silicon substrate and the silicon nitride layer above. After lithography was done, a series of layer coated before were etched by Plasma Therm from the frontside of the wafer in order to form the hard mask for upcoming anisotropic KOH silicon wet etching. Then KOH wet etching was done in multi steps for precisely etching 361 μm in depth. After that 500 Å chromium as adhesive layer for 5000 Å gold was sputtered by Blazers. Negative photoresist (Eagle 2100 ED) was uniformly coated on the trench by electroplating and the pattern of electrical lines was formed by lithography. After exposure in UV and development, wet etching of chromium and gold was used to finally form the electrical wires connecting the micromirror and the external driver on the lower substrate of SiOB.

5.1.3 ASSEMBLY

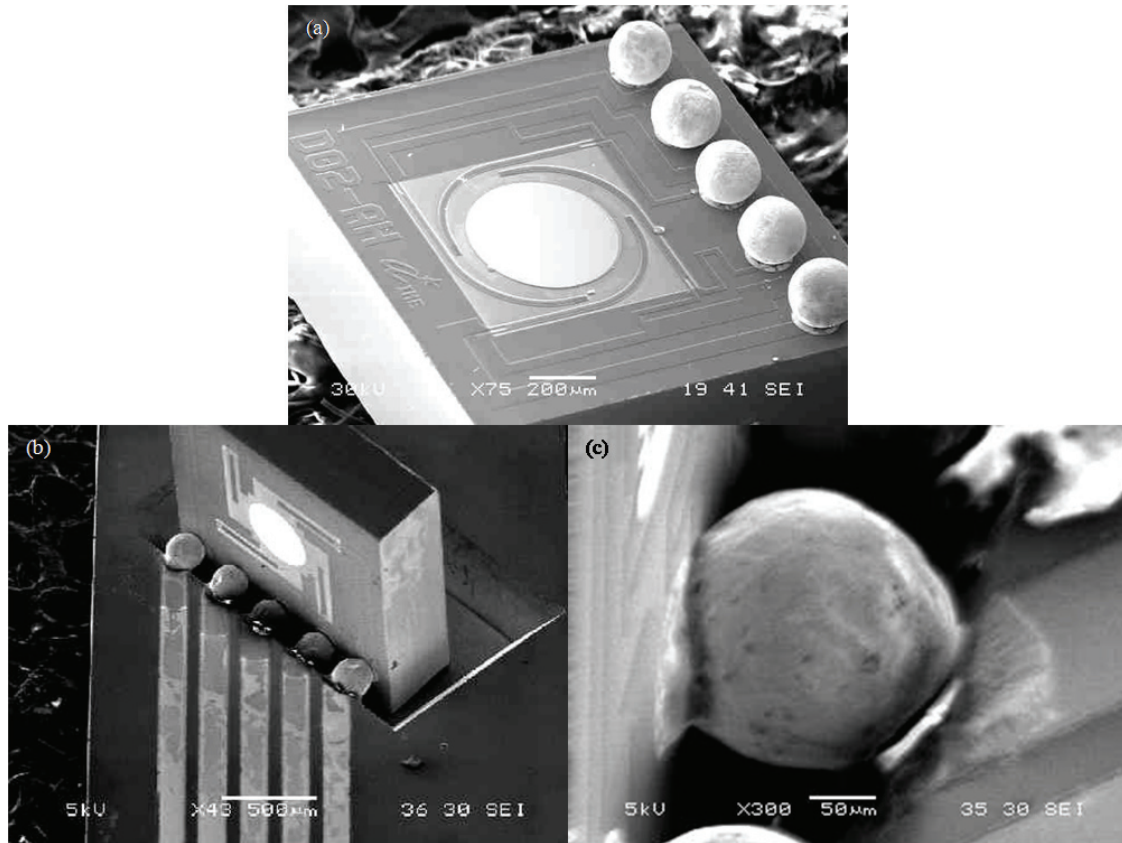


Figure 5.4 (a) Micromirror attached by micro solder balls. (b) Assembly of the micromirror to the lower substrate of the SiOB by two steps micro soldering technology. (b) Interconnection between the micromirror and the chromium/gold electrical wires on the slope of the trench. (Note: different dummy micromirrors were used for assembly testing, so (a) and (b) show different micromirrors used.) (Redraw from Figure 8, 12 and 13 in [91]).

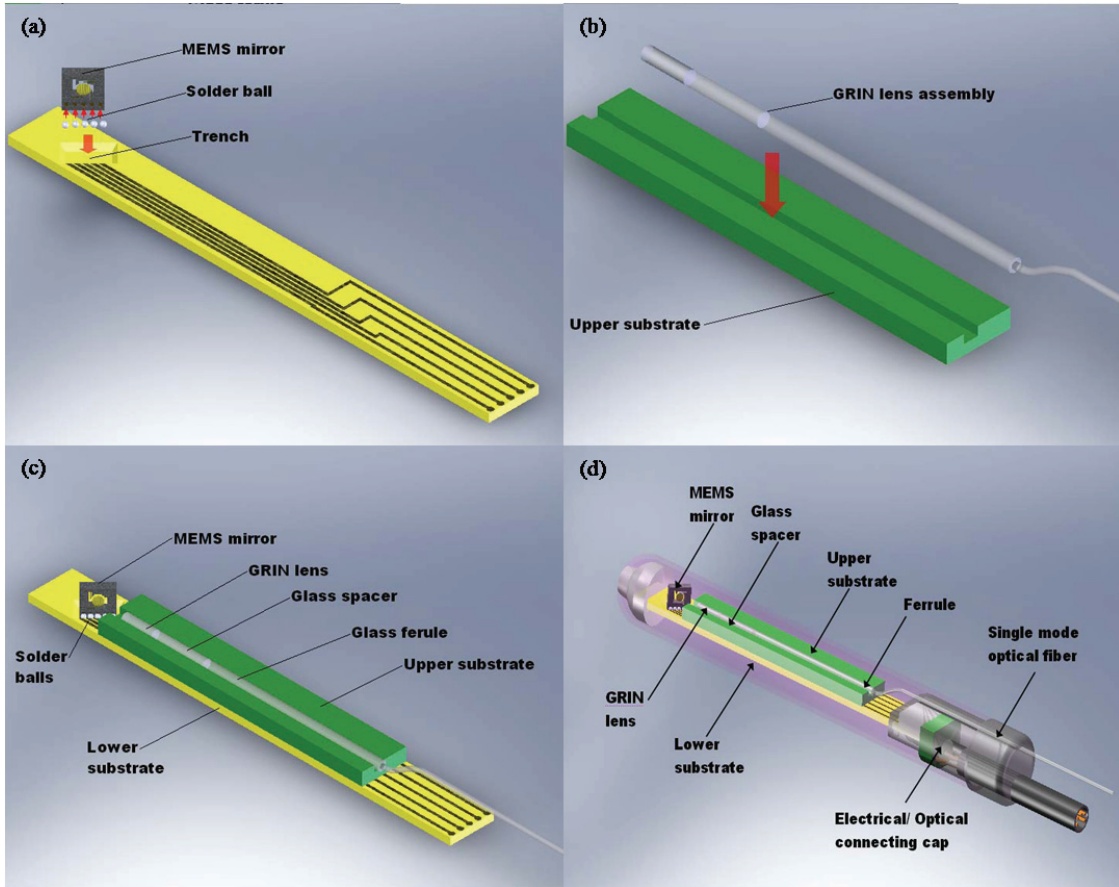


Figure 5.5 (a) Placement of the micromirror onto the lower substrate with the micro solder balls. (b) Placement of the GRIN lens assembly onto the upper substrate. (c) Placement of the upper substrate onto the lower substrate. (d) Full assembly and plastic packaging of the MEMS based endoscopic OCT catheter. (Redraw from Figure 1, 7, 8 and 9 in [105]).

The work flow of traditional SiOB assembly is briefly introduced and listed as follows and its details can be found in our previous publication [91]:

- (1) Pickup and attach five lead free (SnAgCu) micro solder balls with the diameter of 200 μm onto the pads with the diameter of 150 μm of the micromirror by using a eutectic bonder (SEC eutectic die bonder).

- (2) Fluxless process was carried out. The micromirror attached with five micro solder balls was heated to 280 °C in a nitrogen atmosphere. Hence micro solder balls were wet with the under bump metallization (UBM) pads.
- (3) The micromirror with five micro solder balls was manually inserted into the trench on the lower substrate in a nitrogen environment at a reflow temperature of 290 °C which caused micro solder balls to wet with the Cr/Au circuits on the lower substrate, hence establishing the electrical connection.
- (4) The upper substrate carrying the GRIN lens assembly was placed onto the lower substrate and self-aligned with assistance of several position marks made during the fabrication.

5.1.4 CHARACTERIZATION

5.1.4.1 RELIABILITY TEST OF MICRO SOLDER BALLS

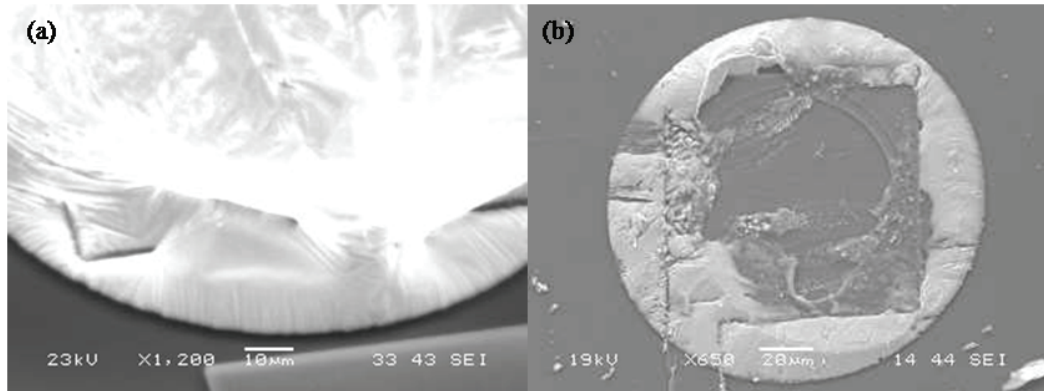


Figure 5.6 (a) Interconnection between a pad and a micro solder ball. (b) Broken pad after shear test. (Redraw from Figure 10 and 11 in [91]).

Reliability test on shear stress was conducted to determine the strength of the interconnectivity bonding between the micro solder ball and the micromirror pad.

Experimental analysis was usually based on visual evaluation and SEM to confirm the presence of the micro solder ball on the mirror pad. The conditions of the shear test were:

- (1) Pad size on micromirror : 150 μm
- (2) Micro solder ball diameter : 200 μm
- (3) Shearing height : 40 μm

The shear test results yielded ball strength of 44.5 gm on average. Fig. 5.6 shows the mirror pad after the shear test. Table 5.1 shows the shear test results.

Table 5.1 Shear test results (Redraw from Table. 2 in [91])

| Sample | Shear strength (gm) |
|---------|---------------------|
| 1 | 40.1 |
| 2 | 32.2 |
| 3 | 56.7 |
| 4 | 36.7 |
| 5 | 42.4 |
| 6 | 52.3 |
| 7 | 37.1 |
| 8 | 41.7 |
| 9 | 53.4 |
| 10 | 52.6 |
| Average | 44.5 |

5.1.4.2 OPTICAL TEST OF ASSEMBLED SiOB

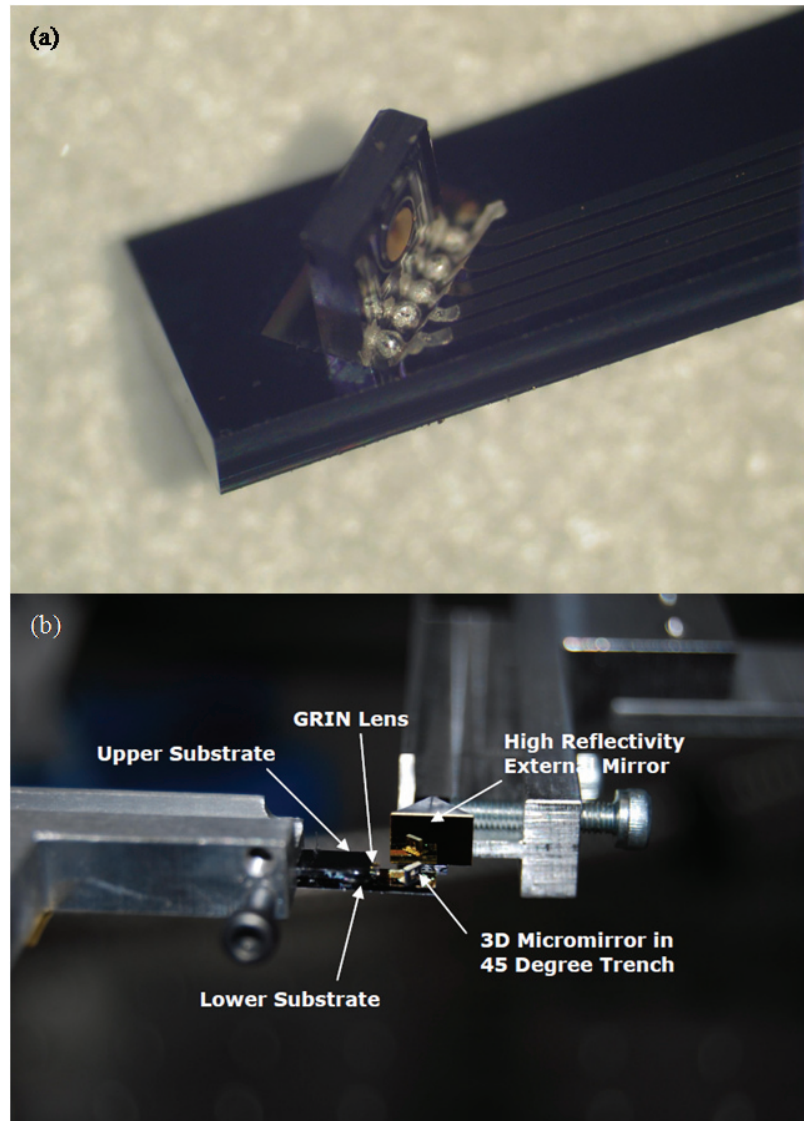


Figure 5.7 (a) Close up view of an assembled SiOB. (b) Experimental setup for optical characterization.

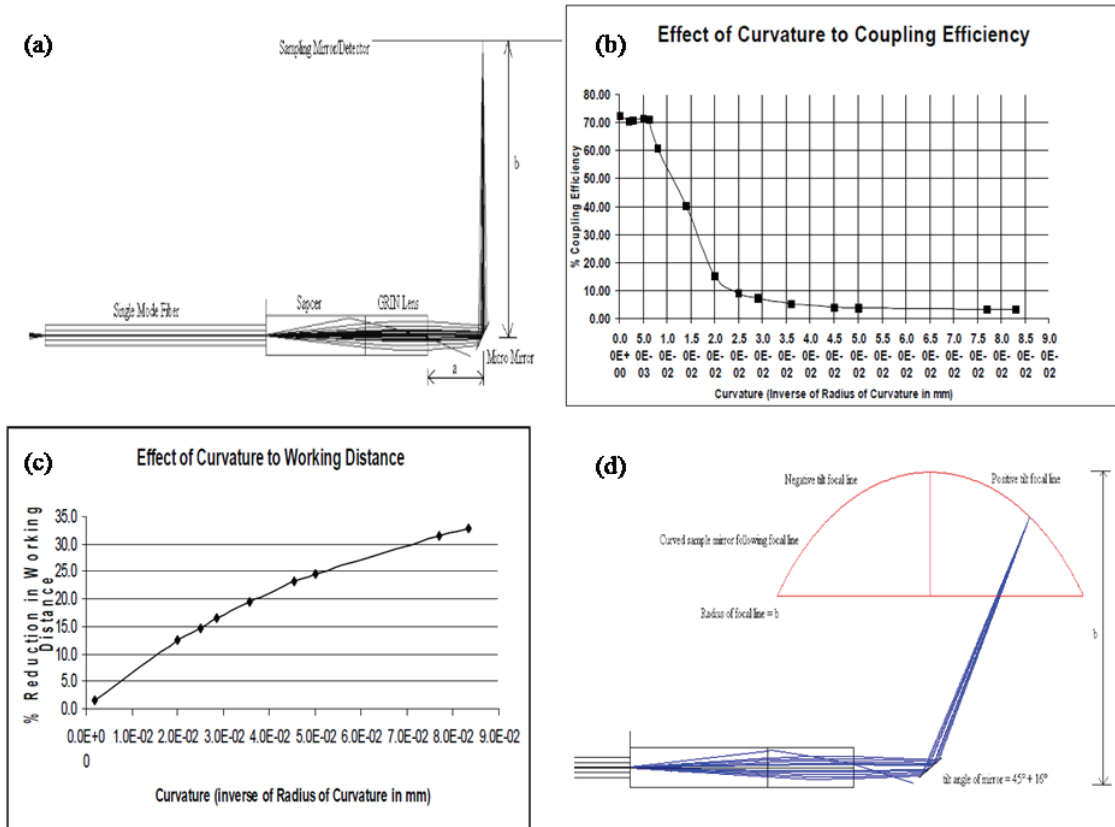


Figure 5.8 (a) Optical simulation of the catheter with GRIN lens and micromirror. (b) Effect of the micromirror's curvature on the coupling efficiency. (c) Effect of the micromirror's curvature on the working distance. (d) Effect of tilting of the micromirror during assembly. (Redraw from Figure 4, 5, 6 and 7 in [106]).

The optical design is the most important part of the catheter design. The imaging quality of the catheter highly depends on proper design of the optical path and the components associated in the optical path. In the optical assembly an important criterion of performance is the optical loss, which is contributed from many sources. The main sources for optical loss are the coupling between the fiber and GRIN lens, the working distance from the GRIN lens to the micromirror, the micromirror roughness, the micro mirror flatness, the housing transparency and the radius of curvature of the housing etc.

An optical simulation was performed using ZEMAX software as shown in Fig. 5.8 (a). In the model all the optical elements were assumed to be perfect so that there were no scattering phenomena. In the diagram the working distance was from the front surface of the GRIN lens to the external mirror as a target. Fresnel reflection from all the surfaces were taken into account in calculation of optical loss obtained from the simulation. The single mode fiber was adjusted to be near to the spacer. The spacer was a glass component with a single refractive index similar to a BK7 glass. This component was considered to be closely attached to the GRIN lens so that air gap and surface transition between them was neglected (although in reality, there was a small gap that may be filled by Canada balsam or air). In the model, on the exposed surface of the GRIN lens and anti-reflection (AR) coating was used to prevent back-reflection. The micromirror deflected the light by 90° to hit the external target mirror. A detector was superimposed with the external target mirror. Maximum coupling efficiency achieved with this design was about 70 %, considering all the losses in the joints. The micromirror was designed to be flat. The mirror surface was coated with Au layer for good reflection. After depositing the Au layer and release of the micromirror, the mirror plate tended to warp; it could be either convex or concave in shape depending on the stress during the process. This caused the mirror plate to have a certain curvature. Most of the mirror plates produced was concave mirror plates. Since the mirror plate shape was of concave nature it resulted in a reduced working distance. To understand the effect of a curved mirror on the assembled optical system, simulation was performed to find out the locations of the changed WD and the coupling efficiency at the original (produced by a flat mirror) WD. Simulation results were plotted in Fig. 5.8 (b). From the result, it was found that the

coupling efficiency decreased with increase of mirror curvature and dropped exponentially when the radius of curvature of mirror fell below certain value, 160mm. From the plot, the curvature of the mirror had to be smaller than $0.66 \times 10^{-2} \text{ mm}^{-1}$ (radius of curvature has to be larger than 152mm) to prevent the coupling efficiency from falling below 60%. Optimization of mirror design and process was in place to improve the curvature of the mirror plate. From the results shown in Fig. 5.8 (c), it was seen that the percentage of reduction in working distance was linearly correlated with the curvature. Estimating directly from the plot, to maintain the change of working distance to be within 5%, the curvature of the mirror had to be smaller than $0.75 \times 10^{-2} \text{ mm}^{-1}$ (radius of curvature has to be larger than 133 mm). The micromirror had an initial position that was laterally tilted 45° relative to the optical axis along the GRIN lens. Defining zero tilt angle as that when the micro mirror was parallel with the GRIN lens objective surface, positive tilt corresponded to directing the rays away from the probe as shown in Fig. 5.8 (d). A simulation was performed to investigate the change in coupling efficiency when the micromirror took on different tilt orientations. A curved external target mirror was used so that maximum coupling could be obtained for all tilt orientations of the micromirror and so that the sample point was always at the focal point. From the results in Fig. 5.8 (d), it was clear that positive tilts resulted in more loss than negative tilts. The loss of optical power increases steadily while the angle of positive tilt is increased. On the negative half of the plot, there was no significant change to coupling efficiency when there was a change in the tilt. Optical Coupling study had done with angle of tilt $+/-160$ from the 45° mirror placement and found that there was a 10% coupling loss in the positive tilt while there was no significant drop in negative tilt. This means, the need for

image compensation in programming was required only when the mirror directs light away from the probe, in the positive tilt.

5.1.5 DRAWBACKS OF TRADITIONAL SIOB

During experiments, several disadvantages of the aforementioned work flow were gradually found and became motivations of the development of the work presented in this paper, which are listed as follows:

- I. In step (1) of section 5.1.3, even if 200 μm were carefully selected to be the most suitable value for the diameter of micro solder balls, placement of these tiny components is still a challenge for us. Any position deviation may lead to fusion of micro sold balls after fluxless heating. Therefore a mechanical isolating structure is preferred to simply the attachment procedure.
- II. In step (2) and (3) of section 5.1.3, the wetting of lead free micro solder balls required high temperature heating which led to damages of the micromirror because that electrothermal bimorph actuators on the micromirror may suffer from overbending leading to plastic deformation or even mechanical failure in such a high temperature. Moreover, two steps heating strategy of step (2) and (3) exaggerated this issue. An alternative is expected to simplify the micro soldering technology and protect the micromirror free of destructive high temperature.
- III. In experiments, we found that in step (3) of section 5.1.3 if the micromirror attached with solder balls was simply inserted into the trench without any extra fixing methods, melted micro solder balls flew onto the Cr/Au lines on the 54.7° side wall of the trench formed by KOH wet etching and the force generated by

melted micro solder balls pulled the micromirror towards the micro sold ball side. Hence the micromirror was no longer vertical to the lower substrate, which naturally led to optical misalignment and low imaging quality. As a solution, an UV curable epoxy was filled in the trench to fix the micromirror before heating. Unfortunately, after heating, we found micro solder balls were difficult to sufficiently contact with the Cr/Au lines on the 54.7° side wall of the trench and loss the electrical connection.

5.2 SiOB WITH INTEGRATED PLATINUM MICROHOTPLATES AND COMB INSULATOR

5.2.1 DESIGN

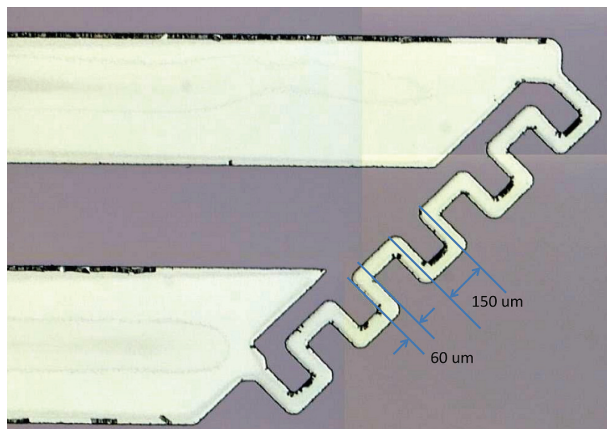


Figure 5.9: Optical image of the Platinum microheater on the lower silicon substrate.

In order to solve these issues, we have developed a new SiOB design consisting of three stacked silicon substrates. The lower substrate still has a 45° trench for the micromirror but DRIE is applied instead of KOH wet etching to form vertical side wall and reduce device dimensions. The other important improvement on the lower substrate lies in that a

serpentine Platinum microheater shown in Fig. 5.9 is fabricated below five Cr/Au pads replacing previous Cr/Au lines on the 54.7° side wall of the trench. The serpentine Platinum microheater aims to provide localized heating of micro solder balls. The main advantage of utilizing microheaters is to locally generate and confine high temperature within a small region, which is more efficient than global heating by using an external hotplate or oven. It has been successfully demonstrated in the localized bonding applications [23], [24]. The pitch and width of the Platinum microheater are $150\ \mu\text{m}$ and $60\ \mu\text{m}$, respectively, which is limited by the $50\ \mu\text{m}$ dry-film photoresist lift process available in IME. In our case, the requirement of an expensive reflow machine has been extinguished by using a power supply and a pair of probes contacting with the pads on the lower silicon substrate for power delivery. In the middle substrate thinned down into $400\ \mu\text{m}$, a comb isolating structure was formed by DRIE etching through the wafer. It is used to be a mechanical isolator to totally separate five micro sold balls. Therefore the complicated pickup and placement procedure is also simplified as “pickup and drop”. There is no obvious functional change in the upper substrate which still carries the GRIN lens assembly. The main optical alignment is still performed on the self-alignment between the lower substrate and the upper substrate. Table 5.2 lists the parameters of both new and previous SiOB designs as well as different micromirrors used as a comparison.

Table 5.2 Parameters of both new and previous SiOB designs as well as different micromirrors used

| Parameters | | New SiOB | Previous SiOB |
|---------------------------|----------------------|--------------|---------------|
| Length (mm) | | 22.5 | 24 |
| Width (mm) | | 2 | 2.5 |
| Thickness (mm) | Lower substrate | 0.4 | 0.4 |
| | Middle substrate | 0.4 | N/A |
| | Upper substrate | 0.725 | 0.725 |
| 45 trench° | Forming method | DRIE | KOH |
| | Depth (um) | 110 | 361 |
| Micromirror | Length (mm) | 2 | 1.5 |
| | Width (mm) | 1.6 | 1.5 |
| | Thickness (mm) | 0.45 | 0.5 |
| | Mirror diameter (mm) | 0.8/1 | 0.5 |
| | Fill factor | 15.71%/24.5% | 8.73% |
| Height with a micromirror | | 2.29 | 1.636 |

5.2.2 FABRICATION PROCESS

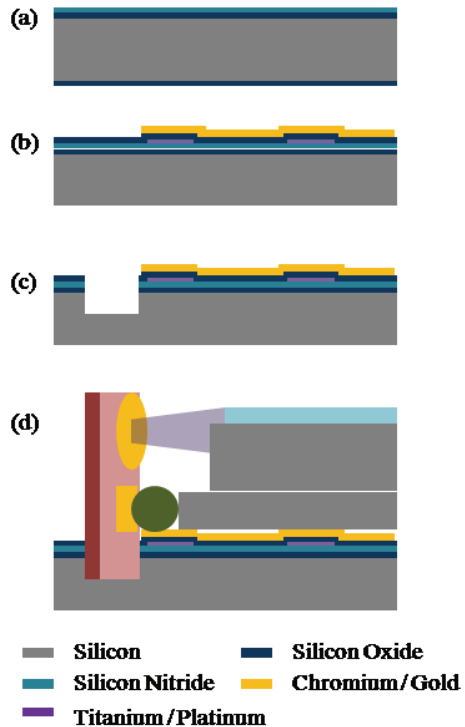


Figure 5.10 Fabrication process: (a) silicon oxide and silicon nitride deposition for stress balancing; (b) Titanium / Platinum lift-off for the microhotplates, silicon oxide deposition for electrical isolation, chromium/gold deposition for electrical wires; (c) DRIE for the trench. (d) Side view of new SiOB assembly.

Only the fabrication flow of a lower substrate of SiOB is shown in Fig. 5.10 (a)-(c). The fabrication started with an 8 inch silicon wafer with 700 μm thickness. The first step was 1000 Å thermal oxide deposition followed by 500 Å PECVD silicon nitride deposition. The mask for Platinum microhotplates was patterned on 20 μm dry film negative photoresist. 200 Å Titanium as adhesive layer and 2000A / 4000 Å Platinum were coated

on the wafer by electronic beam evaporation. Then Platinum microhotplates were created by lifting off of the dry film photoresist. 2000 Å PECVD oxide covered the Platinum microhotplates as an electrical isolation layer for the upcoming Chromium / Gold pads and circuits but opened two rectangular windows at the edge of each lower substrate for the convenience of soldering operation. 150 Å Chromium as adhesive layer as well as 5000 Å gold was then deposited also by e-beam evaporation to form the pads and circuits. A trench with 110 µm was formed by DRIE for the micromirror. Finally the thickness of the processed wafer was thinned down to 400 µm to reduce the overall dimension of SiOB. The half comb structure in the middle substrate and slots in the upper substrate for GRIN lens were also formed by DRIE.

5.2.3 CHARACTERIZATION

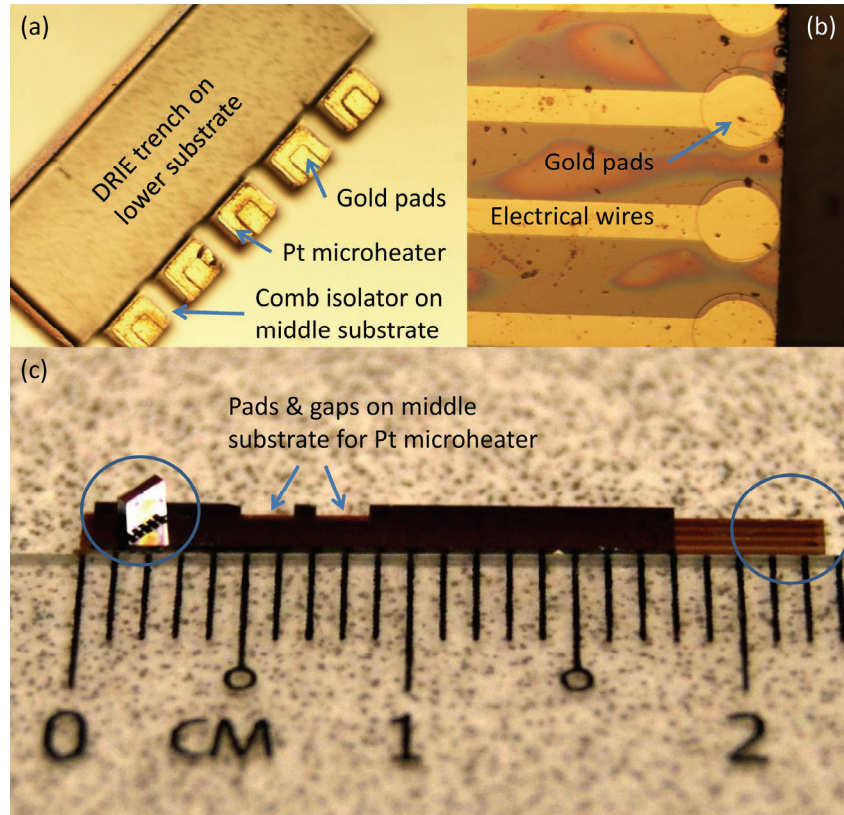


Figure 5.11 Optical images of the SiOB assembly at (a) the distal end, (b) the proximal end and (c) overview with a ruler.

Assembly process flow has become quite simple for the new SiOB design. Optical images of an assembled SiOB with a dummy micromirror are shown in Fig. 5.11 (Note than the upper silicon substrate is not included). At the beginning a common underfill material with high fluidity (U8443, Namics Corporation, Japan) was used to fix the micromirror, the lower silicon substrate and the middle silicon substrate. Secondly five 200 μm plastic core micro solder balls with the melting point of 217.2° (Micropearl SOL-200, Sekisui Chemical Co., Ltd, Japan) are pulled into five trenches made by the comb

structure of the middle substrate. This plastic core micro solder ball features its slight deformation of 3 % after reflow process as well as the relative low melting point. The next step is to use two probes to contact with two pads for the Platinum heater through two gaps opened on the middle silicon substrate and deliver the electrical power provided by an external power supply. Characterizations of the Platinum heater are the main focus in this study and results in detail are provided as follows.

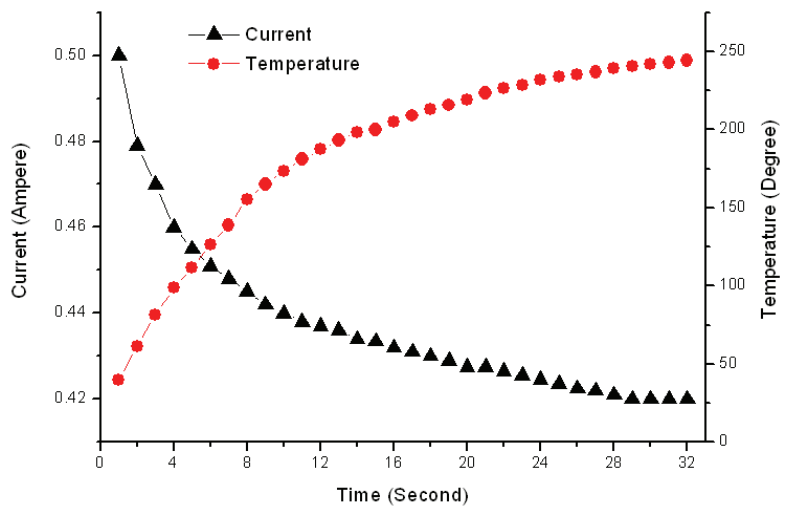


Figure 5.12 (red) step response of the Platinum microheater; (black) Corresponding current change.

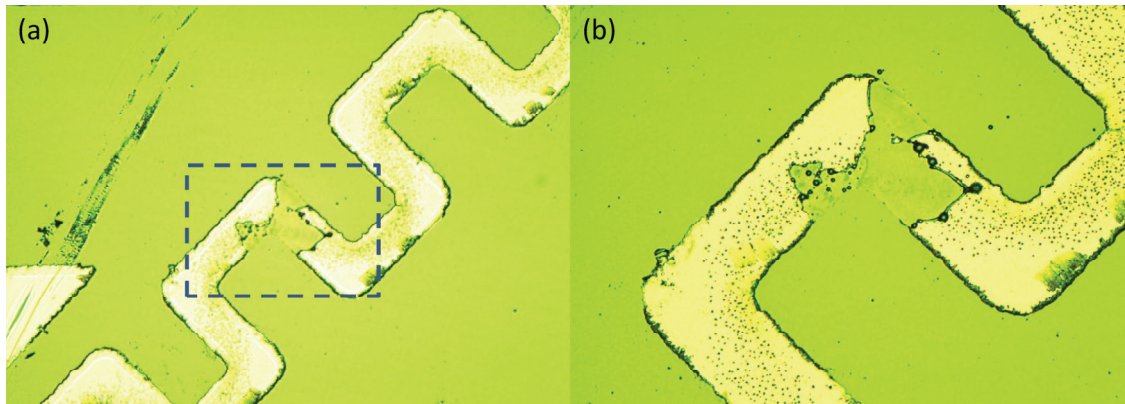


Figure 5.13 Optical microscopic images of a Platinum microheater after heating up to failure.

A Platinum flat film temperature sensor (Pt 100, Labfacility, United Kingdom) is attached to the target Platinum microheater on the lower silicon substrate for a contacting temperature measurement and connected to a multimeter for its resistance measurement. Electrical power is delivered to the Platinum microheater and parameters, such as voltage and current, were read out from the power supply. About 10 V voltage is inputted for the step response measurement. Temperature and current changes are shown in Fig. 5.12. The maximum current appears at the beginning of the measurement when the Platinum microheater is still in the room temperature. The current drops as the temperature increases, as we expected. The maximum temperature achieved is around 250 °C and part of the Platinum heater is observed to peel off. Platinum, as an excellent material for microheaters, can be heated up to 550-600 °C due to its high melting point of 1768 °C, resistance to oxidation as well as tolerance of large current density. However, in our design, the maximum temperature before device failure is slightly less than 250 °C. Because our Platinum microheaters are directly formed on the lower silicon substrate, which led to redundant thermal contact between the Platinum microheater and the rest part of the silicon substrate and result in a reduced peak temperature. The popular design of a microhotplate suspended by beams for thermal isolation is not applied in our design for fabrication process simplification. Furthermore, the melting point of the new Sn/Ag micro solder balls is only 217.3 °C. So our design can meet the requirement of localized heating. The failure mechanism of the Platinum microheater can be attributed to too much thermal stress during heating. Fig. 5.13 shows some optical microscopic images of damaged Platinum microheater.

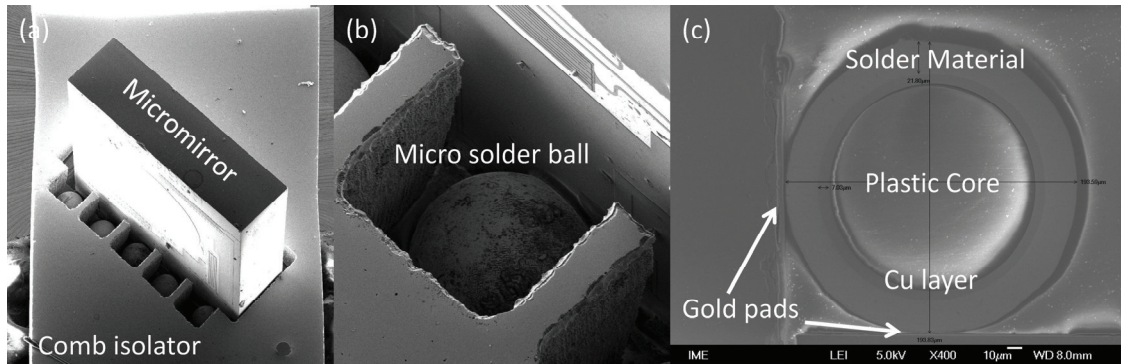


Figure 5.14 (a)-(b): SEM micrographs of a comb isolator and five micro solder balls inside; (c) Cross-sectional SEM micrograph of the connection between the plastic core micro solder ball and pads on the micromirror and the lower silicon substrate.

Fig. 5.14 shows SEM micrographs of assembled SiOB with a dummy micromirror. In Fig. 14 (b) and (c) it is obvious that the 200 μm plastic core solder ball has been wetting with the Cr/Au pads both on the micromirror and the lower silicon substrate. Since there is no significant deformation of the micro solder ball, the wetting area is much smaller and hence the cross-sectional SEM micrograph shown in Fig. 14 (c) may not be precisely located at the wetting area when we were doing mechanical milling and polishing of the expoy molded sample.

5.3 SUMMARY OF SiOB ASSEMBLY

Two kinds of SiOB designs developed for MEMS scanner integrated EOCT catheters have been successfully demonstrated. The overall dimensions of two SiOB designs are 2.5 mm (width) X 25 mm (length) of tradition SiOB and 2 mm (width) X 25 mm (length) of new SiOB which benefit from DRIE vertical etching for forming the trench on the lower substrate. Micro soldering technology was utilized to create electrical connection

for the MEMS scanner. The whole assembly based on the traditional SiOB was inserted into a transparent, biocompatible housing with the diameter of around 4 mm, which was ready for in vivo OCT testing and preliminary OCT imaging results will be shown in the next chapter.

Chapter 6

Endoscopic OCT demonstration

6.1 EXPERIMENTAL SETUP

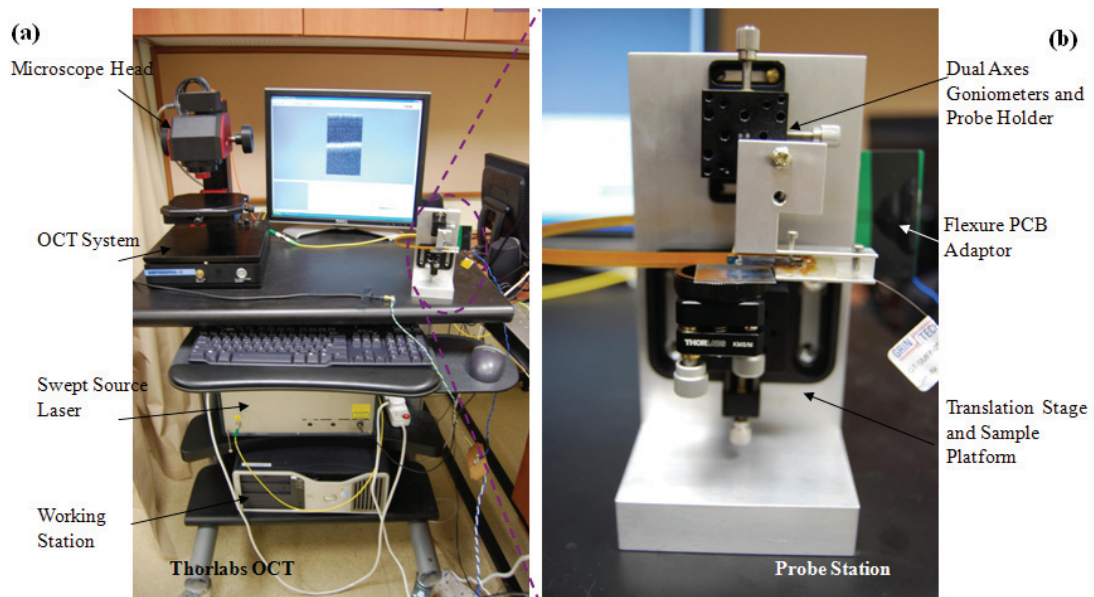


Figure 6.1 (a) The customized swept source OCT system as the experimental setup for optical probe testing. (b) Photo of the probe holder and multi-axis sample platform for testing.

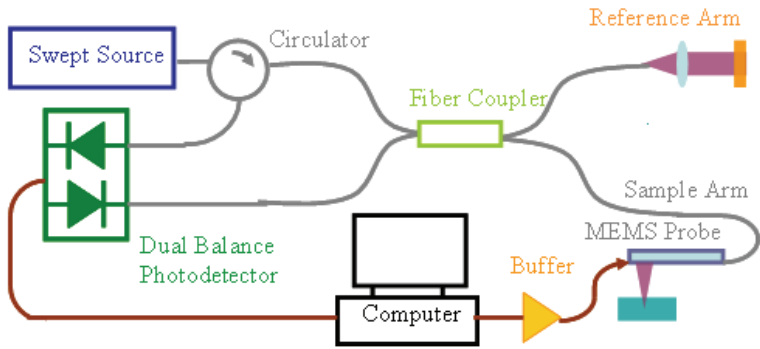


Figure 6.2 Schematic diagram of the swept source OCT system integrated with the two-axis MEMS scanning probe.

The testing of the assembled SiOB MEMS OCT probe was carried out using a commercial swept source OCT system (OCM1300SS, Thorlabs, USA). The photo and schematic diagram of the system are shown in Fig. 6.1 (a) and Fig. 6.2, respectively. The swept source OCT system incorporates a high speed frequency swept external cavity laser (SL1325-P16, Thorlabs, USA), which has a full-width at half maximum (FWHM) bandwidth of 110 nm centered at 1325 nm and 16 kHz fast frequency sweep rate. The output of the light source was split into the sample arm and the reference arm by a broadband 50 / 50 fiber coupler. The A-line acquisition trigger signal generated by the swept light source was fed to a 14 bit, 125 MS/s PCI digitizer (ATS460, AlazarTech, Canada) to initiate data acquisition for OCT interference fringe signals. The sample arm of the swept source OCT system included a microscopy head with an objective lens and a pair of $X-Y$ galvo mirrors (Model 6210H, Cambridge Technology, UK); it was replaced with the assembled SiOB MEMS OCT probe. A photo of the probe holder and multi-axis sample platform for testing is shown in Fig. 6.1 (b). A SMF with a certain length was

inserted into the reference arm to compensate for optical path length mismatch between the two arms. Saw tooth wave forms were generated by a 12 bit high speed analog output board (PCI 6711, National Instruments, USA) to drive two adjacent actuators of the micromirror for fast raster scan across the sample surface. As mentioned above, the micromirror requires up to 20 mA current for full range of deflection of each electrothermal actuator, but the output current of PCI-6711 card was limited to 5 mA per channel. This limitation was overcome by a current buffer circuit, which provided sufficient output current for the electrothermal actuators. The peak-to-peak amplitude and frequency of the sawtooth waveform were controlled by the software of the OCT system.

6.2 OCT IMAGES

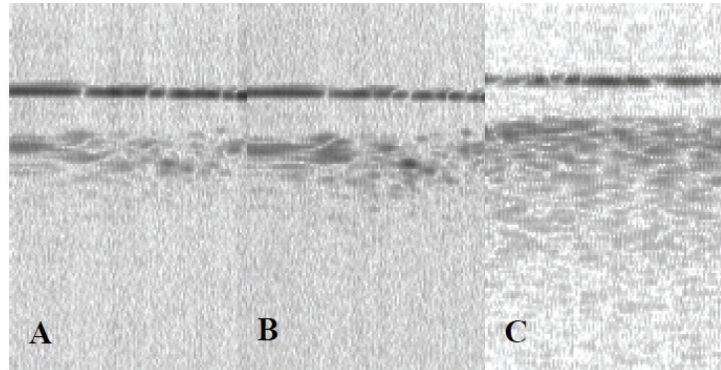


Figure 6.3 (A, B) OCT cross sectional images obtained by the MEMS scanning probe; (C) the reference image obtained by Thorlabs OCM1300SS commercial system. (From Figure 3 in [107]).

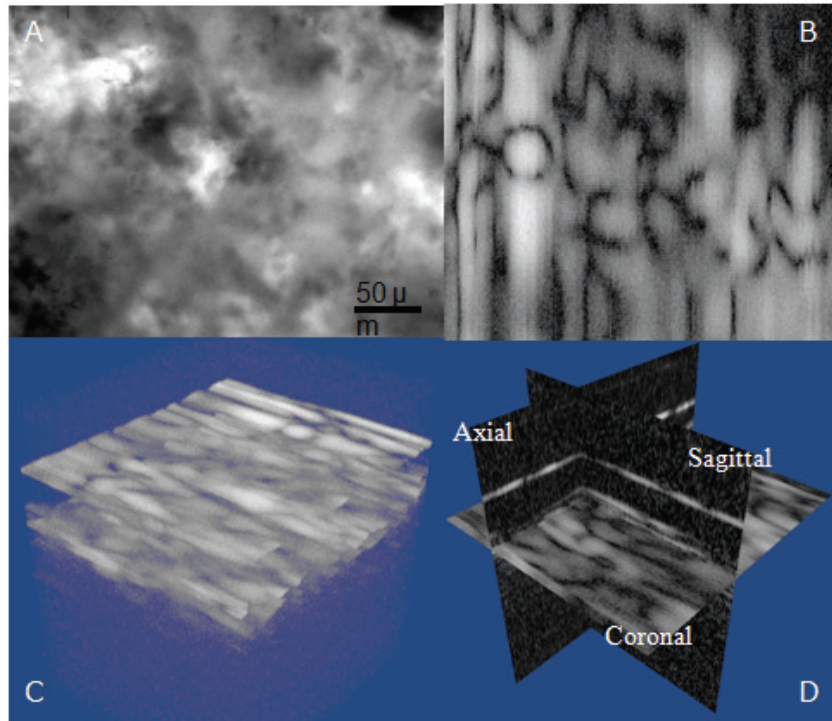


Figure 6.4 (A) *En face* image obtained by a wide field optical microscope. (B) OCT *en face* image. (C) 3D reconstruction of a stack of 2D cross-sectional OCT images for. (D) Orthogonal slices of OCT images of an IR viewing card acquired using the SiOB MEMS OCT probe. (Redraw from Fig. 9 in [34]).

OCT images, both *en face* and three-dimensional, obtained by the SiOB MEMS OCT probe are shown in Fig. 6.3 and Fig. 6.4. An infrared viewing card (VC-VIS/IR, Thorlabs, USA) consisting of a transparent polymer surface and photosensitive material beneath the surface was used as an imaging target. A reference *en face* image of the IR viewing card was obtained by a widefield optical microscope (BX61, Olympus America Inc., USA) with a 0.75 NA objective lens and 550 nm light illumination; the image is shown in Fig. 6.4 (A). A series of two-dimensional cross-sectional images which were stacked together to construct a three-dimensional cross sectional image was obtained by the micromirror in the raster scan. In our study, 450 cross-sectional OCT images (Fig. 6.4 (C)) were

sequentially recorded in a binary file format to combine and reconstruct the three-dimensional volume image shown in Fig. 6.4 (D) as three orthogonal slices in axial, sagittal and coronal directions, respectively. The three-dimensional image has dimensions of $0.55\text{ mm} \times 0.55\text{ mm} \times 1\text{ mm}$. An *en face* OCT image of an arbitrary two dimensional horizontal plane in a relatively small region of the IR viewing card is shown in Fig .6.3 (B). This *en face* image was extracted from the organized 3D dataset. The two images in Fig. 6.3 (A) and (B) may not refer to the same position of the sample. In addition, the current imaging area of our device was limited by the 30 mm radius of curvature of the MEMS micromirror; the imaging area would increase significantly if the radius of curvature was more than 300 mm. The frame rate, which is also the switching rate of the micromirror, is 21.5 fps in our study; this rate meets the requirements of the video rate imaging. The resolution is estimated to be $\sim 20\text{ }\mu\text{m}$ transverse and $\sim 12\text{ }\mu\text{m}$ axial in air.

A low SNR of OCT images was observed and it can be attributed to the loss of light scattered back from the sample under testing. Larger micromirrors with a 1 mm diameter mirror plate will provide 4 times larger field of view than current micromirror of $500\text{ }\mu\text{m}$ diameter and help to capture most of the light scattered back from the sample for improved OCT imaging. Increase in size of the micromirror will reduce the mechanical resonant frequency of the micromirror; however, it will not affect the operational frequency as the mechanical resonant frequency will still be much larger than the thermal switching frequency needed for OCT imaging. The -3 dB cutoff frequency of the micromirror was found to be 46 Hz which is far lower than the estimated resonant frequency ($\sim 2\text{ KHz}$ of a $500\text{ }\mu\text{m}$ micromirror diameter device by simulations in

Coventorware) of the device. Furthermore it would be more convenient for us to align the SiOB plates and improve SNR of OCT signals with larger micromirrors.

Chapter 7

CONCLUSION AND FUTURE RESEARCH

In this thesis, techniques have been demonstrated on two-axis electrothermal MEMS scanners based on a new SOI CMOS compatible fabrication process. MEMS scanners offer fast scanning capability for *in vivo* biological imaging applications. The mechanical and optical properties of MEMS scanners and corresponding SiOB assembly were investigated extensively. The theoretical study on the behaviors of multilayer composite beams under thermal loads, material selection for electrothermal actuators as well as quantitative modeling of two-axis gimbal-less structure are also presented.

In the theoretical study part, an extension of Timoshenko's formula for multilayer composite beams has been developed and utilized to optimize the thickness ratio of different layers in the multilayer composite beam in order to find the maximum mechanical deflection performance of the electrothermal actuator. The thermal response time of the selected electrothermal actuator was also theoretically estimated. Our MEMS scanners are mainly based on two-axis gimble-less structure. The performance of the MEMS scanner depends not only on the active actuator but also on the resting actuators. Therefore a quantitative modeling of two-axis gimbal-less structure has been developed to predict how the geometric variation of the two-axis gimbal-less structure affects the performance of the mirror plate. The modeling strategy employed in this thesis was to simplify the actual two-axis micromirror design as a spatial four-spring and plate system.

Two kinds of electrothermal actuators, curved actuator and FBA, incorporated with two-axis gimbal-less structure have been investigated to enhance the mechanical performance of the MEMS scanner. Previously our old MEMS scanner designs with straight actuators could provide 10 degree mechanical deflection. Now it evolved into curved actuator and FBA for 17 degree and 30 degree mechanical deflection, respectively. In the curved actuator design, the actual length of the actuator was elongated in comparison with the straight actuator design so that larger deflection can be achieved. But, the FBA came in a different way that the FBA performed as an angle provider not a vertical displacement provider as all old actuator designs. Hence FBA is very promising for newly proposed designs and has certain potential to be improved in further.

The two-axis gimbal-less electrothermal micromirror which rotates at 17 degree has been successfully integrated with a tiny double-layer SiOB assembly as well as transparent, biocompatible polycarbonate housing. The traditional SiOB design was developed for a low cost assembly and packaging solution for the MEMS based EOCT catheter and consisted of two silicon substrates vertically stacked for different purposes. A trench was opened by KOH anisotropic wet etching on the top surface of the lower silicon substrate to embrace a two-axis gimbal-less electrothermal micromirror. The function of the other silicon substrate, the upper substrate, was to elevate a customized GRIN lens assembled with a SMF and a glass spacer to the appropriate situation so that the optical axis of the GRIN lens assembly could be precisely aligned with the center of the mirror plate of the micromirror. In order to overcome some drawbacks existing in the traditional SiOB design, a new design integrated with a series of Pt microhotplates has been implemented. By adding five Pt microhotplates below the gold pads, micro soldering to establish

electrical connections between the MEMS scanner on the SiOB and the external drive circuit could be conducted locally and eliminate any potential damage to the MEMS scanner. The preliminary experiments of the well developed EOCT imaging catheter have shown very promising resolution and scanning speed. The work opens a possibility to make compact, high performance and low cost OCT catheters and endoscopes for future clinical applications by using MEMS technology.

Sampling errors leading to missed diagnoses are common with random biopsy, since the diseases may disseminate within a large tissue area and the biopsy operation only sample a small fraction of the tissue under investigation. Typically 3D volumetric data with dimension of 1 mm x 1 mm x 1 mm can be obtained by using aforementioned MEMS based distal scanning OCT endoscopes, which still cannot meet requirements for large area 3D scanning. A hybrid configuration of integrated MEMS micromotor and external translation stage based solution for this purpose has been reported recently [108] but the optical fiber still suffered to stretching forces induced by translational motion and hence lateral scanning speed is limited. Therefore in the future the performance, such as mechanical deflection angle and switch speed, of MEMS scanners may be improved to develop a fully distal scanning large area 3D endoscopic OCT for *in vivo* clinical imaging, which totally eliminates the requirement for external actuated devices for fiber twisting and stretching.

BIBLIOGRAPHY

- [1] D. Huang, E. A. Swanson, W. G. S. C. P. Lin, J. S. Schuman, W. Chang, T. F. M. R. Hee, K. Gregory, C. A. Puliafito, and J. G. Fujimoto, "Optical coherence tomography," *Science* **254**, 1178-1181 (1991).
- [2] E. A. Swanson, D. Huang, M. R. Hee, J. G. Fujimoto, C. P. Lin, and C. A. Puliafito, "High-speed optical coherence domain reflectometry," *Optics Letters* **17**, 151-153 (1992).
- [3] B. Bouma, G. J. Tearney, S. A. Boppart, M. R. Hee, M. E. Brezinski, and J. G. Fujimoto, "High-resolution optical coherence tomographic imaging using a mode-locked Ti:Al₂O₃ laser source," *Optics Letters* **20**, 1486-1488 (1995).
- [4] W. Drexler, U. Morgner, F. X. Kärtner, C. Pitris, S. A. Boppart, X. D. Li, E. P. Ippen, and J. G. Fujimoto, "In vivo ultrahigh-resolution optical coherence tomography," *Optics Letters* **24**, 1221-1223 (1999).
- [5] I. Hartl, X. D. Li, C. Chudoba, R. K. Ghanta, T. H. Ko, J. G. Fujimoto, J. K. Ranka, and R. S. Windeler, "Ultrahigh-resolution optical coherence tomography using continuum generation in an air–silica microstructure optical fiber," *Optics Letters* **26**, 608-610 (2001).
- [6] B. Povazay, K. Bizheva, A. Unterhuber, B. Hermann, H. Sattmann, A. F. Fercher, W. Drexler, A. Apolonski, W. J. Wadsworth, J. C. Knight, P. St. J. Russell, M. Vetterlein, and E. Scherzer, "Submicrometer axial resolution optical coherence tomography," *Optics Letters* **27**, 1800-1802 (2002).

- [7] Y. Wang, Y. Zhao, J. S. Nelson, Z. Chen, and R. S. Windeler, "Ultrahigh-resolution optical coherence tomography by broadband continuum generation from a photonic crystal fiber," *Optics Letters* **28**, 182-184 (2003).
- [8] G. Hausler and M. W. Lindner, "'Coherence radar' and 'spectral radar'—New tools for dermatological diagnosis," *Journal of Biomedical Optics* **3**, 21-31 (1998).
- [9] A. F. Fercher, C. K. Hitzenberger, and G. Kamp, S. Y. El-Zaiat, "Measurement of intraocular distances by backscattering spectral interferometry," *Optics Communications* **117**, 43-48 (1995).
- [10] M. Wojtkowski, R. Leitgeb, A. Kowaleczyk, T. Bajraszewski, and A. F. Fercher, "In vivo human retinal imaging by Fourier domain optical coherence tomography," *Journal of Biomedical Optics* **7**, 457-463 (2002).
- [11] S. R. Chinn, E. A. Swanson, and J. G. Fujimoto, "Optical coherence tomography using a frequency-tunable optical source," *Optics Letters* **22**, 340-342 (1997).
- [12] B. Golubovic, B. E. Bouma, G. J. Tearney, and J. G. Fujimoto, "Optical frequency-domain reflectometry using rapid wavelength tuning of a Cr⁴⁺: forsterite laser," *Optics Letters* **22**, 1704-1706 (1997).
- [13] F. Lexer, C. K. Hitzenberger, A. F. Fercher, and M. Kulhavy, "Wavelength-tuning interferometry of intraocular distances," *Applied Optics* **36**, 6548-6553 (1997).
- [14] M. A. Choma, M. Sarunic, C. Yang, and J. A. Izatt, "Sensitivity advantage of swept source and Fourier domain optical coherence tomography," *Optics Express* **11**, 2183—2189 (2003).

- [15] J. F. de Boer, B. Cense, B. H. Park, M. C. Pierce, G. J. Tearney, and B. E. Bouma, "Improved signal-to-noise ratio in spectral-domain compared with time-domain optical coherence tomography," *Optics Letters* **28**, 2067–2069 (2003).
- [16] R. Leitgeb, C. Hitzenberger, and Adolf Fercher, "Performance of fourier domain vs. time domain optical coherence tomography," *Optics Express* **11**, 889-894 (2003)
- [17] R. Huber, M. Wojtkowski, and J. G. Fujimoto, "Fourier Domain Mode Locking (FDML): A new laser operating regime and applications for optical coherence tomography," *Optics Express* **14**, 3225-3237 (2006).
- [18] R. Huber, D. C. Adler, and J. G. Fujimoto, "Buffered Fourier domain mode locking: unidirectional swept laser sources for optical coherence tomography imaging at 370,000 lines/s," *Optics Letters* **31**, 2975-2977 (2006).
- [19] D. C. Adler, R. Huber, and J. G. Fujimoto, "Phase-sensitive optical coherence tomography at up to 370,000 lines per second using buffered Fourier domain mode-locked lasers," *Optics Letters* **32**, 626-628 (2007).
- [20] R. Huber, D. C. Adler, V. J. Srinivasan, and J. G. Fujimoto, "Fourier domain mode locking at 1050 nm for ultra-high-speed optical coherence tomography of the human retina at 236,000 axial scans per second," *Optics Letters* **32**, 2049-2051 (2007).
- [21] D. C. Adler, Y. Chen, R. Huber, J. S. Schmitt, J. Connolly and J. G. Fujimoto, "Three-dimensional endomicroscopy using optical coherence tomography," *Nature Photonics* **1**, 709-716 (2007).

- [22] G. J. Tearney, M. E. Brezinski, B. E. Bouma, S. A. Boppart, C. Pitriss, J. F. Southern, and J. G. Fujimoto, "In Vivo Endoscopic Optical Biopsy with Optical Coherence Tomography," *Science* **276**, 2037-2039 (1997).
- [23] F. Feldchtein, G. Gelikonov, V. Gelikonov, R. Kuranov, A. Sergeev, N. Gladkova, A. Shakhov, N. Shakhova, L. Snopova, A. Terent'eva, E. Zagainova, Y. Chumakov, and I. Kuznetzova, "Endoscopic applications of optical coherence tomography," *Optics Express* **3**, 257-270 (1998).
- [24] G. J. Tearney, S. A. Boppart, B. E. Bouma, M. E. Brezinski, N. J. Weissman, J. F. Southern, and J. G. Fujimoto, " Scanning single-mode fiber optic catheter-endoscope for optical coherence tomography," *Optics Letters* **21**, 543–545 (1996).
- [25] V. X. D. Yang, Y. X. Mao, N. Munce, B. Standish, W. Kucharczyk, N. E. Marcon, B. C. Wilson, and I. A. Vitkin, "Interstitial Doppler optical coherence tomography," *Optics Letters* **30**, 1791–1793 (2005).
- [26] V. X. D. Yang, M. L. Gordon, S. J. Tang, N. E. Marcon, G. Gardiner, B. Qi, S. Bisland, E. Seng-Yue, S. Lo, J. Pekar, B. C. Wilson, and I.A. Vitkin, "High speed, wide velocity dynamic range Doppler optical coherence tomography (Part III): In vivo endoscopic imaging of blood flow in the rat and human gastrointestinal tracts," *Optics Express* **11**, 2416–2424 (2003).
- [27] Y. Pan, H. Xie, and G. K. Fedder, "Endoscopic Optical Coherence Tomography Based on a CMOS-MEMS micromirror," *Optics Letters* **26**, 1966-1968 (2001).
- [28] H. Xie, Y. Pan and G.K. Fedder, "A SCS micromirror for optical coherence tomographic imaging," *Sensors and Actuators A*, **103**, 237 – 241 (2003).

- [29] T. Xie, H. Xie, G.K. Fedder, and Y. Pan, "Endoscopic Optical Coherence Tomography with a Modified MEMS Mirror for Detection of Bladder Cancers," *Applied Optics* **42**, 6422-6426 (2003).
- [30] J. Singh, T. Gan, A. Agarwal, Mohanraj, and S. Liw, "3D free space thermally actuated micromirror device," *Sensors and Actuators A* **123-124**, 468-475 (2005).
- [31] J. M. Zara, S. Yazdanfar, K. D. Rao, J. A. Izatt, and S. W. Smith, "Electrostatic micromachine scanning mirror for optical coherence tomography," *Optics Letters* **28**, 628-630 (2003).
- [32] W. Jung, J. Zhang, L. Wang, Z. Chen, D. McCormick, and N. Tien, "Three-dimensional endoscopic optical coherence tomography by use of a two-axis microelectromechanical scanning mirror," *Applied Physics Letters* **88**, 163910 (2006).
- [33] A. D. Aguirre, P. R. Herz, Y. Chen, J. G. Fujimoto, W. Piyawattanametha, L. Fan, and M. C. Wu, "Two-axis MEMS scanning catheter for ultrahigh resolution three-dimensional and en face imaging," *Optics Express* **15**, 2445-2453, (2007).
- [34] Y. Xu, J. Singh, C. S. Premachandran, A. Khairyanto, K. W. S. Chen, N. Chen, C. J. R. Sheppard, and M. Olivo, "Design and development of a 3D scanning MEMS OCT probe using a novel SiOB package assembly," *Journal of Micromechanics and Microengineering* **18**, 125005 (2008).
- [35] K. H. Kim, B. H. Park, G. N. Maguluri, T. W. Lee, F. J. Rogomentich, M. G. Bancu, B. E. Bouma, J. F. de Boer, and J. J. Bernstein, "Two-axis magnetically-driven MEMS scanning catheter for endoscopic high-speed optical coherence tomography," *Optics Express* **15**, 18130-18140 (2007).

- [36] J. Singh, T. Gan, A. Agarwal, M. Soundarapandian, and S. Liw, "3D free space thermally actuated micromirror device," *Sensors and Actuators A* **123–124**, 468-475 (2005).
- [37] K. E. Petersen, "Silicon torsional scanning mirror," *IBM Journal of Research Development* **24**, 631-637 (1980).
- [38] N. Singh, K. D. Buddharaju, S. K. Manhas, A. Agarwal, S. C. Rustagi, G. Q. Lo, N. Balasubramanian, and D. L. Kwong, "Si, SiGe nanowire devices by top-down technology and their applications," *IEEE Transactions on Electron Devices* **55**, 3107-3118 (2008).
- [39] S. H. Tao, Q. Fang, J. F. Song, M. B. Yu, G. Q. Lo, and D. L. Kwong, "Cascade wide-angle Y-junction 1 X 16 optical power splitter based on silicon wire waveguides on silicon-on-insulator" *Optics Express* **16**, 21456-21461 (2008).
- [40] L. F. Cheow, L. Yobas, and D. L. Kwong, "Digital microfluidics: droplet-based logic gates" *Applied Physics Letters* **90**, 054107 (2007).
- [41] L. Fan and M. C. Wu, "Two-dimensional optical scanner with large angular rotation realized by self-assembled micro-elevator," *Proceedings of IEEE LEOS Summer Topical Meeting on Optical MEMS*, Paper WB4 (1998).
- [42] V. A. Aksyuk, F. Pardo, C. A. Bolle, S. Arney, C. R. Giles, and D. J. Bishop, "Lucent Microstar micromirror array technology for large optical crossconnects," *Proceedings of the SPIE, MOEMS and Miniaturized Systems*, 320-324 (2000).

- [43] L. Y. Lin and E. L. Goldstein, "Opportunities and challenges for MEMS in lightwave communications," *IEEE Journal of Selected Topics Quantum Electronics* **8**, 163-172 (2002).
- [44] R. R. A. Syms, "Scaling laws for MEMS mirror-rotation optical cross connect switches," *IEEE Journal of Lightwave Technology* **20**, 1084-1094 (2002).
- [45] W. C. Tang, T. C. H. Nguyen, M. W. Judy, and R. T. Howe, "Electrostatic-comb drive of lateral polysilicon resonators," *Sensors and Actuators A*, A21, 5th International Conference on Solid-State Sensors and Actuators and Eurosensors III, 328-331 (1989).
- [46] V. Milanovic, M. Last, and K. S. J. Pister, "Torsional Micromirrors with Lateral Actuators" *Proceedings of Transducers*, 1290-1301 (2001).
- [47] A. Selvakumar, K. Najafi, W. H. Juan, and S. Pang, "Vertical comb array microactuators," *Proceedings of IEEE International Conference on Micro Electro Mechanical Systems, Amsterdam, Netherlands*, 43-48 (1995).
- [48] A. Selvakumar and K. Najafi, "Vertical Comb Array Microactuators," *IEEE Journal of Microelectromechanical Systems* **12**, 440-449 (2003).
- [49] P. R. Patterson, D. Hah, H. Nguyen, R. M. Chao, H. Toshiyoshi, and Ming C. Wu, "A Scanning Micromirror with Angular Comb Drive Actuation," *Proceedings of 15th IEEE International Micro Electro Mechanical Systems Conference*, 544-547 (2002).
- [50] J. Kim, H. Choo, L. Lin, and R. S. Muller, "Microfabricated torsional actuator using self-aligned plastic deformation," *Proceedings of Transducers*, 1015-1018 (2003).
- [51] A. Jain, H. Qu, S. Todd, and H. Xie, "A thermal bimorph micromirror with large bi-directional and vertical actuation," *Sensors and Actuators A* **122**, 9-15 (2005).

- [52] D. Elata and R. Mahameed, “A temperature-gradient driven micromirror with large angles and high frequencies,” *Proceedings of IEEE International conference on MEMS*, 850-853 (2006).
- [53] R. Miller and Y. C. Tai, “Electromagnetic MEMS scanning mirrors,” *Optical Engineering* **36**, 1399-1407 (1997).
- [54] J. W. Judy and R. S. Muller, “Magnetically actuated, addressable microstructures,” *IEEE Journal of Microelectromechanical Systems* **6**, 249-256 (1997).
- [55] S. H. Ahn, and Y. Y. Kim, “Galvanometric silicon scanning mirror with 2 DOF,” *Proceedings of IEEE/LEOS International Conference on Optical MEMS*, Lugano, Switzerland, 87-88 (2002).
- [56] H. J. Nam, Y. S. Kim, S. M. Cho, Y. Yee, and J. U. Bu, “Low voltage PZT actuated tilting micromirror with hinge structure,” *Proceedings of IEEE/LEOS International Conference on Optical MEMS*, Lugano, Switzerland, 89-90 (2002).
- [57] J. Tsuar, L. Zhang, R. Maeda, and S. Matsumoto, “2D micro scanner actuated by sol-gel derived double layered PZT,” *Proceedings of Fifteenth IEEE International Conference on Micro Electro Mechanical Systems*, Las Vegas, NV, 548-551 (2002).
- [58] A. Werber and H. Zappe, “Thermo-pneumatically actuated, membrane-based micro-mirror devices,” *Journal Micromechanics & Microengineering* **16**, 2524-2531(2006).
- [59] A. Werber and H. Zappe, “Tunable pneumatic microoptics,” *IEEE Journal of Microelectromechanical Systems* **17**, 1218-1227 (2008).
- [60] H. Kang and J. Kim, “EWOD (Electrowetting-on-Dielectric) actuated optical micromirror,” *Proceedings of IEEE International Conference on MEMS* 742-745 (2006).

- [61] G. G. Stoney, “The tension of metallic films deposited by electrolysis” *Proceedings of the Royal Society of London. Series A* **82**, 172-175 (1909).
- [62] S. P. Timoshenko, “Analysis of bi-metal thermostat” *Journal of the Optical Society of America* **11**, 233-255 (1925).
- [63] E. Suhir, “Stresses in bi-metal thermostats,” *Journal of Applied Mechanics* **53**, 657-660 (1986).
- [64] E. Suhir, “Interfacial stresses in bimetal thermostat,” *Journal of Applied Mechanics* **56**, 595-600 (1989).
- [65] L. B. Freund, J. A. Floro, and E. Chason, “Extensions of the Stoney formula for substrate curvature to configurations with thin substrates or large deformations,” *Applied Physics Letters* **74**, 1987-1989 (1998).
- [66] T. S. Chow, “Thermal warping of layered composites,” *Journal of Applied physics* **47**, 1351-1354 (1976).
- [67] Z. C. Feng and H. D. Liu, “Generalized formula for curvature radius and layer stresses caused by thermal strain in semiconductor multilayer structures,” *Journal of Applied physics* **54**, 83-85 (1983).
- [68] E. Suhir, “An approximate analysis of stresses in multilayered elastic thin films,” *Journal of Applied Mechanics* **55**, 143-148 (1988).
- [69] T. Y. Pan and Y. H. Pao, “Deformation in multilayer stacked assemblies,” *Journal of Electronic Packaging* **112**, 30-34 (1990).

- [70] Y. H. Pao and E. Eisele, “Interfacial shear and peel stresses in multilayered thin stacks subjected to uniform thermal loading,” *Journal of Electronic Packaging* **113**, 164-172 (1991).
- [71] Y. Y. Hu and W. M. Huang, “Elastic and elastic-plastic analysis of multilayer thin films: closed-form solutions” *Journal of Applied physics* **96**, 4154-4160 (2004).
- [72] C. A. Klein, “How accurate are Stoney’s equation and recent modifications,” *Journal of Applied physics* **88**, 5487-5489 (2000).
- [73] C. A. Klein, “Strains and stresses in multilayered elastic structures: the case of chemically vapor-deposited ZnS/ZnSe laminates,” *Journal of Applied physics* **87**, 2265-2272 (2000).
- [74] C. A. Klein, “Normal and interfacial stresses in thin-film coated optics: the case of diamond-coated zinc sulfide windows,” *Optical Engineering* **40**, 1115-1124 (2001).
- [75] A. Y. Kuo and K. L. Chen, “Effects of thickness on thermal stresses in a thin solder or adhesive layer,” *Journal of Electronic Packaging* **114**, 189-202 (1992).
- [76] A. O. Cifuentes, “A note on the determination of the thermal stresses in multi-metal beams subjected to temperature variations,” *Journal of Electronic Packaging* **113**, 425-427 (1991).
- [77] E. Egan, G. Kelly, and L. Herard, “PBGA warpage and stresses prediction for efficient creation of the thermomechanical design space for package-level reliability,”

Proceedings of IEEE Electronic Components and Technology Conference, 1217-1223 (1999).

- [78] J. K. Gimzewski, Ch. Gerber, E. Meyer, and R. R. Schlittler, "Observation of a chemical reaction using a micromechanical sensor," *Chemical Physics Letter* **217**, 589-594 (1994).
- [79] J. R. Barnes, R. J. Stephenson, C. N. Woodburn, S. J. O'Shea, M. E. Welland, T. Rayment, J. K. Gimzewski, and Ch. Gerber, "A femtojoule calorimeter using micromechanical sensors" *Review of Scientific Instruments* **65**, 3793-3798 (1994).
- [80] J. Lai, T. Perazzo, Z. Shi, and A. Majumdar, "Optimization and performance of high-resolution micro-optomechanical thermal sensors," *Sensors and Actuators A* **58**, 113-119 (1997).
- [81] Y. Zhao, M. Mao, R. Horowitz, A. Majumdar, and J. Kitching, "Optomechanical uncooled infrared imaging system: design, microfabrication, and performance," *IEEE Journal of Microelectromechanical Systems* **11**, 136 – 146 (2002).
- [82] D. Grbovic, N. V. Lavrik, P. G. Datskos, D. Forrai, E. Nelson, J. Devitt, and B. McIntyre, "Uncooled infrared imaging using bimaterial microcantilever arrays," *Applied Physics Letters* **89**, 073118 (2006).
- [83] P. G. Datskos, N. V. Lavrik, and S. Rajic, "Performance of uncooled microcantilever thermal detectors," *Review of Scientific Instruments* **75**, 1134-1148 (2004).

- [84] L. Que, J. S. Park, and Y. B. Gianchandani, “Bent-beam electrothermal actuators-Part I: Single beam and cascaded devices,” *IEEE Journal of Microelectromechanical Systems* **10**, 247 – 254 (2001).
- [85] J. S. Park, L. L. Chu, A. D. Oliver, and Y. B. Gianchandani, “Bent-beam electrothermal actuators-Part II: Linear and rotary microengines,” *IEEE Journal of Microelectromechanical Systems* **10**, 255 – 262 (2001).
- [86] P. J. Gilgunn, J. Liu, N. Sarkar, and G. K. Fedder, “CMOS-MEMS Lateral Electrothermal Actuators,” *IEEE Journal of Microelectromechanical Systems* **17**, 103 – 114 (2008).
- [87] S. Prasanna and S. M. Spearing, “Materials selection and design of microelectrothermal bimaterial actuators,” *IEEE Journal of Microelectromechanical Systems* **16**, 248 – 259 (2007).
- [88] Y. Xu, J. Singh and N. Chen, “Modeling of two-axis gimbal-less scanning micromirror” *Proceedings of the 22th European Conference on Solid-State Transducers (Eurosensors XXII)*, Dresden, Germany, 56-59 (2008).
- [89] J. Singh, J. H. S. Teo, Y. Xu, C. S. Premachandran, N. Chen, R. Kotlanka, M. Olivo, and C. J. R. Sheppard, “A two axes scanning SOI MEMS micromirror for endoscopic bioimaging” *Journal of Micromechanics and Microengineering* **18**, 025001 (2008).
- [90] Y. Xu, J. Singh, T. Selvaratnam, and N. Chen, “Two-axis gimbal-less electrothermal micromirror for large angle circumferential scanning” *IEEE Journal of Selected Topics in Quantum Electronics*, accepted (2009).

- [91] K. W. S. Chen, C. S. Premachandran, A. Khairyanto, J. Singh, and W. Y. Seung, “Package development for MEMS based 3D micro-mirror optical bio-probe for OCT application” *Proceedings of IEEE Electronic Packaging Technology Conference*, 347-351 (2007).
- [92] S. H. Hwang, D. D. Seo, J. Y. An, M. H. Kim, W. C. Choi, S. R. Cho, S. H. Lee, H. H. Park, and H. S. Cho, “Parallel optical transmitter module using angled fibers and a V-Grooved silicon optical bench for VCSEL array,” *IEEE Transactions on Advanced Packaging* **29**, 457-462 (2006).
- [93] Y. Akahori, T. Ohyama, T. Yamada, K. Katoh, and T. Ito, “High-speed photoreceivers using solder bumps and microstrip lines formed on a silicon optical bench,” *IEEE Photonics Technology Letters* **11**, 454-456(1999).
- [94] M. Iwase, T. Nomura, A. Izawa, H. Mori, S. Tamura, T. Shirai, and T. Kamiya, “Single mode fiber MT-RJ SFF transceiver module using optical subassembly with a new shielded silicon optical bench,” *IEEE Transactions on Advanced Packaging* **24**, 419-428 (2001).
- [95] A. K. Chu, Z. Y. Tsai, Y. T. Chen, and J. H. Chiang, “Thin WDM filters for low-cost optical triplexers on silicon optical benches,” *Electronics Letters* **44**, 929-930 (2008).
- [96] K. Yu, D. Lee, and O. Solgaard, “Variable bandwidth optical filters with vertical micromirrors and silicon optical bench alignment technology,” *Proceedings of IEEE Lasers and Electro-Optics Society*, 531-532 (2004).

- [97] J. Li, Q. X. Zhang, and A. Q. Liu, "Advanced fiber optical switches using deep RIE (DRIE) fabrication," *Sensors Actuators A* **102**, 286-295 (2003).
- [98] X. M. Zhang, A. Q. Liu, C. Lu, F. Wang, and Z. S. Liu, "Polysilicon micromachined fiber-optical attenuator for DWDM applications," *Sensors and Actuators A* **108**, 28-35 (2003).
- [99] J. Li, J. K. H. Goh, B. S. P. Lee, Q. X. Zhang, P. V. Ramana, and P. Damaruganath, "Low cost 4-Channel CWDM splitter using SiOB packaging," *Proceedings of IEEE Electronic Components and Technology Conference*, 1745-1751 (2006).
- [100] J. W. Osenbach, M. F. Dautartas, E. Pitman, C. Nijander, M. Brady, R. K. Schlenker, T. Butrie, S. P. Scrank, B. S. Auker, D. Kern, S. Salko, D. Rinaudo, C. Whitcraft, and J. F. Dormer, "Low cost/high volume laser modules using silicon optical bench technology," *Proceedings of IEEE Electronic Components and Technology Conference*, 581-587 (1998).
- [101] A. Q. Liu, X. M. Zhang, H. Cai, D. Y. Tang, and C. Lu, "Miniaturized injection-locked laser using microelectromechanical systems technology," *Applied Physics Letters* **87**, 101101 (2005).
- [102] Y. Yamada, A. Sugita, K. Moriwaki, I. Ogawa, and T. Hashimoto, "An application of a silica-on-terraced-silicon platform to hybrid Mach-Zehnder interferometric circuits consisting of silica-waveguides and LiNbO₃ phase-shifters," *IEEE Photonic Technology Letter* **6**, 822-824 (1994).

- [103] K. Yu, D. Lee D, U. Krishnamoorthy, N. Park, and O. Solgaard, “Micromachined Fourier Transform Spectrometer on silicon optical bench platform,” *Sensors and Actuators A* **130-131**, 523-530 (2005).
- [104] C. S. Premachandran, K. W. S. Chen, J. Singh, J. Teo, Y. Xu, N. Chen, C. Sheppard and M. Olivo, “Design, fabrication and assembly of an optical biosensor probe package for OCT (Optical coherence tomography) application,” *Proceedings of IEEE Electronic Components and Technology Conference*, 1556-1560 (2007).
- [105] C. S. Premachandran, A. Khairyanto, K. W. S. Chen, J. Singh, S. X. L. Wang, Y. Xu, N. Chen, C. J. R. Sheppard, M. Olivo, and J. Lau, “Influence of optical probe packaging on a 3D MEMS scanning micro-mirror for optical coherence tomography (OCT) applications,” *Proceedings of the 58th Electric Components and Technology Conference (ECTC'08)*, 829-833 (2008).
- [106] A. Khairyanto, C. S. Premachandran, K. W. S. Chen, J. Singh, J. Chandrappan, J. H. Lau, and Y. Xu, “Optical alignment of dual-axis MEMS based scanning optical probe for optical coherence tomography (OCT) application,” *Proceedings of the 10th Electronics Packaging Technology Conference (EPTC'08)*, Singapore, 945-950 (2008).
- [107] Y. Xu, J. Singh, C. S. Premachandran, A. Khairyanto, K. W. S. Chen, N. Chen, C. J. R. Sheppard and M. Olivo, “Two axes MEMS probe for endoscopic optical coherence tomography” *Proceedings of the 6th International Conference on Optics Design and Fabrication (ODF'08)*, Taipei, Taiwan, PS-163 (2008).

[108] J. Su, J. Zhang, L. Yu, and Z. Chen, "In vivo three-dimensional microelectromechanical endoscopic swept source optical coherence tomography," *Optics Express* **15**, 10390-10396 (2007).